

## ABSTRACT

SILLETTI, BRYAN ANTHONY. **Characterization of NO<sub>x</sub> Storage Materials by Temperature-Programmed Desorption and Diffuse Reflectance Infrared Spectroscopy.** (Under the direction of H. HENRY LAMB.)

The goal of this research was to elucidate the chemical nature of NO<sub>2</sub> adsorption sites on basic metal oxides (MgO,  $\gamma$ -Al<sub>2</sub>O<sub>3</sub>, MgO/Al<sub>2</sub>O<sub>3</sub>, BaO/Al<sub>2</sub>O<sub>3</sub>, and a hydrotalcite-derived Mg-Al oxide) and in Na- and Ba-exchanged faujasite (NaY and BaY). The mixed oxides were characterized by powder x-ray diffraction (XRD) and surface area analysis using the single-point BET method. Temperature-programmed desorption (TPD) and diffuse reflectance infrared Fourier transform spectroscopy (DRIFTS) were used to characterize the surface species produced by NO<sub>2</sub> and CO<sub>2</sub> adsorption. Our results evidence that NO<sub>2</sub> chemisorbs on basic metal oxides in two forms: (1) NO<sub>2</sub> bound as nitrite species that decompose at moderate temperatures (180-300°C) evolving NO and leaving oxygen on the surface and (2) surface nitrate species that decompose at high temperatures (400-500°C) with concomitant evolution of NO and O<sub>2</sub>. Basicity, as measured by CO<sub>2</sub> TPD, is not the principal characteristic of surface sites for NO<sub>2</sub> adsorption; however, competitive adsorption of CO<sub>2</sub> and NO<sub>2</sub> reveals that there is 20-50% overlap of the two site populations. Site competition between CO<sub>2</sub> and NO<sub>2</sub> is most significant for the more strongly basic sites on BaO/Al<sub>2</sub>O<sub>3</sub>.

Exposure of NaY and BaY to a simulated diesel exhaust gas (containing 20% CO<sub>2</sub>, 12% O<sub>2</sub>, 1000 ppm NO<sub>2</sub> in He) at 30°C demonstrated that these materials have closely similar NO<sub>x</sub> adsorption capacities; however, NO<sub>2</sub> binds much more strongly to BaY than NaY, as evidenced by TPD. For NaY, ~80% of the adsorbed NO<sub>2</sub> desorbed as NO and NO<sub>2</sub> at less than 100°C and the remainder desorbed as NO and O<sub>2</sub> at 200°C. For BaY, ~60% of the adsorbed NO<sub>2</sub> desorbed

as NO and NO<sub>2</sub> at 160°C, while the remainder of the NO<sub>x</sub> desorbed as NO + O<sub>2</sub> at 370°C. Simulated NO<sub>x</sub> storage-reduction experiments revealed that Pt-impregnated BaY could function effectively at diesel exhaust temperatures albeit in the absence of sulfur-containing gases.

Characterization of NO<sub>x</sub> Storage Materials by Temperature-Programmed Desorption and  
Diffuse Reflectance Infrared Spectroscopy

By

BRYAN ANTHONY SILLETTI



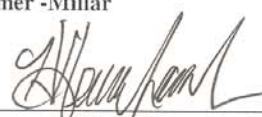
A thesis submitted to the Graduate Faculty of  
North Carolina State University  
in partial fulfillment of the  
requirements for the Degree of  
Master of Science

MATERIALS SCIENCE AND ENGINEERING

Raleigh

2004

APPROVED BY:

 _____ Dr. Angus Kingon	 _____ Dr. JP Maria
 _____ Dr. Lou Balmer -Millar	 _____ Dr. Jerry Spivey
 _____ Dr. H. Henry Lamb	

## **Dedication**

I would like to dedicate this thesis to my family including my father, Harry, my mother, Jeanie, and sisters, Lisa and Sonya. They have always been so incredibly supportive of me and my interests regardless of where it might take me. They constantly afforded me inspiration and unending love and support. It has been only through your constant intercession and encouragement that I have been able to be the person that I am today and hopefully, one day, to be the person that you can admire. To all of my friends and family that I have had the honor to know and grow with, thanks! I look forward to many more fantastic memories.

## **Biography**

Bryan Silletti was born in Toledo, OH on January 17, 1975 to Harry and Regina Silletti with siblings Sonya and Lisa Silletti. His father, Harry Silletti, worked for Owens-Illinois for 30 years and retired at the age of 56 in Toledo, OH after working overseas in Madrid, Spain, London, England, and Milan, Italy. His mother, Regina Silletti, has had a diversified career in conjunction with a Masters in Education and a Masters in Sociology. She has excelled in education both as a college professor and a high school guidance counselor along with several positions at the Private Industry Council (PIC) in Toledo, OH. Within months of his birth, his family transferred to Madrid, Spain as part of his father's company where his entire family began to appreciate the values of the international community and living abroad. Bryan returned to Toledo with his family in 1978 and continued his education in Toledo until he moved to London, England to complete his secondary education at an international school (ACS Hillingdon). Here Bryan's interests in travel and international involvement developed even more and included participation as a delegate to Nigeria in Economic Development at The Hague International Model United Nations (THIMUN) along with extensive travel throughout Europe. After high school, Bryan completed his BS in Chemical Engineering at the University of Notre Dame in South Bend, IN. Upon completion, Bryan learned Italian and completed a two month research project on cation-exchanged zeolites at The Politecnico di Milano in Milan, Italy before starting work at Caterpillar Inc on August 4, 1997. Bryan worked at several business units at Caterpillar for his first 4 years, primarily in the area of elastomeric sealing systems, before transferring to the Advanced Materials Technology (AMT) division. At AMT he was sent to North Carolina State University to pursue his Master's degree in Materials Science and complete a research

program for Caterpillar in the area of NO<sub>x</sub> adsorbers. Bryan has now returned to Caterpillar as a research engineer to continue his research on catalyst development.

## **Acknowledgements**

I would like to acknowledge the constant support and reinforcement from my advisor and professor Dr Henry Lamb. For his knowledge of equipment and understanding of the principles of chemical engineering that has enabled me to grow and progress in my education at NC State. I know that it has taken a great deal of encouragement to focus my efforts to finally complete my Masters. Thanks to Caterpillar Inc. for the funding of this project and particularly, Dr. Lou Balmer-Millar and Dr. Michael Readey, for their support of my continued education in pursuit of a Master's degree at NC State University. Thanks also to Dr. Jerry Spivey, Dr. Angus Kingon, and Dr. JP Maria for all their efforts in support of my thesis and research. Thanks to Susan Sigmon and Ryan Adams for all the support and work in the lab that enabled me to finish.

## TABLE OF CONTENTS

	Page
LIST OF TABLES .....	viii
LIST OF FIGURES .....	ix
INTRODUCTION .....	1
Mixed Oxides in NO <sub>x</sub> Traps .....	10
Investigation of Oxide Surfaces via Probe Molecules .....	13
CHAPTER I: Characterization of (Mg,Al) Oxides as NO <sub>x</sub> Storage Materials using Temperature- Programmed Desorption.....	16
Abstract .....	17
Introduction .....	18
Experimental Methods .....	20
Results .....	22
Discussion.....	26
Conclusions .....	30
Tables .....	31
Figures.....	33
CHAPTER II: Characterization of (Mg,Al) Oxides as NO <sub>x</sub> Storage Materials: Infrared Spectroscopy of Adsorbed Species.....	41
Abstract .....	42
Introduction .....	43
Experimental Methods .....	44
Results .....	45
Discussion.....	50
Conclusions .....	52
Tables .....	53
Figures.....	57
CHAPTER III: Characterization of NO <sub>x</sub> Storage Reduction by Pt/BaY and Pt/Nay Catalysts .....	64
Abstract .....	65
Introduction .....	66
Experimental Methods .....	67
Results and Discussion.....	69
Conclusions .....	72
Tables .....	74
Figures.....	75
CONCLUSIONS AND OUTLOOK .....	80
APPENDICES	



Appendix I: Palladium-Hydrotalcite NO <sub>x</sub> Storage-Reduction Catalysts .....	84
Appendix II: Bulk Magnesium Carbonate and Nitrate Decomposition .....	91
Appendix III: SuperCriticalCO <sub>2</sub> (SCCO <sub>2</sub> ) Solvent Extraction Apparatus Design and Assembly: .....	93
LIST OF REFERENCES .....	95

## LIST OF TABLES

### Chapter I

1.1 BET Surface Area .....	31
1.2 XRD Peak Assignments .....	31
1.3 Sol-Gel and Boehmite Alumina Comparison .....	31
1.4 30°C Comparison of Mixed Oxides .....	32
1.5 100°C Comparison of Mixed Oxides .....	32
1.6 290°C Comparison of Mixed Oxides .....	32

### Chapter II

2.1 Frequencies of Stretching and Bending Vibrations for All Species .....	53
2.2 DRIFTS Characterization of the Adsorption and Desorption of NO <sub>2</sub> Mixed Gas on Al <sub>2</sub> O <sub>3</sub> .....	54
2.3 DRIFTS Characterization of the Adsorption and Desorption of NO <sub>2</sub> Mixed Gas on MgO .....	55
2.4 DRIFTS Characterization of the Adsorption and Desorption of NO <sub>2</sub> Mixed Gas on BaO/Al <sub>2</sub> O <sub>3</sub> .....	56
2.5 DRIFTS Characterization of the Adsorption and Desorption of NO <sub>2</sub> Mixed Gas On Hydrotalcite .....	56

### Chapter III

3.1 Thermal Stability and Storage Capacity Comparison of NO <sub>x</sub> Adsorption on NaY, BaY, Pt/NaY, Pt/BaY.....	74
--	----

## LIST OF FIGURES

### Chapter I

1.1 Diffraction Patterns of HT3, sol-gel $\text{Al}_2\text{O}_3$ , boehmite $\text{Al}_2\text{O}_3$ , $\text{MgO}/\text{Al}_2\text{O}_3$ , $\text{MgO}$ , and $\text{BaO}/\text{Al}_2\text{O}_3$ .....	33
1.2 $\text{CO}_2$ TPD after Adsorption at $30^\circ\text{C}$ .....	34
1.3 $\text{CO}_2$ TPD after Adsorption at $100^\circ\text{C}$ .....	34
1.4 $\text{CO}_2$ TPD after Adsorption at $290^\circ\text{C}$ .....	35
1.5 $30^\circ\text{C}$ Adsorption of $\text{NO}_2$ Mix Gas and $\text{CO}_2$ on Alumina .....	35
1.6 $100^\circ\text{C}$ Adsorption of $\text{NO}_2$ Mix Gas and $\text{CO}_2$ on Alumina .....	36
1.7 $290^\circ\text{C}$ Adsorption of $\text{NO}_2$ Mix Gas and $\text{CO}_2$ on Alumina .....	36
1.8 $\text{MgO}$ , Commercial Hydrotalcite, and $\text{MgO}/\text{Al}_2\text{O}_3$ $\text{CO}_2$ and $\text{NO}_2$ Adsorption at $30^\circ\text{C}$ .....	37
1.9 $\text{MgO}$ , Commercial Hydrotalcite, and $\text{MgO}/\text{Al}_2\text{O}_3$ $\text{CO}_2$ and $\text{NO}_2$ Adsorption at $100^\circ\text{C}$ .....	38
1.10 $\text{MgO}$ , Commercial Hydrotalcite, and $\text{MgO}/\text{Al}_2\text{O}_3$ $\text{CO}_2$ and $\text{NO}_2$ Adsorption at $290^\circ\text{C}$ .....	39
1.11 $\text{MgO}$ , Commercial Hydrotalcite, and $\text{MgO}/\text{Al}_2\text{O}_3$ $\text{CO}_2$ and $\text{NO}_2$ Adsorption at $290^\circ\text{C}$ and cooled in the $\text{NO}_2$ mixed gas .....	40

### Chapter II

2.1 The structure of $\text{CO}_2$ and $\text{NO}_x$ Adsorbates on Oxide Surfaces .....	57
2.2 Absorbance of (A) $\text{Al}_2\text{O}_3$ , (B) $\text{MgO}$ , (C) $\text{BaO}/\text{Al}_2\text{O}_3$ , and (D) HT in He measured at $30^\circ\text{C}$ after Soaking for 1 hour in He at $500^\circ\text{C}$ with KBR as background. ....	58
2.3 Absorbance of (A) $\text{Al}_2\text{O}_3$ , (B) $\text{MgO}$ , (C) $\text{BaO}/\text{Al}_2\text{O}_3$ , and (D) HT in He measured at $30^\circ\text{C}$ after Adsorption and purge after .....	59
2.4 Absorbance of $\text{Al}_2\text{O}_3$ during desorption at $100^\circ\text{C}$ , $200^\circ\text{C}$ , $250^\circ\text{C}$ , $300^\circ\text{C}$ , $350^\circ\text{C}$ , $400^\circ\text{C}$ , and $450^\circ\text{C}$ with $\text{Al}_2\text{O}_3$ after adsorption and purge subtracted from the spectrum .....	60
2.5 Absorbance of $\text{MgO}$ during desorption at $100^\circ\text{C}$ , $200^\circ\text{C}$ , $250^\circ\text{C}$ , $350^\circ\text{C}$ , $400^\circ\text{C}$ , and $450^\circ\text{C}$ with $\text{MgO}$ after adsorption and purge subtracted from the spectrum .....	61

2.6 Absorbance of BaO/Al <sub>2</sub> O <sub>3</sub> during desorption at 100°C, 200°C, 300°C, 400°C, and 500°C with BaO/Al <sub>2</sub> O <sub>3</sub> after adsorption and purge subtracted from the spectrum .....	62
2.7 Absorbance of HT during desorption at 100°C, 200°C, 300°C 400°C, and 500°C with HT after adsorption and purge subtracted from the spectrum .....	63

### Chapter III

3.1 TPD: 100°C Adsorption of CO <sub>2</sub> on (A) NaY and (B) BaY.....	75
3.2 TPD: 4 hour 30°C Adsorption of NO <sub>2</sub> Mixed Gas on (A) NaY and (B) BaY .....	75
3.3 TPD: NO <sub>2</sub> Adsorption at 250°C on (A) BaY (B) Pt/BaY (C) NaY .....	76
3.4 TPD: NO + O <sub>2</sub> Adsorption at 250°C on (A) BaY (B) Pt/BaY .....	76
3.5 TPD: NO adsorption at 250°C (A) NaY and (B) Pt/NaY .....	77
3.6 TPD: NO + O <sub>2</sub> adsorption at 250°C (A) NaY and (B) Pt/NaY .....	77
3.7 TPR(H <sub>2</sub> ): NO <sub>2</sub> adsorption at 250C for 1 hour (A) BaY and (B) Pt/BaY.....	78
3.8 TPR(H <sub>2</sub> ): NO + O <sub>2</sub> adsorption at 250C for 1 hour (A) BaY and (B) Pt/BaY.....	78
3.9 NO <sub>2</sub> /NO equilibrium ratio as a function of temperature and O <sub>2</sub> concentration .....	79

## Introduction

The US Environmental Protection Agency (EPA) has taken several steps to reduce NO<sub>x</sub> emissions. The time period between 2003 and 2007 marks a transition for many US industries to comply with recent NO<sub>x</sub> emission standards. During the 1990s the EPA established nationwide rules tightening NO<sub>x</sub> emissions. NO<sub>x</sub> is a major contributor to acid rain (ranking second only to sulfur compounds); NO<sub>x</sub> compounds foster the creation of photochemical oxidants such as ozone and peroxyacetyl nitrate [1]. Although NO<sub>x</sub> is produced naturally by lightning, bacterial action in the soil, volcanic activity, and human activity, the primary source is the combustion of fossil fuels at temperatures higher than 1500°C [1]. In addition, higher concentrations of these compounds may cause such adverse health effects as decreased lung function or lung cancer, particularly during the presence of smog. Smog is a low-lying perceptible layer of polluted air that is, in essence, a mixture of fog and smoke. There are two types of smog, a winter and summer smog. Summer smog is formed during periods of high Hydrocarbon (HC) and NO<sub>x</sub> concentrations combined with intense sunlight, while winter smog is formed during episodes of quiet and cold weather due to the increased burning of fossil fuels for heating and power supply purposes combined with slow discharge of pollutants in the stagnant atmosphere [2].

On road vehicle emissions account for nearly 50% of ambient NO<sub>x</sub> emissions and thus has been a significant target of EPA legislation [1]. Although legislation on automobile spark ignited (SI) engines tightened quickly through 1982, legislation on compression ignition engines (diesel engines) has lagged behind and is currently aimed at reducing NO<sub>x</sub> emissions by 95% by the year 2010.

Diesel engines operate in a lean (oxygen-rich/fuel-starved) condition and operate more efficiently and cleanly (based on a direct horse power comparison) than the stoichiometric SI

automobile engines. In diesel engines, air is nearly completely compressed in the cylinder before fuel is injected. The amount of fuel that is injected is dependent on the load of the engine. The  $\lambda$  parameter, defined as the ratio of air available to air required for complete combustion, varies between 1.1 and 6 [3]. The SI engine, however, operates at a  $\lambda$  near 1 or commonly referred to as stoichiometric combustion. Under this stoichiometric operation, the Three Way Catalyst (TWC) is able to oxidize the hydrocarbons, CO, and other VOCs, while concurrently reducing NO<sub>x</sub> to meet the required emission standards.

The automotive market, however, is pushing for lean-burn (oxygen rich) combustion to improve fuel economy and the current TWC will be unable to reduce NO<sub>x</sub> emissions in this oxygen rich environment. As a result, a new catalyst system is required to reduce NO<sub>x</sub> emissions. A promising solution to NO<sub>x</sub> removal is the NO<sub>x</sub> storage reduction (NO<sub>x</sub>SR) catalyst or NO<sub>x</sub> trap [4, 5, 6]. This system employs a selective sorbent that oxidizes NO to NO<sub>2</sub> and stores the NO<sub>2</sub> as a nitrate in an oxygen-rich (Lean) combustion gas that includes, NO<sub>x</sub>, O<sub>2</sub>, H<sub>2</sub>O, SO<sub>2</sub>, CO<sub>2</sub>, and N<sub>2</sub>. Then, during fuel-rich exhaust conditions at elevated temperatures, the nitrate quickly decomposes from the catalyst as NO<sub>2</sub> and NO to be reduced to N<sub>2</sub> and O<sub>2</sub> by the reductant (CO, H<sub>2</sub>, other). This new catalyst system can be applied in both diesel and SI engines. Table 1 provides a summary of the various gases and their typical concentrations in a diesel engine.

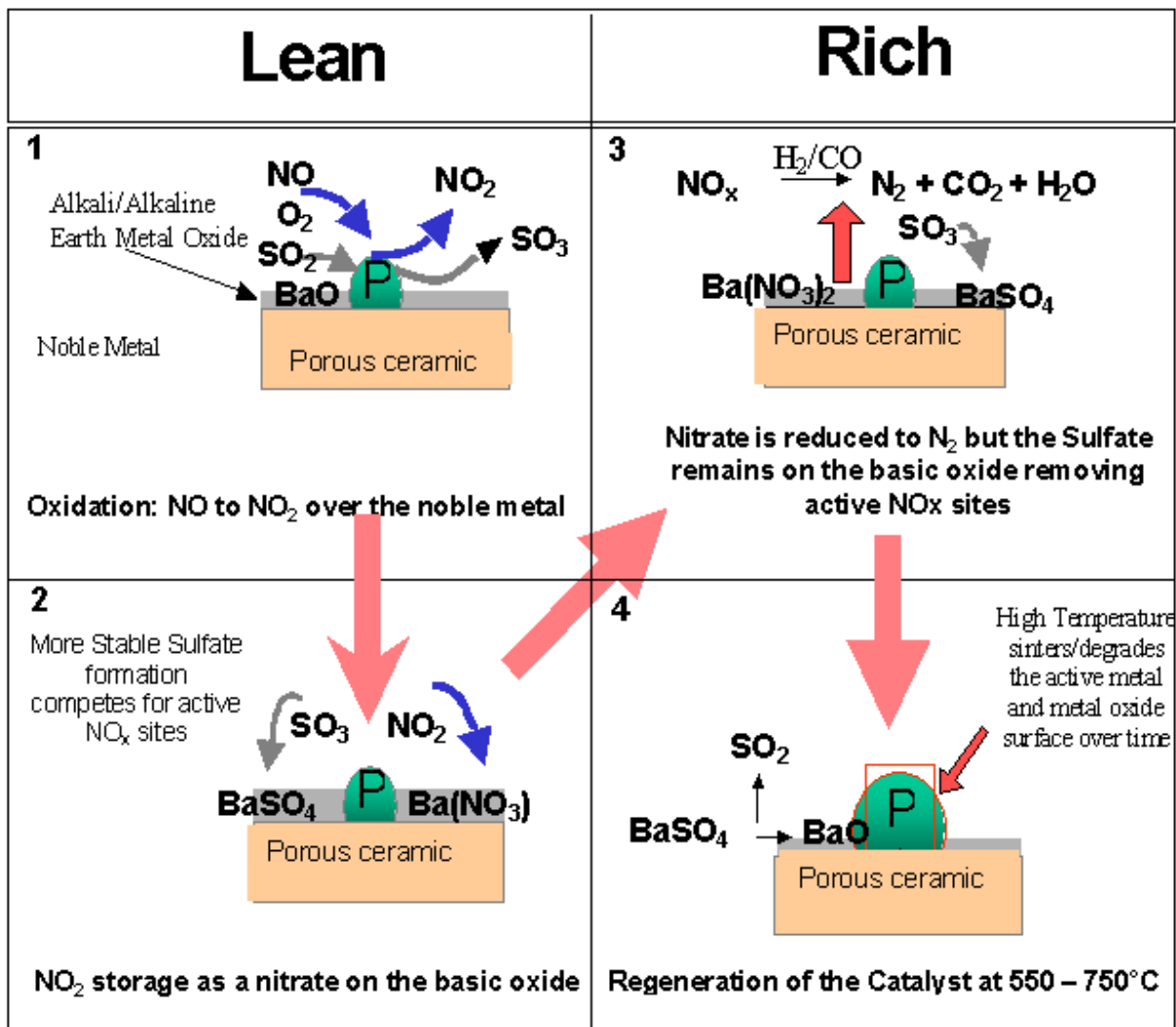
**Table 1: Typical Diesel Gas Concentrations:**

	NO <sub>x</sub>	O <sub>2</sub>	H <sub>2</sub> O	SO <sub>2</sub>	CO <sub>2</sub>	CO	HC	N <sub>2</sub>
Concentration	500 ppm	12%	8%	30 ppm	8%	200 ppm	200 ppm	Balance

An example of a typical NO<sub>x</sub> trap is Pt/Rh/BaO/Al<sub>2</sub>O<sub>3</sub> [7]. In this catalyst, platinum is loaded on the catalyst at 1% by weight for oxidation of NO; BaO is doped onto the oxide support

and acts as the adsorbent for  $\text{NO}_2$  during lean conditions;  $\text{Al}_2\text{O}_3$  is the oxide support and Rh is used to catalyze the reduction of  $\text{NO}_x$  to  $\text{N}_2$  and  $\text{O}_2$ . Figure 1 below depicts these mechanisms of the  $\text{NO}_x$  trap catalyst. In addition to the  $\text{NO}$  oxidation, storage and reduction mechanisms, this figure also illustrates the thermal and sulfur deactivation mechanisms.

**Figure 1:  $\text{NO}_x$  Trap Mechanism [8]**



Kobayashi et al reviewed several of the particular reactions that occur on a  $\text{NO}_x$  trap both in lean and rich conditions and they are given below as equations 1a – 5e. [9]. Kobayashi indicated that the  $\text{NO}_x$  trap mechanism is driven by equilibrium processes based on gas

concentrations of the exhaust gas components. For example, increasing the partial pressure of oxygen will increase NO<sub>2</sub> formation, while higher CO<sub>2</sub> levels will drive the carbonate formation and destabilize the nitrate. In addition, based on their results, as H<sub>2</sub>O increased, the NO conversion increased, which suggested a process path via the metal hydroxide. The NO<sub>x</sub> trap performance is most dependent on the precious metal loading and the alkali metal oxide distribution. Based on Kobayashi's ranking, the NO<sub>x</sub> trap performance for the alkali metals and alkaline earth metals varied as follows: K > Ba > Sr > Na > Ca > Li > Mg, while the NO conversion decreased as follows: Pt/Rh > Pd/Rh > Pd only.

#### **Lean Exhaust Conditions (Temperature Operating Window) [9]**

- 1). NO oxidation to NO<sub>2</sub> by precious metals (Low Temp Operation)



- 2). Formation of the Nitrate

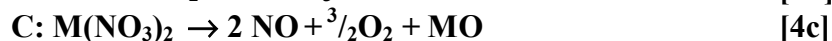
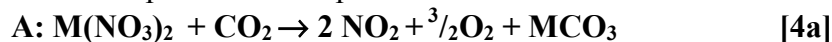


- 3). NO<sub>x</sub> Trap Storage

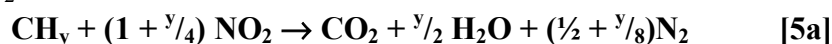


#### **Rich Exhaust Conditions (High Temp.)**

- 1). Nitrate Decomposition or Displacement



- 2). NO<sub>2</sub>/NO Reduction



Kobayashi also investigated the thermodynamics of each stage of the NO<sub>x</sub>SR catalyst during both the lean and rich conditions. During the lean exhaust condition, the NO is oxidized



to NO<sub>2</sub> (given in step [1a]) and the NO<sub>2</sub> subsequently interacts with oxygen and the surface of the metal oxide to form a metal nitrate. During storage, Kobayashi investigated various pathways that lead to the metal nitrate. Table 2 is a review of the various alkali and alkaline earth metal oxides and their equilibrium constants for the NO<sub>x</sub> storage equations [3a] – [3d], in the lean condition at 300, 350°C and atmospheric pressure. The largest positive equilibrium constants are the most thermodynamically favorable processes. From table 2 [9], it can be seen that, as a general trend, reaction B and D are more thermodynamically favored and that reaction B with Barium is the most thermodynamically favored of all the reactions. During the rich exhaust condition, the nitrate can be displaced by the carbonate, oxide, or hydroxide phases and the desorbed NO<sub>x</sub> species can be reduced via the pathways written for each reductant.

**Table 2: NO<sub>x</sub> Trap Storage Reaction Equilibrium Constants (LogKp)**  
(Lean Conditions)

	Reaction A			Reaction B			Reaction C			Reaction D	
<b>Metal</b>	300°C	350°C		300°C	350°C		300°C	350°C		300°C	350°C
<b>Li</b>	-1.10	-1.54		8.72	7.38		-7.16	-6.80		2.66	2.13
<b>Na</b>	6.16	5.12		17.0	14.0		-4.58	-4.46		5.24	4.47
<b>K</b>	11.4	9.92		21.3	18.8		-2.61	-2.69		7.21	6.24
<b>Mg</b>	-19.4			0.279			-19.4			0.217	
<b>Ca</b>	-8.08	-8.91		11.6	8.93		-16.0	-15.6		3.63	2.29
<b>Sr</b>	-1.11	-2.57		15.3	12.5		-13.8	-13.5		5.86	4.34
<b>Ba</b>	4.14	2.29		23.8	20.1		-11.9	-11.8		7.72	6.06

Table 3 provides a review of the equilibrium constants in the rich gas conditions for the nitrate displacement. The three comparison reactions are given below, 1 - 3. This review indicates that, in the presence of CO<sub>2</sub>, the carbonate is the most thermodynamically favored species in the reduction environment and is the most thermodynamically stable for potassium and sodium

1. Carbonate Formation: M-oxide + CO<sub>2</sub> -> M-Carbonate;
2. Hydroxide Formation: M-Oxide + H<sub>2</sub>O -> M-Hydroxide
3. Hydroxide to Carbonate: M-Hydroxide + CO<sub>2</sub> -> M-Carbonate

**Table 3: Nitrate Displacement Equilibrium Constants (LogKp)**  
(Rich Condition)

	Carbonate Formation		Hydroxide Formation		Hydroxide To Carbonate	
<b>Metal</b>	300°C	350°C	300°C	350°C		350°C
<b>Li</b>	12.1	10.5	2.33	1.88	7.46	6.75
<b>Na</b>	21.5	19.2	5.74	4.88	10.5	9.41
<b>K</b>	28.1	25.2	8.10	7.27	11.9	10.7
<b>Mg</b>	0.06	-0.656				
<b>Ca</b>	7.93	6.64	2.52	1.76	5.41	4.89
<b>Sr</b>	12.7	10.9	3.76	2.74	8.90	8.20
<b>Ba</b>	16.1	14.1	6.35	5.29	9.71	8.79

Table 4 documents Pauling's electronegativity for all the periodic table of elements. The most basic metal oxides are associated with the most electropositive metals, particularly the

Alkali and Alkaline-earth metals. Although several of the alkali metals are more electropositive than Ba, including Na, K, and Cs, the most stable nitrate under lean conditions (from Table 2) is the Barium species, as it is the largest, most polarizable alkaline earth metal with a very low electronegativity of 0.9.

**Table 4: Periodic Table of Pauling's Electronegativity [10]**

Group Period	1	2	3	4	5	6	7	8	9	10	11	12	13	14	15	16	17	18
1	<a href="#">H</a> 2.1																	<a href="#">He</a>
2	<a href="#">Li</a> 1	<a href="#">Be</a> 1.5											<a href="#">B</a> 2	<a href="#">C</a> 2.5	<a href="#">N</a> 3	<a href="#">O</a> 3.5	<a href="#">F</a> 4	<a href="#">Ne</a>
3	<a href="#">Na</a> 0.9	<a href="#">Mg</a> 1.2											<a href="#">Al</a> 1.5	<a href="#">Si</a> 1.8	<a href="#">P</a> 2.1	<a href="#">S</a> 2.5	<a href="#">Cl</a> 3	<a href="#">Ar</a>
4	<a href="#">K</a> 0.8	<a href="#">Ca</a> 1	<a href="#">Sc</a> 1.3	<a href="#">Ti</a> 1.5	<a href="#">V</a> 1.6	<a href="#">Cr</a> 1.6	<a href="#">Mn</a> 1.5	<a href="#">Fe</a> 1.8	<a href="#">Co</a> 1.9	<a href="#">Ni</a> 1.8	<a href="#">Cu</a> 1.9	<a href="#">Zn</a> 1.6	<a href="#">Ga</a> 1.6	<a href="#">Ge</a> 1.8	<a href="#">As</a> 2	<a href="#">Se</a> 2.4	<a href="#">Br</a> 2.8	<a href="#">Kr</a>
5	<a href="#">Rb</a> 0.8	<a href="#">Sr</a> 1	<a href="#">Y</a> 1.2	<a href="#">Zr</a> 1.4	<a href="#">Nb</a> 1.6	<a href="#">Mo</a> 1.8	<a href="#">Tc</a> 1.9	<a href="#">Ru</a> 2.2	<a href="#">Rh</a> 2.2	<a href="#">Pd</a> 2.2	<a href="#">Ag</a> 1.9	<a href="#">Cd</a> 1.7	<a href="#">In</a> 1.7	<a href="#">Sn</a> 1.8	<a href="#">Sb</a> 1.9	<a href="#">Te</a> 2.1	<a href="#">I</a> 2.5	<a href="#">Xe</a>
6	<a href="#">Cs</a> 0.7	<a href="#">Ba</a> 0.9		<a href="#">Hf</a> 1.3	<a href="#">Ta</a> 1.5	<a href="#">W</a> 1.7	<a href="#">Re</a> 1.9	<a href="#">Os</a> 2.2	<a href="#">Ir</a> 2.2	<a href="#">Pt</a> 2.2	<a href="#">Au</a> 2.4	<a href="#">Hg</a> 1.9	<a href="#">Tl</a> 1.8	<a href="#">Pb</a> 1.9	<a href="#">Bi</a> 1.9	<a href="#">Po</a> 2	<a href="#">At</a> 2.2	<a href="#">Rn</a>
7	<a href="#">Fr</a> 0.7	<a href="#">Ra</a> 0.9																

The NO<sub>x</sub> trap can operate at nearly 90% conversion, but it has several significant deactivation mechanisms that currently limit its use in the automotive and diesel engine applications. General deactivation mechanisms for catalysts are characterized by the following: poisoning, blockage of pores, sintering of metals, reorganization of the catalyst surface, loss of active material through volatilization and support attrition, and degradation through chemical, mechanical and thermal strains [11]. Although there are many potential deactivation mechanisms for the NO<sub>x</sub> trap catalyst, there are two primary deactivation mechanisms. The predominant deactivating mechanism for NO<sub>x</sub> traps is the preferential adsorption of SO<sub>2</sub> as both a bulk and surface sulfate [12]. SO<sub>2</sub> follows a similar storage mechanism as NO; it is oxidized to SO<sub>3</sub> and

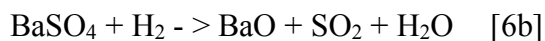
subsequently stored as the sulfate on the catalyst. Unfortunately, the sulfate is more thermodynamically stable than the nitrate and thus the  $\text{SO}_3$  reacts preferentially with the basic oxide, thus removing available active sites for  $\text{NO}_2$  adsorption. Matsumoto et al indicated similar trends on the specific support, Pt/Rh/BaO/ $\text{Al}_2\text{O}_3$ . They indicated that the mechanism of  $\text{SO}_2$  poisoning of the catalyst occurs through oxidation of the sulfur dioxide by the precious metals and subsequent reaction with the support and alkali metals to form both aluminum sulfates and barium sulfate as demonstrated by the differential thermal analysis (DTA) and IR [13]. Based on this study, it was unclear whether aluminum sulfate covered the surface of the  $\gamma$ -alumina or plugged the micropores. Regardless of the location of the sulfate, this mechanistic study indicates that the support is also deactivated by sulfate which causes further surface degradation through reduction in surface area or pore volume. The degree of inhibition that occurred was dependent on the  $\text{SO}_2$  concentration in the feed gas and on the exposure time.

Using X-ray Photoelectron Spectroscopy (XPS), Engstrom et al. documented that sulfates were formed after the  $\text{NO}_x\text{SR}$  was exposed to  $\text{SO}_x$  and they further indicated that all of the  $\text{SO}_2$  in the feed gas accumulates in the catalyst independent of  $\text{SO}_2$  concentration. Thus even low  $\text{SO}_2$  concentrations will cause deactivation [14]. In addition to the deactivation of the storage capacity, Engstrom et al indicated that the oxidation of  $\text{NO}$  to  $\text{NO}_2$  decreases as a result of  $\text{SO}_3$  exposure. This will result in a reduced storage efficiency of  $\text{NO}$ . They further illustrated that the steady state production of  $\text{NO}_2$  by the catalyst gradually decreases with  $\text{SO}_2$  exposure time by blocking the noble metal sites by  $\text{SO}_2$  derived species [15]. Wilson et al showed that  $\text{SO}_2$  overlayers on Pt are highly reactive towards  $\text{C}_3\text{H}_6$  oxidation resulting in sulfur deposits after reduction on the noble metal [16]. These overlayers may also be susceptible to  $\text{CO}$  and  $\text{H}_2$ , although it was not indicated in this article. The presence of  $\text{SO}_2$  also inhibits the reduction activity of the catalyst. The incomplete  $\text{NO}_x$  reduction during the rich phase after  $\text{SO}_2$  exposure,

together with the increased N<sub>2</sub>O formation during the rich period, are strong indications of inhibition or poisoning of the reduction sites (e.g Rh). The cause of the blocking effect on the reduction sites is estimated to be the same as that of oxidation.

Based on the properties of the gas and bulk species, the thermodynamic stability of the various species of Barium was summarized by Ambertsson et al. In only O<sub>2</sub> with bulk BaO, BaO<sub>2</sub> is the most stable phase through 400°C, after which it begins to decompose into BaO [17]. When NO, NO<sub>2</sub>, and O<sub>2</sub> are added to the gas mixture, Ba(NO<sub>3</sub>)<sub>2</sub> is the most stable compound up to 500°C, but then rapidly decreases through 600°C [17]. In the presence of CO<sub>2</sub>, BaCO<sub>3</sub> becomes thermodynamically stable from 300°C up to approximately 1100°C [17]. The thermodynamic stability of the Barium species is significantly affected by the presence of O<sub>2</sub>, H<sub>2</sub>O, and CO<sub>2</sub> along with NO and NO<sub>2</sub>. Depending on the gas species present, the stability of the Ba(NO<sub>3</sub>)<sub>2</sub> stability will vary between 350°C and 600°C [17]. As a result, a realistic gas mixture is required to develop an accurate assessment of the NO<sub>x</sub> adsorber performance during the storage and regeneration phase.

The sulfate stability, not discussed by Ambertsson et al, will be the most stable phase through 1000°C in the absence of any reductant. Breen et al from the University of Limerick documented that CO<sub>2</sub> aids in the removal of sulfates under hydrogen rich conditions to form the metal carbonate that is more stable than the oxide [17]. They evaluated the ΔG of the following reactions ([6a] – [6b]) at various temperatures:



The ΔG of the carbonate formation from the sulfate becomes thermodynamically stable at 600°C with CO<sub>2</sub> + H<sub>2</sub> over a Pt-Rh/CeO<sub>2</sub> – Al<sub>2</sub>O<sub>3</sub> catalyst and allows the removal of the sulfate, while with only H<sub>2</sub> the ΔG does not thermodynamically favor BaO until nearly 1000°C.

Other NO<sub>x</sub> trap deactivation mechanisms include:

1. Thermal deterioration upon reaction of the NO<sub>x</sub> storage materials with compounds within the washcoat and particle growth of both the precious metals and the NO<sub>x</sub> storage materials [11]
2. Mechanical degradation of the support due to the molar volume change associated with the adsorption of the gas and changing from the oxide, carbonate, and hydroxide to the nitrate and sulfate.

Now that there is a clearer picture of the nature of NO<sub>x</sub> Storage reduction, it is important to investigate the trends of the industry to improve the sulfur tolerance of a NO<sub>x</sub> trap. One of the areas that have been a major target of industry is the area of mixed oxides to utilize an optimal support to balance the storage and reduction mechanism. A second area is to investigate materials that can replace Ba as the storage component using various transition metals, alkali and alkaline earth metals.

### **Mixed Oxides in NO<sub>x</sub> Traps**

Most heterogeneous catalysts consist of a catalytically active component such as: metal, an organometallic or a metal oxide that is dispersed on a porous support. In many cases, the surface of the support may participate as the active component. High surface area supports tend to have a microporous structure, in which the primary function is to provide a location for the dispersion of the active species [18]. By investigating the nature of the metal oxide-support interaction dramatic enhancement in catalytic activity and selectivity relative to unsupported oxides can be achieved. The solid support usually contains a pore network with pores ranging

from micro (<20 Angstroms) through to macro pores, approaching micron dimensions [18]. The location of the catalytically active component within the porous structure is critical. The manner in which pores interconnect and aid in the gas diffusion process have a profound effect on the accessibility of reactants to the catalytically active site, and to the removal of products [18].

The interaction of oxide supports, namely  $\text{TiO}_2$ ,  $\text{Al}_2\text{O}_3$ ,  $\text{SiO}_2$ ,  $\text{ZrO}_2$ ,  $\text{CeO}_2$  and others can yield a combination of promotion and stabilization that utilizes surface interaction to achieve optimal basicity, acidity, structural stability and reaction sites. Promoters accelerate the effect of the catalytic reactions, but are not catalytic alone. Stabilizers ensure the thermal, structural, surface, and electronic integrity over larger variations in pressure, temperature and gas composition. In many catalytic systems, the performance is known to depend not only on the inherent catalytic activity of the active phase, but also on the textural and physicochemical properties of the support. In an attempt to obtain better catalysts, the use of some new Ti-Al supports have been tried with promising results in reaction systems like hydrodesulfurization [19,20,21]. In this case, greater catalytic activities have been found due to the role of the support.

It is known that  $\text{TiO}_2$  is more resistant to sulfation among transition metal oxides. The sulfate formed on  $\text{TiO}_2$  is unstable, primarily due to its acidity, and the active sites can be restored under reaction conditions. However, the formation of sulfates on  $\gamma\text{-Al}_2\text{O}_3$  active sites is more stable and less likely to be regenerated.  $\text{TiO}_2$  has been commercially used as a support for vanadia catalyst in ammonia SCR reaction to remove  $\text{NO}_x$  from power plants due to its resistance to  $\text{SO}_2$  [22]. Several studies have shown that combining alumina with titania reduces the stability of the sulfate. This mixed oxide provides a potential avenue for improve sulfur tolerance for  $\text{NO}_x$  adsorber applications. They demonstrated that  $\text{NO}_x$  storage decreases with

decreasing  $\text{SO}_2$  storage, most likely due to the acidity of the metal oxide support or the electronegativity of the metal ion [23]. However, the potential that occurs is in finding the optimum surface chemistry such that  $\text{NO}_x$  can be stably adsorbed and desorbed from the surface with sufficient capacity and without degradation by  $\text{SO}_2$ . It is in this surface chemistry that the titania destabilizes the sulfate formation on the alumina in the mixed metal oxides, while still providing the required framework for adequate  $\text{NO}_x$  storage. Concurrently, the alumina also restricts the grain growth of  $\text{TiO}_2$  occurring during the anatase–rutile transition associated with a significant reduction in surface area.

Matsumoto et al evaluated the current Japanese  $\text{NO}_x$  trap that is used on only Japanese cars due to the low sulfur fuel [4]. His study documents the changes that occur in the  $\text{NO}_x$  trap for improved performance in the presence of  $\text{SO}_2$ .

**Figure 2: Comparison of  $\text{NO}_x$  Storage after Regeneration to Desulfation Temperature**

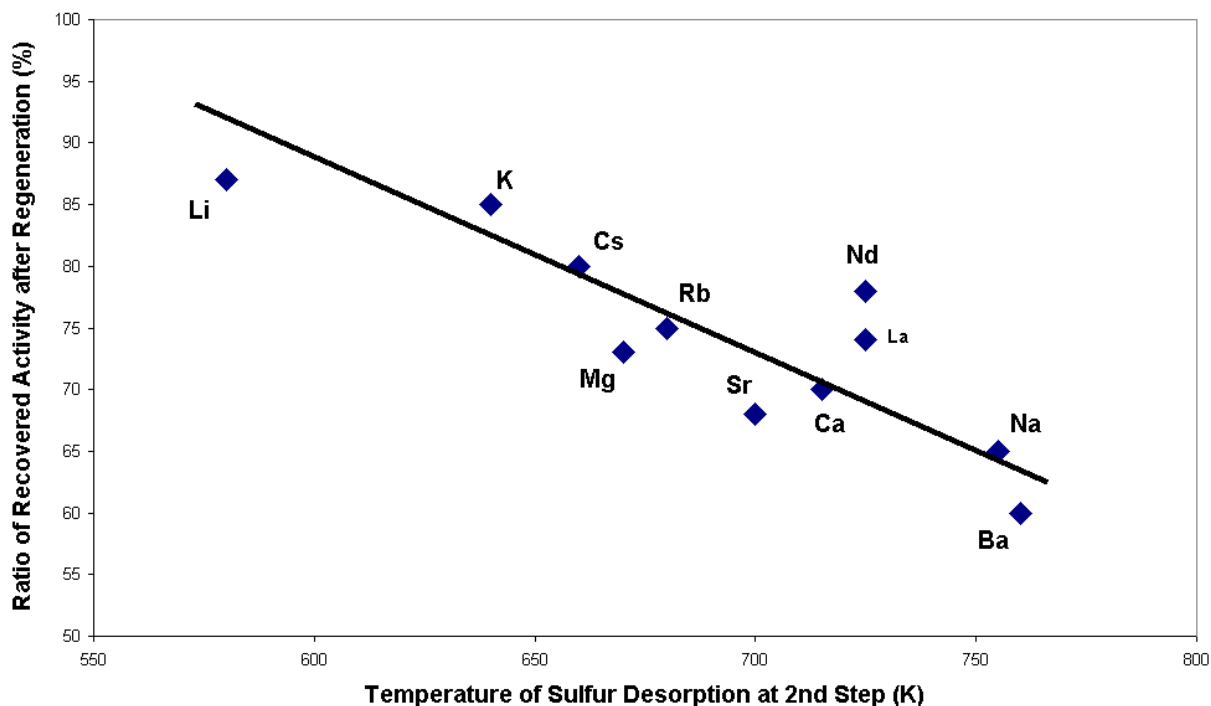




Figure 2 indicates that the sulfur compounds were desorbed from the metal oxide support (2<sup>nd</sup> Step of the sulfur desorption in the plot) at a lower temperature for lithium doped  $\gamma$ -Al<sub>2</sub>O<sub>3</sub> and the recovery of the activity of the catalyst with lithium doped  $\gamma$ -Al<sub>2</sub>O<sub>3</sub> was better than the others. Even though Ba forms the most stable nitrate, it forms an even more stable sulfate with the least amount of NO<sub>x</sub> capacity recovery. Thus the material with the largest NO<sub>x</sub> capacity may not be the best material of choice due to the sensitivity to sulfur.

The current Japanese market catalyst employs the combination of 33 mol% TiO<sub>2</sub> and 67 mol% of Li/ $\gamma$ -Al<sub>2</sub>O<sub>3</sub> because the temperature of the catalyst equipped to a lean burn engine in Japan is usually below 973K. At temperatures greater than 973K, the thermal degradation of TiO<sub>2</sub> dominates the NO<sub>x</sub> storage capacity, while below this temperature the activity is increased due to improved sulfur tolerance with the changed surface chemistry of the TiO<sub>2</sub> and  $\gamma$ -Al<sub>2</sub>O<sub>3</sub> combination.

Yamazaki et al studied the effect of various transition metals and the effect of Selective Catalytic Reduction (SCR) and NO<sub>x</sub>SR activity [24]. Based on this study, Fe, Ni, Co does not improve the NO<sub>x</sub> conversion for NSR or SCR in the absence of sulfur. After aging, the sulfur content of the Pt/Ba/Fe/Al<sub>2</sub>O<sub>3</sub> is equal to Pt/Ba/Al<sub>2</sub>O<sub>3</sub>, but the sulfur content of Pt/Ba/Fe/Al<sub>2</sub>O<sub>3</sub> after exposure to a reducing gas is about ½ that of the Pt/Ba/Al<sub>2</sub>O<sub>3</sub> exposed to the same gas. The larger the Fe loading (up to 18%) the lower the SO<sub>2</sub> desorption temperature and the smaller is the BaSO<sub>4</sub> particle size due to particle growth inhibition. Based on their SEM study, sulfur was only observed where Fe<sub>2</sub>O<sub>3</sub> was not present [24].

### **Investigation of the Oxide Surfaces via Probe Molecules**

The use of probe molecules to characterize the surface of metal oxides is well documented. In NO<sub>x</sub> adsorber catalysis, most of the literature indicates that basicity is one of the

major drivers for the choice of the storage oxide. The more basic the oxide, the larger the  $\text{NO}_x$  adsorption capacity, which leads to a more thermally stable nitrate [25].  $\text{CO}_2$  adsorption is well documented as an effective method to characterize the basicity of the surface of an oxide. Wang et al. looked at the defect structure of  $\text{MgO}$  and characterized the total basicity by the adsorption/desorption of  $\text{CO}_2$  as well as the nature of the site that  $\text{CO}_2$  binds to the surface [26]. Horuchi et al reviewed the driving forces for the electrostatic interaction between  $\text{CO}_2$  and the oxygen anions of the surface of a metal oxide, further documenting the capability of  $\text{CO}_2$  to look at the relative basicity of various electropositive metals. The molecular structures of the surface of metal oxide species are critical to the performance of each catalytic system. Infrared spectroscopy can be used to characterize the presence of  $\text{M}=\text{O}$  and bridging  $\text{M}-\text{O}-\text{M}$  vibrations along with determining the location of the surface metal oxide species by directly monitoring the specific surface hydroxyls of the support that are being titrated. IR is typically more useful for adsorbates, and Raman scattering for metal-oxygen vibrations due to their different selection rules. This fundamental information is critical for the development of molecular-structure – reactivity relationships for supported metal oxide catalysts. Under reaction conditions, the surface metal oxide species can be unchanged, hydrated, reduced to a lower oxidation state or transformed to a crystalline phase, each providing a unique interaction with adsorbates like  $\text{CO}_2$ ,  $\text{H}_2\text{O}$ , and  $\text{NO}_2$  [27].

Hodjati et al. looked at a series of barium aluminates for  $\text{NO}_x$  sorption [28]. They concluded that the electronic environment of Barium oxide plays a major role in its  $\text{NO}_x$  sorption properties. They showed that if barium is engaged in a strong bond with aluminum or tin, it will be protected against carbonate formation. The second point of difference concerns the structure and stability of the nitrate formation. If the barium is integrated with the structure of the support

and not just an oxide on the surface of a support, two varieties of nitrate are formed, the most abundant resulting from an N-bounded nitrate. This species does not exist on the bulk BaO. The formation of such a species could be explained by the presence of free oxygen vacancies on barium aluminate or BaSnO<sub>3</sub>, in which case NO<sub>2</sub> behaves as a Lewis acid and reacts with those vacancies as: Ba-O + NO<sub>2</sub> -> O-Ba-NO<sub>2</sub>. These sites are solely used for NO<sub>2</sub> sorption and not for CO<sub>2</sub>, and as a result, the competition between nitrates and carbonates formation is suppressed [28].

In our investigations, we wanted to understand the nature of the basicity that drives the NO<sub>x</sub> adsorption process and attempt to characterize the interaction of the metal oxide surface with a basic probe, like CO<sub>2</sub>, in comparison to a mixed oxide gas system. This allows the comparison of the type of basic sites on the surface of the metal oxide and the total capacity for CO<sub>2</sub> adsorption with the capacity and sites available for NO<sub>2</sub> adsorption.

## **Chapter I: Characterization of (Mg,Al) Oxides as NO<sub>x</sub> Storage Materials using Temperature-Programmed Desorption**

Bryan A. Silletti,<sup>1</sup> Susan Sigmon, James J. Spivey,<sup>2</sup> and H. Henry Lamb\*

Department of Chemical Engineering,  
North Carolina State University  
Raleigh, NC 27695 USA

\*Author to whom correspondence should be addressed.

Phone: (919)-515-6395  
Fax: (919)-515-3465  
e-mail: lamb@eos.ncsu.edu

<sup>1</sup>Present Address: Caterpillar Inc., Mossville, Illinois

<sup>2</sup>Present Address: Department of Chemical Engineering, Louisiana State University, Baton Rouge, LA

## ABSTRACT

The role of surface basicity of the storage component in  $\text{NO}_x$ SR catalysts was investigated by temperature programmed desorption (TPD) on  $\text{Al}_2\text{O}_3$ ,  $\text{MgO}$ , a hydrotalcite-derived Mg-Al oxide,  $\text{MgO}/\text{Al}_2\text{O}_3$  and  $\text{BaO}/\text{Al}_2\text{O}_3$ . Adsorption of  $\text{CO}_2$  and  $\text{NO}_2$  from a simulated exhaust gas mixture (mixed gas) containing 20%  $\text{CO}_2$ , 12%  $\text{O}_2$ , 1000 ppm  $\text{NO}_2$  (balance He) was compared to the adsorption of  $\text{CO}_2$  from 20%  $\text{CO}_2$  in He on the mixed oxides. The goal was to understand the chemical nature of the  $\text{NO}_x$  adsorption sites under simulated lean-burn conditions at various exhaust temperatures. The results indicate that the total basic site density probed via  $\text{CO}_2$  does not fully account for the  $\text{NO}_2$  adsorption capacity, although there is an overlap of 20 – 50% depending on the oxide and the adsorption temperature. Thus,  $\text{CO}_2$  does not compete with  $\text{NO}_2$  for the majority of the  $\text{NO}_x$  adsorption sites. The more strongly basic sites, however, that desorb  $\text{CO}_2$  at temperatures greater than  $250^\circ\text{C}$  exhibit a better correlation with the total  $\text{NO}_x$  capacity on  $\text{MgO}$ , HT, and  $\text{MgO}/\text{Al}_2\text{O}_3$ . On  $\text{BaO}/\text{Al}_2\text{O}_3$ , however, the difference between  $30^\circ\text{C}$  and  $290^\circ\text{C}$  adsorption of  $\text{CO}_2$  from the mixed gas less than 20%. This indicates that on the most basic oxide, there is a greater dependence on  $\text{CO}_2$  and significant competition for the same active sites. It was also demonstrated that a more weakly bound  $\text{NO}_2^-$  species is formed on all the metal oxides that desorbs as  $\text{NO}$  at moderate temperatures ( $100 - 300^\circ\text{C}$ ) and a surface nitrate species that decomposes at  $400\text{-}500^\circ\text{C}$  with evolution of  $\text{NO} + \text{O}_2$ .

## Introduction

$\text{NO}_x$  emissions from internal combustion engines are a major contributor to acid rain (ranking second only to sulfur compounds), and  $\text{NO}_x$  compounds foster the generation of photochemical oxidants such as ozone and peroxyacetyl nitrate in the troposphere. On road vehicles account for nearly 50% of ambient  $\text{NO}_x$  emissions and thus has been a significant target for EPA legislation [1]. Three-way exhaust catalysts have been effective in reducing  $\text{NO}_x$  emissions from spark ignition (SI) engines that operate under stoichiometric conditions [29]. Conforming to increasingly stringent standards on  $\text{NO}_x$  exhaust emissions has proven more difficult for diesel engines because they operate under fuel lean (oxygen-rich) conditions. Legislation requiring a 95% decrease in  $\text{NO}_x$  emissions from diesel engines and the automotive industry's shift toward lean-burn SI engines have created the need for new approaches to  $\text{NO}_x$  emission reduction [1]. One such alternative is the  $\text{NO}_x$  storage reduction ( $\text{NO}_x\text{SR}$ ) catalyst or  $\text{NO}_x$  trap.  $\text{NO}_x\text{SR}$  catalysts oxidize NO to  $\text{NO}_2$  and store the  $\text{NO}_2$  as a nitrate in an oxygen-rich combustion gas environment containing  $\text{NO}_x$ ,  $\text{O}_2$ ,  $\text{H}_2\text{O}$ ,  $\text{SO}_2$ ,  $\text{CO}_2$ , and  $\text{N}_2$ . Subsequently, during a brief fuel-rich exhaust cycle, the nitrate species is decomposed and the byproducts are reduced to  $\text{N}_2$  and  $\text{O}_2$  by a reductant ( $\text{CO}$ ,  $\text{H}_2$ , other).

Characterization of the interaction of metal oxide supports with the metal catalyst is becoming increasingly important not only to obtain optimal catalyst systems, but also to define the relationship between catalytic activity and surface structure [30]. In many catalytic systems, the performance is known to depend not only on the inherent catalytic activity of the active phase, but also on the textural and physicochemical properties of the support [30]. For this reason, we employed the use of CO<sub>2</sub> and NO<sub>2</sub> adsorption via temperature programmed desorption (TPD) to understand the nature of the sites that are active for NO<sub>x</sub>SR catalysts. Gaseous CO<sub>2</sub> is a linear molecule with high electron density surrounding the oxygen atom thus creating an electrophilic carbon atom at its center. This carbon atom acts as a weak acid to probe effectively all basic surface sites on porous catalysts. Gaseous NO<sub>2</sub> exhibits complex chemistry and at room temperature it is a paramagnetic gas that dimerizes reversibly to N<sub>2</sub>O<sub>4</sub> [31]. NO<sub>2</sub> exhibits a bent planar structure with a free electron localized around the N atom. In addition, due to the lone unpaired electron, NO<sub>2</sub> can act both as an electron donor to become isoelectronic with O<sub>2</sub> or act as an electron acceptor to obtain a more stable 18e<sup>-</sup> configuration [31]. As a result, NO<sub>2</sub> will be active for both Lewis base and acid sites as well as defect sites. It is these characteristics that will be explored in this investigation.

For our catalysts, we chose Mg and Al mixed oxides due to the potential for improved sulfur tolerance and compared them to BaO/Al<sub>2</sub>O<sub>3</sub> [32, 33]. Hydrotalcites are naturally occurring anionic clays which can be expressed with the general formula,  $[M_x^{2+}M^{3+}(\text{OH})_{2x+2}]^+[A_{1/n}^{n-}\cdot\text{H}_2\text{O}]^-$  where x is the M<sup>2+</sup>/M<sup>3+</sup> ratio [34]. Most commercial hydrotalcites resemble the naturally occurring compound, Mg<sub>6</sub>Al<sub>2</sub>(OH)<sub>16</sub>CO<sub>3</sub>·4H<sub>2</sub>O, resembling the structure of brucite, Mg(OH)<sub>2</sub> [35]. Also known as layered double hydroxides, hydrotalcites consist of positively charged brucite-like layers between negatively charged layers of anions and water [36]. For mixed Mg,Al

oxides, we used both MgO doped Al<sub>2</sub>O<sub>3</sub> and a commercial hydrotalcite. Using these mixed Mg, Al oxides and temperature programmed desorption (TPD), we investigated the temperature-dependent adsorption processes of CO<sub>2</sub> and NO<sub>2</sub> on basic oxide surfaces.

## **Experimental Methods**

### *Materials*

MgO (Magchem AD200, Martin Marietta), Catapal A alumina (Vista Chemicals), and a commercial hydrotalcite (HT), with a Mg:Al ratio of 7:3, were used as received. The HT was calcined in flowing O<sub>2</sub> at 150 mL/min with a 4°C/min ramp rate from 30°C to 600°C and soaked for 2 hours. A sol-gel Al<sub>2</sub>O<sub>3</sub> was synthesized using aluminum isopropoxide and 2-methyl-2,4-pentanediol; the resulting powder was calcined at 700°C for 2 h. This method yields alumina with a surface area of 230 m<sup>2</sup>/g, a pore volume of 1.1 cc/g, an average pore diameter of 14 nm and no detectable sulfur impurities [37]. Subsequently, the sol-gel Al<sub>2</sub>O<sub>3</sub> was impregnated with Mg and Ba via incipient wetness using the quantities of Mg(NO<sub>3</sub>)<sub>2</sub> and Ba(NO<sub>3</sub>)<sub>2</sub> to obtain 5 mmol MgO per gram Al<sub>2</sub>O<sub>3</sub> (MgO/Al<sub>2</sub>O<sub>3</sub>) and 5 mmol BaO per gram Al<sub>2</sub>O<sub>3</sub> (BaO/Al<sub>2</sub>O<sub>3</sub>), respectively. Each sample was then calcined in O<sub>2</sub> at 600°C for 2 h.

### *Characterization*

X-ray diffraction patterns for each of the calcined solids were recorded using a INEL XRG 3000 with a CPS 120 Detector and a Germanium Crystal Monochromator provided by Dr. James Martin from the Inorganic Chemistry department at NC State University. A Fine Focused 1500 Watt Cu Tube was used at 30mA and 34.8 kV. The calcined sample was placed in the XRD and allowed to collect the diffraction pattern for 2 h at all 2θ values. The specific surface



areas of the catalysts were determined by nitrogen adsorption at 77 K using a Micromeritics Flow Sorb II 2300 analyzer and the single-point Brunauer-Emmett-Teller (BET) method. Each sample was pretreated at 200°C until no further weight loss was recorded before being transferred to the sample tube for N<sub>2</sub> adsorption.

### *Temperature-Programmed Desorption*

TPD experiments were performed in a fixed bed microreactor consisting of a fritted quartz tube mounted in a vertical Lindberg furnace that is controlled by an Omega PID controller and a solid-state contactor. The catalyst bed temperature is measured using a Type K thermocouple interfaced to a PC via a Metrabyte device. The reactor effluent was sampled continuously using a quadrupole mass spectrometer (QMS) with a high-pressure gas inlet system (Pfeiffer vacuum). A certified gas mixture (National Welders) containing 1000 ppm NO<sub>2</sub>, 20% CO<sub>2</sub>, 12% O<sub>2</sub> in balance He was used in NO<sub>2</sub> TPD experiments. A blended mixture containing ~20% CO<sub>2</sub> in He was used in CO<sub>2</sub> TPD experiments. Ultrahigh purity He and CO<sub>2</sub> were supplied by National Welders. Gases were metered using calibrated flow meters (rotameters).

In each experiment, 200 mg of metal oxide powder was placed in a quartz reactor tube and pretreated in He at 30 mL/min (NTP) to 550°C and soaked for 1 h. The sample was then cooled to the desired adsorption temperature (30, 100 or 290°C) in flowing He and exposed to either the NO<sub>2</sub> mixed gas or CO<sub>2</sub> in He at 45 mL/min for 30 min. After adsorption, the catalyst was purged in flowing He (30 mL/min) temperature for 40 min and then cooled to ~30°C. The sample temperature was then linearly ramped at 10°C/min to 550°C.

## Results

The XRD patterns of the samples are shown in Figure 1.1. The XRD pattern of MgO is characteristic of periclase with strong diffraction peaks at 43 and 62° two-theta. The diffraction pattern of the sol-gel Al<sub>2</sub>O<sub>3</sub> is characteristic of  $\gamma$ -Al<sub>2</sub>O<sub>3</sub> albeit with a significant percentage of amorphous material. The XRD pattern of the Catapal A boehmite [AlO(OH)] is before calcining and thus the results indicate a nearly amorphous transitional Al<sub>2</sub>O<sub>3</sub> phase. The XRD pattern of the MgO/Al<sub>2</sub>O<sub>3</sub> evidences an increase in crystallinity of the  $\gamma$ -Al<sub>2</sub>O<sub>3</sub> phase and a small shift in peak locations consistent with an increase in the lattice parameter. In addition, a surface spinel phase was detected using the peaks at 31, 27, 45, and 60°. The material derived by heating the commercial hydrotalcite to 600°C in O<sub>2</sub> exhibited strong, sharp diffraction peaks at 50 74, 89, and 95° two-theta. This phase is unique to the HT, but is representative of an 8 – 12° shift of all the major peaks that define the MgO pattern. Lastly, the BaO/Al<sub>2</sub>O<sub>3</sub> XRD pattern indicates the presence of Al<sub>2</sub>O<sub>3</sub>, BaO, and a mixed barium aluminate phase.

The specific surface areas of the metal oxides investigated in this study are given in Table 1.1. The single-point BET results have been confirmed by multi-point BET analyses for selected samples. The Catapal A and sol-gel transitional aluminas have specific surface areas of approximately 250 m<sup>2</sup>/g. Addition of Mg (and Ba) to the sol-gel alumina reduced the specific surface area (after calcination) to 187 m<sup>2</sup>/g (197 m<sup>2</sup>/g) consistent with particle sintering (and the increase in crystallinity observed by XRD). The surface areas of the MgO and HT-derived Mg-Al mixed oxide are approximately 180 m<sup>2</sup>/g.

Figure 1.2 shows the TPD spectra of all the metal oxides after CO<sub>2</sub> adsorption at 30°C. The CO<sub>2</sub> desorption peaks of the sol-gel and boehmite-derived aluminas appear at 40°C and the majority of the capacity is below 100°C and representative of weakly bound (physically

adsorbed) CO<sub>2</sub>. The aluminas exhibit similar weak CO<sub>2</sub> desorption tails that are associated with relatively low densities of moderately basic surface sites. A narrow low-temperature CO<sub>2</sub> desorption peak is also observed for the MgO and BaO-modified sol-gel aluminas suggesting that these surfaces retain significant alumina character. The MgO and the HT-derived Mg-Al oxide do not exhibit a desorption peak at 40°C but instead have a smaller broader peak at 70°C and a much stronger CO<sub>2</sub> desorption tail at higher temperatures. The MgO also has a CO<sub>2</sub> desorption peak at 500°C, while the BaO/Al<sub>2</sub>O<sub>3</sub> exhibits a higher temperature tail of CO<sub>2</sub> desorption. The MgO/Al<sub>2</sub>O<sub>3</sub> has the largest capacity, 501 μmol/g, but BaO/Al<sub>2</sub>O<sub>3</sub> has the highest CO<sub>2</sub> desorption temperature, indicating the most basic sites.

Figure 1.3 compares the TPD spectra of all samples after CO<sub>2</sub> adsorption at 100°C. MgO had the largest total capacity at 305 μmol/g and exhibited CO<sub>2</sub> desorption peaks at 100, 200, and 450°C. The MgO/Al<sub>2</sub>O<sub>3</sub> had significantly diminished capacity due to the loss of the very weakly bound CO<sub>2</sub> below 100°C. It had the second largest capacity at 260 μmol/g with two similar low temperature CO<sub>2</sub> desorption peaks at 125 and 175°C, followed by a desorption tail of mixed CO<sub>2</sub> species. The remaining materials all demonstrated one peak desorption temperature and a subsequent tail of CO<sub>2</sub> desorption. The HT was similar in capacity to the MgO/Al<sub>2</sub>O<sub>3</sub> while the sol-gel and Catapal alumina had significantly reduced capacity at 136 and 77 μmol/g, respectively.

Figure 1.4 depicts the TPD spectra after CO<sub>2</sub> adsorption at 290°C. In this case, only MgO, MgO/Al<sub>2</sub>O<sub>3</sub> and BaO/Al<sub>2</sub>O<sub>3</sub> adsorb CO<sub>2</sub> in the 20% CO<sub>2</sub> in balance He at 103, 68 and 211 μmol/g (as given by Table 1.5). In the mixed gas, little to no CO<sub>2</sub> is desorbed from the Mg based oxides (< 16 μmol/g), while 182 μmol/g is desorbed on the Ba-doped alumina. The BaO/Al<sub>2</sub>O<sub>3</sub> still has significant CO<sub>2</sub> capacity at 290°C and still competes actively sites with NO<sub>2</sub>.

Figure 1.5 shows TPD spectra recorded following adsorption of  $\text{CO}_2 + \text{NO}_2$  at  $30^\circ\text{C}$  from the mixed gas onto sol-gel  $\text{Al}_2\text{O}_3$  and the boehmite-derived transitional alumina. On both aluminas, a high-temperature TPD peak is observed at  $360^\circ\text{C}$  which is associated with evolution of  $\text{NO}$  and  $\text{O}_2$  in approximately a 1.8:1 molar ratio. This stoichiometry is higher than the expected ratio of 1.33:1, but the character is consistent with the ratio of 1.45 that was observed with the decomposition of bulk magnesium nitrate as depicted in the Appendix II. Two low-temperature  $\text{NO}$  desorption peaks are observed: a broad asymmetric peak near  $50^\circ\text{C}$  and a well-defined peak that appears at  $\sim 175^\circ\text{C}$  on the boehmite-derived alumina and at  $\sim 190^\circ\text{C}$  for the sol-gel alumina. Neither of these  $\text{NO}$  desorption states is accompanied by  $\text{O}_2$  (or  $\text{NO}_2$ ) desorption.

The mixed gas TPD experiment was repeated at an adsorption temperature of  $100^\circ\text{C}$  and  $290^\circ\text{C}$ , and the results are shown in Figures 1.6 and 1.7, respectively. At  $100^\circ\text{C}$ , the  $\text{CO}_2$  adsorption capacity is significantly reduced, however, the remaining capacity is reflective of stronger basic sites. Again, the difference in capacity between the single-component  $\text{CO}_2$  adsorption relative to the mixed gas  $\text{CO}_2$  adsorption is associated with stronger basic sites. At  $290^\circ\text{C}$ , there is negligible adsorption of  $\text{CO}_2$  on either alumina. As seen in Table 1.3, the total  $\text{NO}_2$  adsorption is still higher than  $\text{CO}_2$  adsorption. The boehmite-derived alumina has a slightly larger  $\text{NO}$  desorption peak relative to the sol-gel alumina (131 vs. 92, respectively), but the thermal stability of the adsorbed species are both at  $375^\circ\text{C}$ , when adsorbed at  $100^\circ\text{C}$ . The  $\text{NO} + \text{O}_2$  TPD peak associated with the boehmite-derived alumina shifts to a slightly higher temperature ( $390^\circ\text{C}$  versus  $375^\circ\text{C}$ ) following  $\text{NO}_2$  adsorption at  $290^\circ\text{C}$ , while the sol-gel alumina is consistently at  $375^\circ\text{C}$ . In addition, the boehmite-derived alumina consistently exhibits a “tail” on the high-temperature  $\text{NO}$  and  $\text{O}_2$  desorption peaks.

Table 1.3 summarizes the CO<sub>2</sub> and NO<sub>2</sub> adsorption capacities of the aluminas under all testing conditions. Based on this data, sol-gel alumina had a 40% greater total CO<sub>2</sub> adsorption capacity relative to the boehmite-derived alumina, but the majority of the adsorbed species was very weakly bound CO<sub>2</sub> with a desorption temperature below 100°C. The total NO<sub>2</sub> adsorption capacity of the sol-gel alumina at 30°C is also larger than the boehmite-derived alumina. By comparing the quantity of CO<sub>2</sub> desorbed following CO<sub>2</sub> and NO<sub>2</sub> mixed gas adsorption at room temperature, there was about a 45% reduction in total CO<sub>2</sub> capacity that we infer was due to the competitive adsorption of NO<sub>2</sub>. This reduction in CO<sub>2</sub> adsorption capacity, however, does not account completely for the NO<sub>2</sub> adsorption capacity.

TPD spectra measured following mixed gas adsorption at 30°C on MgO, HT-derived Mg-Al oxide, MgO/Al<sub>2</sub>O<sub>3</sub>, and BaO/Al<sub>2</sub>O<sub>3</sub> at 30°C are shown in Figure 1.8 and the results are in Table 1.4. The difference in CO<sub>2</sub> capacity between the mixed gas adsorption and CO<sub>2</sub> in He adsorption accounts for approximately 50% of the total NO capacity on MgO and MgO/Al<sub>2</sub>O<sub>3</sub>, while minimal differences are noted on the HT and BaO/Al<sub>2</sub>O<sub>3</sub>. Qualitatively, the peaks are similar to Al<sub>2</sub>O<sub>3</sub> as there is a low temperature NO desorption along with a high temperature NO + O<sub>2</sub> evolution for each sample. Figure 1.9 and table 1.5 shows the competitive adsorption of CO<sub>2</sub> in the presence of NO<sub>2</sub> more clearly at 100°C. The CO<sub>2</sub> probed sites reflect a larger number of medium strength basic sites (200°C – 400°C). These sites, however, account for only a small portion (<30%) of the NO<sub>2</sub> adsorption sites.

Figure 1.10 documents the sites still available for mixed gas adsorption at 290°C. BaO-modified alumina, MgO and MgO-modified alumina are the only samples to adsorb CO<sub>2</sub> at 290°C, but only BaO-doped alumina adsorbed CO<sub>2</sub> from the NO<sub>2</sub> mixed gas. At 290°C adsorption, there is no stable surface nitrite species and only the nitrate capacity is represented by

the NO capacity. Lastly, in Figure 1.11, the time and temperature dependencies of the adsorption of NO<sub>2</sub> and CO<sub>2</sub> were studied when the NO<sub>2</sub> mixed gas is adsorbed on MgO and MgO/Al<sub>2</sub>O<sub>3</sub> at 290°C and the sample was allowed to cool down in the mixed gas to 30°C.

## Discussion

The XRD and BET results evidence that the precursor composition and calcination conditions significantly affect the crystalline phase(s) and specific surface areas of the metal oxides. The transitional aluminas exhibit similar weak CO<sub>2</sub> desorption tails that are associated with small concentration densities of moderately basic surface sites. The narrow low-temperature CO<sub>2</sub> desorption peak that is very consistent on both the aluminas is also observed for the MgO and BaO-modified sol-gel aluminas, suggesting that these surfaces still retain significant alumina character. CO<sub>2</sub> TPD after adsorption at 100°C provides a more direct measure of the surface sites with basic character. These species are associated with more strongly bound CO<sub>2</sub> and higher basicity. Based on the results for MgO, HT, and BaO/Al<sub>2</sub>O<sub>3</sub>, increasing Mg or Ba content increases the surface basicity. In addition, the Mg that is bound in the HT-derived Mg-Al oxide does not exhibit the large low temperature CO<sub>2</sub> desorption peak that was present on the MgO-modified sol-gel alumina but resembles the character of the MgO sample with a lower overall capacity. As a result, the HT exhibits a bimodal distribution of medium strength basic sites (100°C – 350°C) without either the low temperature alumina peak or the high temperature tail on the MgO, BaO, and MgO/ Al<sub>2</sub>O<sub>3</sub>. The BaO/Al<sub>2</sub>O<sub>3</sub> is the most basic with the largest capacity of CO<sub>2</sub> after 290°C, and is consistent with the differences in the electronegativity of the metal oxides.

After the NO<sub>2</sub> mixed gas adsorption on the aluminas, there are multiple NO<sub>x</sub> desorption states, a low temperature NO desorption peak and a high temperature NO + O<sub>2</sub> peak in a ratio of approximately 1.6 : 1. The stoichiometry of the magnesium nitrate in Appendix II is 1.45. We associate the high-temperature desorption peak with decomposition of a surface nitrate species [38]. The stoichiometry of bulk aluminum nitrate decomposition is  $2\text{Al}(\text{NO}_3)_3 \rightarrow \text{Al}_2\text{O}_3 + 6\text{NO} + \frac{9}{2}\text{O}_2$ , which yields a ratio of 1.33:1. Although the nitrate formation is not thermally activated, the nitrate does require another oxygen either from the oxide surface or from another NO<sub>2</sub> species to be formed. This oxygen is obtained either from the reaction of 2 NO<sub>2</sub> molecules or from the surface of the oxide. If the oxygen is obtained from the reaction of the NO<sub>2</sub> molecules, the bulk stoichiometry require for nitrate formation would be as follows:  $6\text{NO}_2 \rightarrow 3\text{NO}_3 + 3\text{NO}$ , whereby an equivalent low temperature NO peak and high temperature nitrate decomposition peak might be expected [39]. By comparing the areas of the low-temperature and high-temperature NO TPD peaks we find them to be inequivalent. Thus, the low temperature NO desorption is most likely associated with a surface nitro (NO<sub>2</sub><sup>-</sup>) species that irreversibly desorbs as NO from the surface, but may participate in the nitrate formation at higher temperatures. The NO evolution implies that a vacant surface coordination site has been filled by O.

The difference in capacity between CO<sub>2</sub> in He adsorption and the CO<sub>2</sub> in the mixed gas on the alumina sample is Difference between the NO<sub>2</sub> and CO<sub>2</sub> adsorption sites on the aluminas can be partially explained by the fact that NO<sub>2</sub> is a strong oxidizing agent that can oxidize surface defect sites and be subsequently desorbed as NO [40]. Also, γ-alumina does have a large population of defect sites due to its defect spinel structure, and these sites will be active for electron donation from NO<sub>2</sub> that are not active for CO<sub>2</sub> adsorption.

Similarly to the aluminas, the (Mg, Ba)Al oxides exhibit at least one moderate- to low-temperature NO desorption peak (without concomitant O<sub>2</sub> desorption) and a high-temperature NO + O<sub>2</sub> desorption peak associated with a surface nitrate species are observed. MgO exhibits both a low-temperature and an intermediate temperature NO desorption peak. The intermediate temperature NO desorption peaks on MgO, HT-derived Mg-Al oxide, and BaO/alumina appear at higher temperatures than on the MgO/ Al<sub>2</sub>O<sub>3</sub>; however, the peaks were much broader and less defined. The low-temperature NO TPD peak for MgO/ Al<sub>2</sub>O<sub>3</sub> is similar to that of the unmodified alumina support. This seems to indicate that there is a tight distribution of active sites on alumina for low temperature adsorption of NO<sub>2</sub><sup>-</sup> species at specific defect sites or weakly basic sites. The Al-based sites in the HT are bound differently, as can be seen by the differences in the diffraction pattern between HT and MgO/ Al<sub>2</sub>O<sub>3</sub>, and do not give rise to the same low temperature NO distribution. Table 4 provides a summary of all the RT TPD results for the mixed oxide samples. The relative thermal stability of the nitrate species on each of the samples is given as follows: Al<sub>2</sub>O<sub>3</sub> < MgO/Al<sub>2</sub>O<sub>3</sub> < MgO < HT3 < BaO/Al<sub>2</sub>O<sub>3</sub>, but the overall capacity was greatest on MgO.

In general, the more strongly basic sites as measured by CO<sub>2</sub> TPD are lost to NO<sub>2</sub> competitive adsorption, whereas the low-temperature (more weakly bound) CO<sub>2</sub> states are largely unaffected by NO<sub>2</sub> competitive adsorption. NO<sub>2</sub> adsorbs at strongly basic sites, but NO<sub>2</sub> also adsorbs at sites that are not active for CO<sub>2</sub> adsorption. NO<sub>2</sub> molecules have a significantly larger electron affinity and bind more strongly at the basic metal sites and this occurs even with a 200X difference in concentration from 20% CO<sub>2</sub> to 0.1% NO<sub>2</sub>. The difference between the CO<sub>2</sub> capacities on BaO/Al<sub>2</sub>O<sub>3</sub> however, is very similar to the total NO<sub>x</sub> storage capacity (36 vs. 29 μmols/g). For the Mg oxides, that the most basic sites, as measured by CO<sub>2</sub> adsorption at



290°C, are all more active for NO<sub>2</sub> adsorption than CO<sub>2</sub> adsorption. The CO<sub>2</sub> capacity on the Mg oxides, however, only accounts for approximately 50% of the total NO<sub>2</sub> adsorbed, while on the BaO/Al<sub>2</sub>O<sub>3</sub>, it accounts for over 75% of the nitrate capacity. The pure CO<sub>2</sub> capacity at 290°C is characteristic of Lewis Basicity and the difference between the mixed gas CO<sub>2</sub> and CO<sub>2</sub> in He capacity must be associated with the Lewis basic sites that are adsorbed by NO<sub>2</sub>. The remaining NO<sub>x</sub> storage capacity must occur via defect sites, Lewis acid sites and other mechanisms that are not necessarily driven purely by basicity.

In figure 1.11, both MgO and MgO/Al<sub>2</sub>O<sub>3</sub> have been saturated with NO<sub>2</sub> forming a different species that desorbs at lower temperature with a higher NO:O<sub>2</sub> ratio than the surface nitrate species present after 30 minutes of adsorption at 290°C. O<sub>2</sub> desorbed at lower temperature indicating that oxidation had saturated the surface and the remainder was removed in a stoichiometric form. This provides insight into the differences in the sites that are active for NO<sub>2</sub> adsorption. MgO/Al<sub>2</sub>O<sub>3</sub> desorbed less O<sub>2</sub> at both low and high temperature. The sample was so saturated that low temperature physisorbed NO<sub>2</sub> was also present on the sample. When comparing the capacity for CO<sub>2</sub> storage, the amount of CO<sub>2</sub> was less than the amount of CO<sub>2</sub> that was adsorbed for 30 minutes at room temperature. This indicates that with increasing amount of exposure to the mixed gas, NO<sub>2</sub> will continue to dominate the adsorption process, but there are still basic sites active for CO<sub>2</sub> adsorption that are not displaced by NO<sub>2</sub>. Consequently, the unpaired electron on the polar NO<sub>2</sub> molecule is demonstrating that, even though NO<sub>2</sub> is active for Lewis basic sites, it is also active for Lewis acid sites by donating the electron for bonding. The unique character of the NO<sub>2</sub> molecule also allows it to adsorb on many different sites on the samples that will not adsorb the basic probe CO<sub>2</sub>.

## Conclusions

Single-component CO<sub>2</sub> adsorption at RT, 100°C, and 290°C, relative to the competitive adsorption of CO<sub>2</sub> in the presence of NO<sub>2</sub>, yields a larger number of medium strength basic sites (200°C – 400°C). These more strongly bound CO<sub>2</sub> species, though, only account for a small portion (< 40%) of the NO<sub>2</sub> adsorption sites with the exception of BaO/Al<sub>2</sub>O<sub>3</sub> where there is a stronger correlation between the surface bound CO<sub>2</sub> sites and the surface bound NO<sub>2</sub> sites at 290°C. NO<sub>2</sub> molecules have a significantly larger electron affinity (~2.3eV) and can also bind more strongly at the basic metal sites that are not as readily susceptible to CO<sub>2</sub> adsorption. Even though NO<sub>2</sub> is active for Lewis basic sites, it is also active for Lewis acid and vacancy sites by donating the electron for bonding due to the unique character of the NO<sub>2</sub> molecule. These sites are not active for CO<sub>2</sub> adsorption. In addition, based on our studies, as the exposure time to the NO<sub>2</sub> mix gas increases, the amount of NO<sub>2</sub> adsorbed increases, continuously displacing the surface bound carbonates and bicarbonates. Lastly, we have also demonstrated that NO<sub>2</sub> adsorption at room temperature is characterized by two states: low temperature NO desorption, bound as a surface nitrite species, that can oxidize the surface and irreversibly bound NO<sub>2</sub> that is stored as a surface nitrate. The nitrate decomposes to evolve stoichiometric NO + O<sub>2</sub> at high temperatures.

**Table 1.1: BET Surface Area**

Sample	Surface Area (m <sup>2</sup> /g)
MgO	179
MgO Al <sub>2</sub> O <sub>3</sub>	187
Commercial Hydrotalcite	188
BaO Al <sub>2</sub> O <sub>3</sub>	197
Sol-Gel – Al <sub>2</sub> O <sub>3</sub>	246
Catapal – Al <sub>2</sub> O <sub>3</sub>	252

**Table 1.2: XRD Peak Assignments**  
**2 $\Theta$  Peak Position (Relative %)**

<b>S- Al<sub>2</sub>O<sub>3</sub></b>	<b>33<sub>91</sub></b>	<b>37<sub>94</sub></b>		<b>46<sub>92</sub></b>	<b>61<sub>47</sub></b>	<b>67<sub>100</sub></b>				
$\gamma$ -Al <sub>2</sub> O <sub>3</sub>	32 <sub>20</sub>	37 <sub>59</sub>	39 <sub>22</sub>	46 <sub>80</sub>	61 <sub>20</sub>	66 <sub>100</sub>				
<b>MgO</b>	<b>32<sub>21</sub></b>	<b>37<sub>25</sub></b>	<b>43<sub>100</sub></b>	<b>63<sub>63</sub></b>	<b>74<sub>4</sub></b>	<b>78<sub>20</sub></b>	<b>94<sub>11</sub></b>			
Periclase		37 <sub>10</sub>	43 <sub>100</sub>	63 <sub>80</sub>	74 <sub>20</sub>	78 <sub>61</sub>	94			
<b>MgO/Al<sub>2</sub>O<sub>3</sub></b>	<b>32<sub>48</sub></b>	<b>37<sub>75</sub></b>	<b>46<sub>88</sub></b>	<b>60<sub>35</sub></b>	<b>67<sub>100</sub></b>		<b>78<sub>12</sub></b>	<b>84<sub>12</sub></b>	<b>95<sub>14</sub></b>	
Periclase		37 <sub>10</sub>	43 <sub>100</sub>	63 <sub>80</sub>		74 <sub>20</sub>	78 <sub>61</sub>		94	
MgAl <sub>2</sub> O <sub>4</sub>		37 <sub>100</sub>	45 <sub>66</sub>	60 <sub>40</sub>	65.5 <sub>76</sub>		78 <sub>28</sub>			
<b>HT</b>		<b>43<sub>17</sub></b>	<b>50<sub>100</sub></b>			<b>74<sub>64</sub></b>		<b>90<sub>7</sub></b>	<b>95<sub>17</sub></b>	
MgAl <sub>2</sub> O <sub>4</sub>	37 <sub>100</sub>	45 <sub>80</sub>	55 <sub>32</sub>	60 <sub>80</sub>	65.5 <sub>100</sub>	74 <sub>20</sub>	78 <sub>28</sub>			
Periclase	37 <sub>10</sub>	43 <sub>100</sub>			63 <sub>80</sub>	74 <sub>20</sub>	78 <sub>61</sub>		94	
<b>BaO/Al<sub>2</sub>O<sub>3</sub></b>	<b>24<sub>100</sub></b>	<b>28<sub>51</sub></b>	<b>34<sub>65</sub></b>	<b>37<sub>43</sub></b>	<b>40<sub>41</sub></b>	<b>42<sub>41</sub></b>	<b>46<sub>46</sub></b>	<b>55<sub>22</sub></b>	<b>61<sub>26</sub></b>	<b>67<sub>53</sub></b>
BaAl <sub>2</sub> O <sub>4</sub>		28 <sub>100</sub>	34 <sub>41</sub>		40 <sub>28</sub>		45 <sub>22</sub>	57 <sub>22</sub>	61 <sub>11</sub>	
BaO	26.5 <sub>100</sub>		33 <sub>82</sub>			43 <sub>82</sub>	46 <sub>8</sub>	56 <sub>82</sub>		69 <sub>40</sub>
$\gamma$ -Al <sub>2</sub> O <sub>3</sub>			32 <sub>20</sub>	37 <sub>59</sub>	39 <sub>22</sub>		46 <sub>80</sub>		61 <sub>20</sub>	66 <sub>100</sub>

**Table 1.3: Sol-Gel and Boehmite Alumina Comparison**

	20% CO <sub>2</sub> in He Capacity (μmols/g)	Mixed CO <sub>2</sub> Capacity (μmols/g)	Total NO Capacity (μmols/g)	NO Tdes (High)	High Temp NO Capacity (μmols/g)	NO:O <sub>2</sub> Ratio	NO Tdes (Low)	LT NO Capacity (μmols/g)
<b>S- Al<sub>2</sub>O<sub>3</sub> (30°C)</b>	<b>347</b>	<b>225</b>	<b>210</b>	<b>360</b>	<b>144</b>	<b>1.87</b>	<b>190</b>	<b>34</b>
<b>B- Al<sub>2</sub>O<sub>3</sub> (30°C)</b>	<b>248</b>	<b>138</b>	<b>156</b>	<b>360</b>	<b>104</b>	<b>1.74</b>	<b>175</b>	<b>41</b>
<b>S- Al<sub>2</sub>O<sub>3</sub> (100°C)</b>	<b>136</b>	<b>95</b>	<b>133</b>	<b>375</b>	<b>92</b>	<b>1.67</b>	<b>190</b>	<b>41</b>
<b>B- Al<sub>2</sub>O<sub>3</sub> (100°C)</b>	<b>77</b>	<b>93</b>	<b>167</b>	<b>375</b>	<b>131</b>	<b>1.80</b>	<b>190</b>	<b>36</b>
<b>S- Al<sub>2</sub>O<sub>3</sub> (290°C)</b>	<b>-</b>	<b>-</b>	<b>83</b>	<b>375</b>	<b>83</b>	<b>1.65</b>	<b>-</b>	<b>-</b>
<b>B- Al<sub>2</sub>O<sub>3</sub> (290°C)</b>	<b>-</b>	<b>-</b>	<b>88</b>	<b>390</b>	<b>88</b>	<b>1.70</b>	<b>-</b>	<b>-</b>

**Table 1.4: 30°C Comparison of Mixed Oxides**

	Mg:Al:Ba	20% CO <sub>2</sub> in He Capacity ( $\mu\text{mol}/\text{g}$ )	Mixed CO <sub>2</sub> Capacity ( $\mu\text{mol}/\text{g}$ )	Total NO Capacity ( $\mu\text{mol}/\text{g}$ )	NO Tdes (High)	High Temp NO Capacity ( $\mu\text{mol}/\text{g}$ )	NO:O <sub>2</sub> Ratio	NO Tdes (Low)	LT NO Capacity ( $\mu\text{mol}/\text{g}$ )
<b>MgO</b>	1:0:0	490	347	258	490	201	1.64	300	38
<b>MgO/ Al<sub>2</sub>O<sub>3</sub></b>	1:4:0	501	371	147	425	108	1.76	240	37
<b>HT</b>	7:3:0	229	246	114	510	75	1.44	280	36
<b>BaO/ Al<sub>2</sub>O<sub>3</sub></b>	0:2:1	487	515	62	525	62	1.50	-	-

**Table 1.5: 100°C Comparison of Mixed Oxides**

	Mg:Al:Ba	20% CO <sub>2</sub> in He Capacity ( $\mu\text{mol}/\text{g}$ )	Mixed CO <sub>2</sub> Capacity ( $\mu\text{mol}/\text{g}$ )	Total NO Capacity ( $\mu\text{mol}/\text{g}$ )	NO Tdes (High)	High Temp NO Capacity ( $\mu\text{mol}/\text{g}$ )	NO:O <sub>2</sub> Ratio	NO Tdes (Low)	LT NO Capacity ( $\mu\text{mol}/\text{g}$ )
<b>MgO</b>	1:0:0	305	274	137	475	104	1.77	300	32
<b>MgO/ Al<sub>2</sub>O<sub>3</sub></b>	1:4:0	260	248	138	440	99	1.62	275	39
<b>HT</b>	7:3:0	177	136	147	510	123	1.62	275	23

**Table 1.6: 290°C Comparison of Mixed Oxides**

	Mg:Al:Ba	20% CO <sub>2</sub> in He Capacity ( $\mu\text{mol}/\text{g}$ )	Mixed CO <sub>2</sub> Capacity ( $\mu\text{mol}/\text{g}$ )	Total NO Capacity ( $\mu\text{mol}/\text{g}$ )	NO Tdes (High)	NO:O <sub>2</sub> Ratio
<b>MgO</b>	1:0:0	103	16	202	475	1.59
<b>MgO/ Al<sub>2</sub>O<sub>3</sub></b>	1:4:0	68	0	84	425	1.61
<b>HT</b>	7:3:0	-	0	89	500	1.50
<b>BaO/ Al<sub>2</sub>O<sub>3</sub></b>	0:2:1	211	182	36	525	1.13

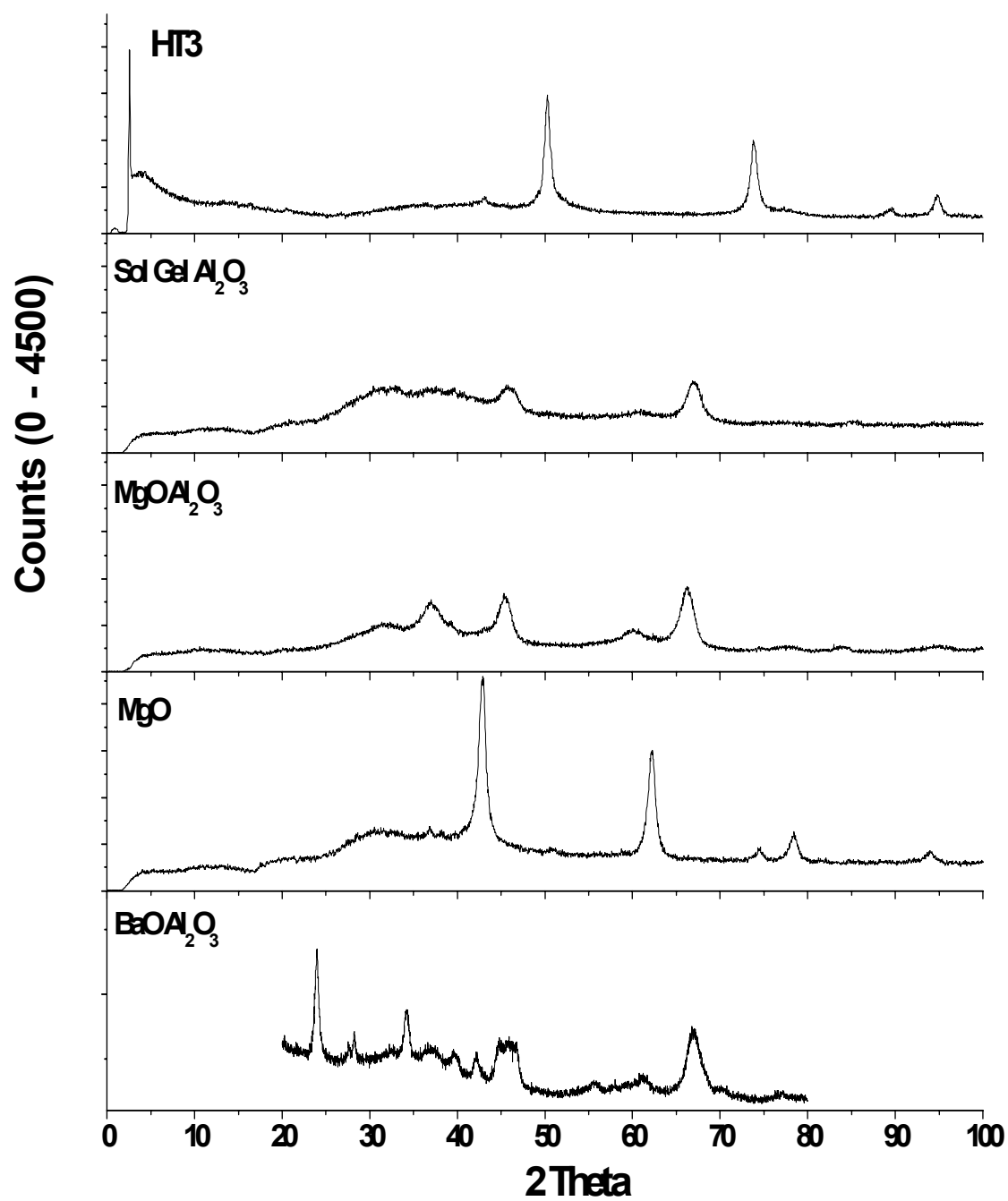
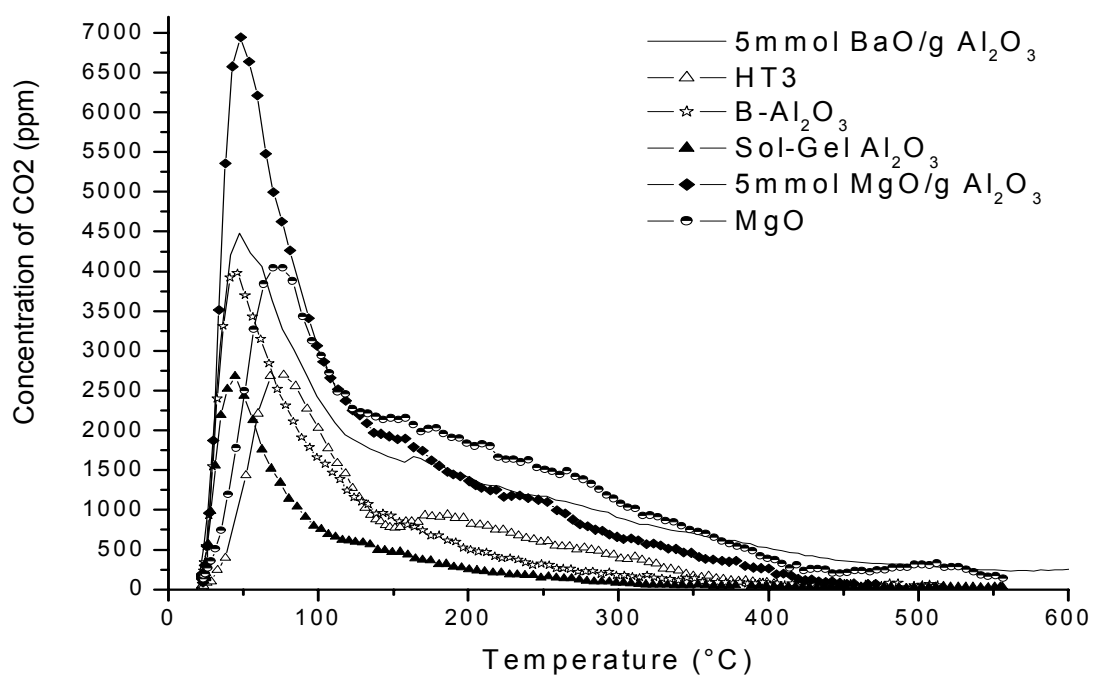
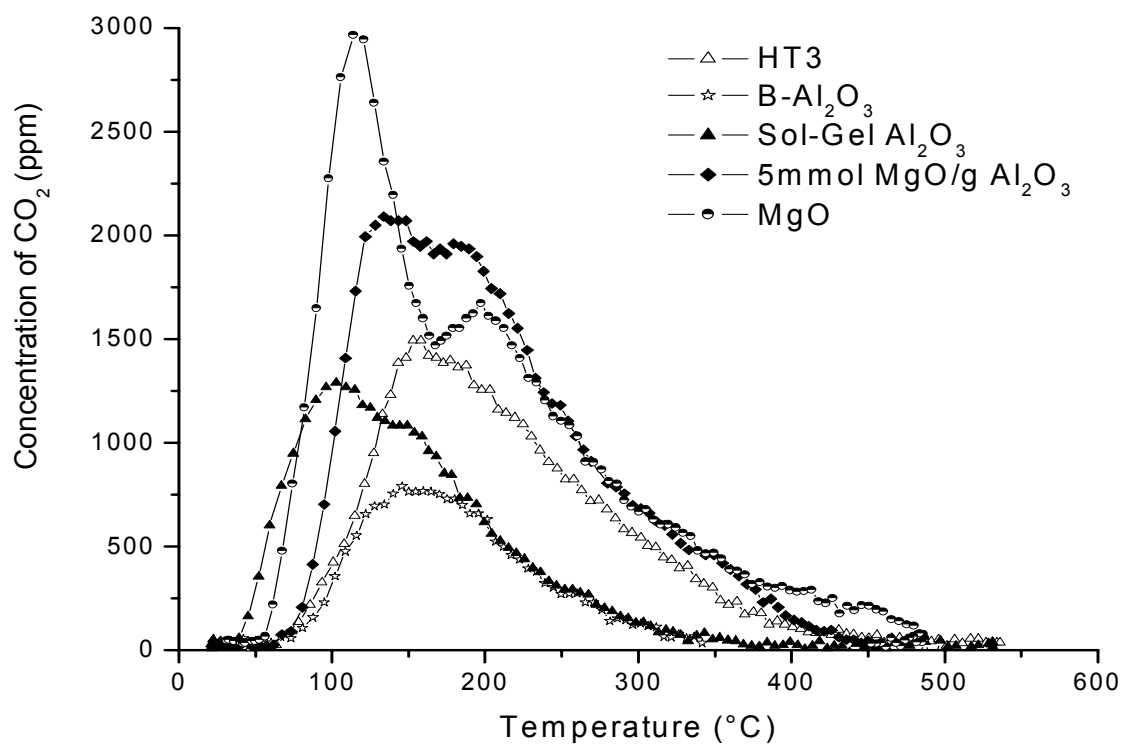


Figure 1.1: Diffraction Patterns of HT3, sol-gel  $\text{Al}_2\text{O}_3$ , boehmite  $\text{Al}_2\text{O}_3$ ,  $\text{MgO}/\text{Al}_2\text{O}_3$ ,  $\text{MgO}$ , and  $\text{BaO}/\text{Al}_2\text{O}_3$



**Figure 1.2: CO<sub>2</sub> TPD after Adsorption at 30°C**



**Figure 1.3: CO<sub>2</sub> TPD after Adsorption at 100°C**

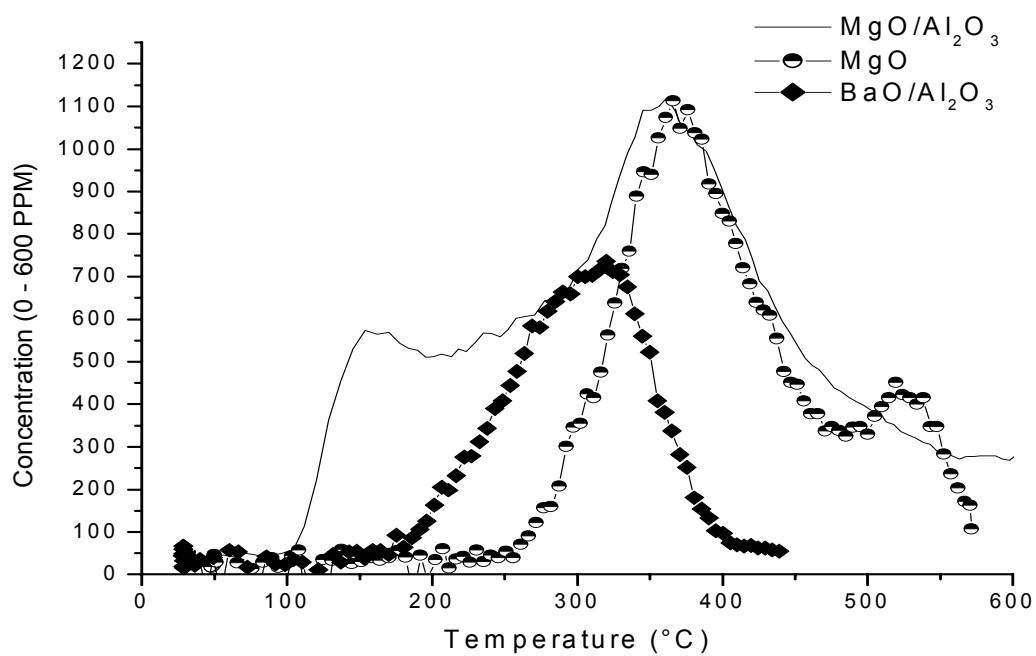


Figure 1.4: CO<sub>2</sub> TPD after Adsorption at 290°C

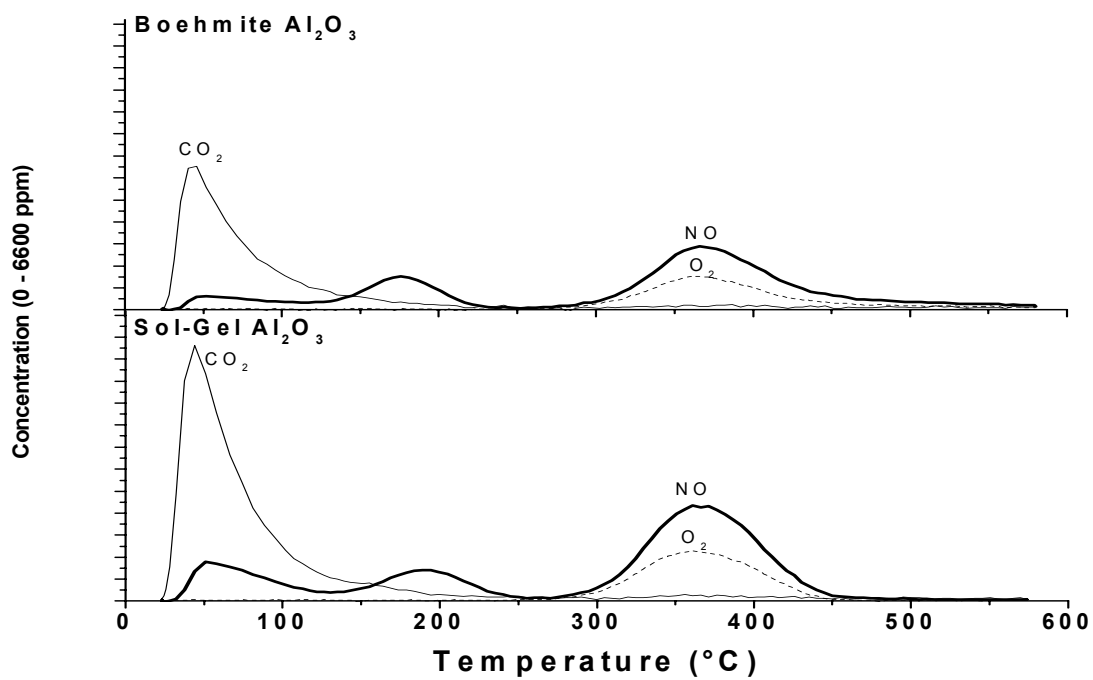


Figure 1.5: 30°C Adsorption of NO<sub>2</sub> Mix Gas and CO<sub>2</sub> on Alumina

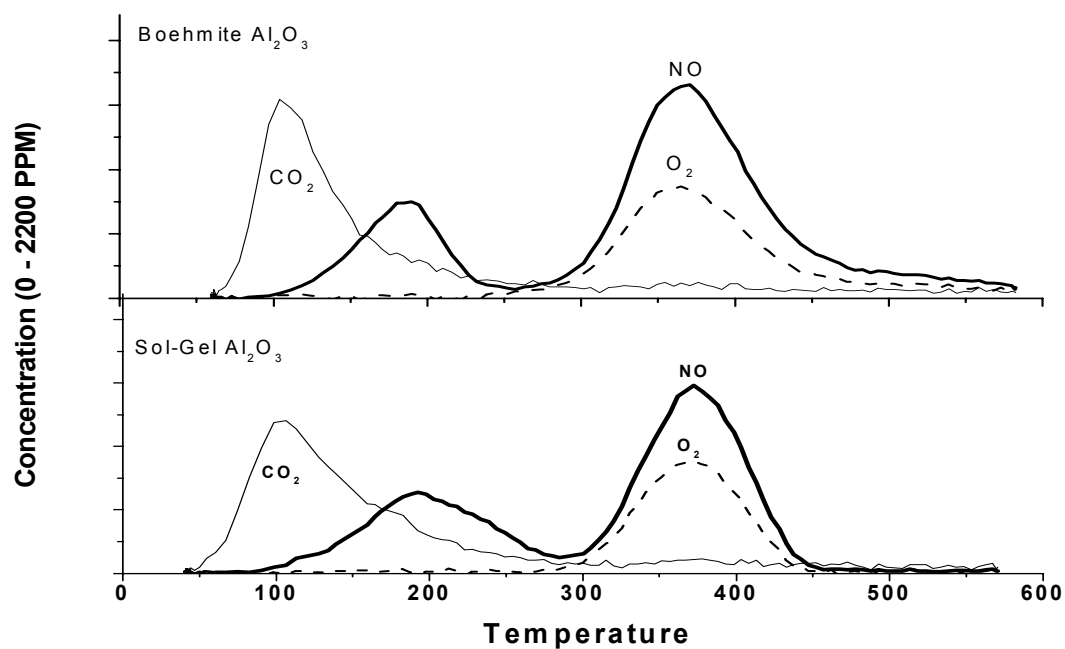


Figure 1.6: 100°C Adsorption of  $\text{NO}_2$  Mix Gas and  $\text{CO}_2$  on Alumina

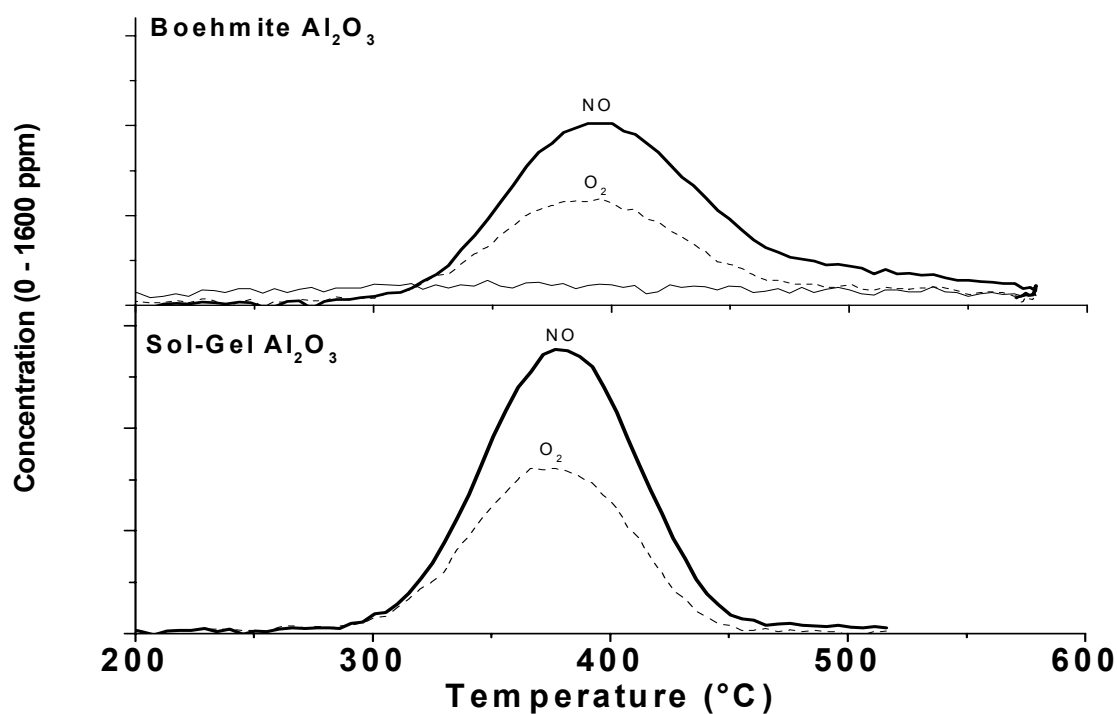
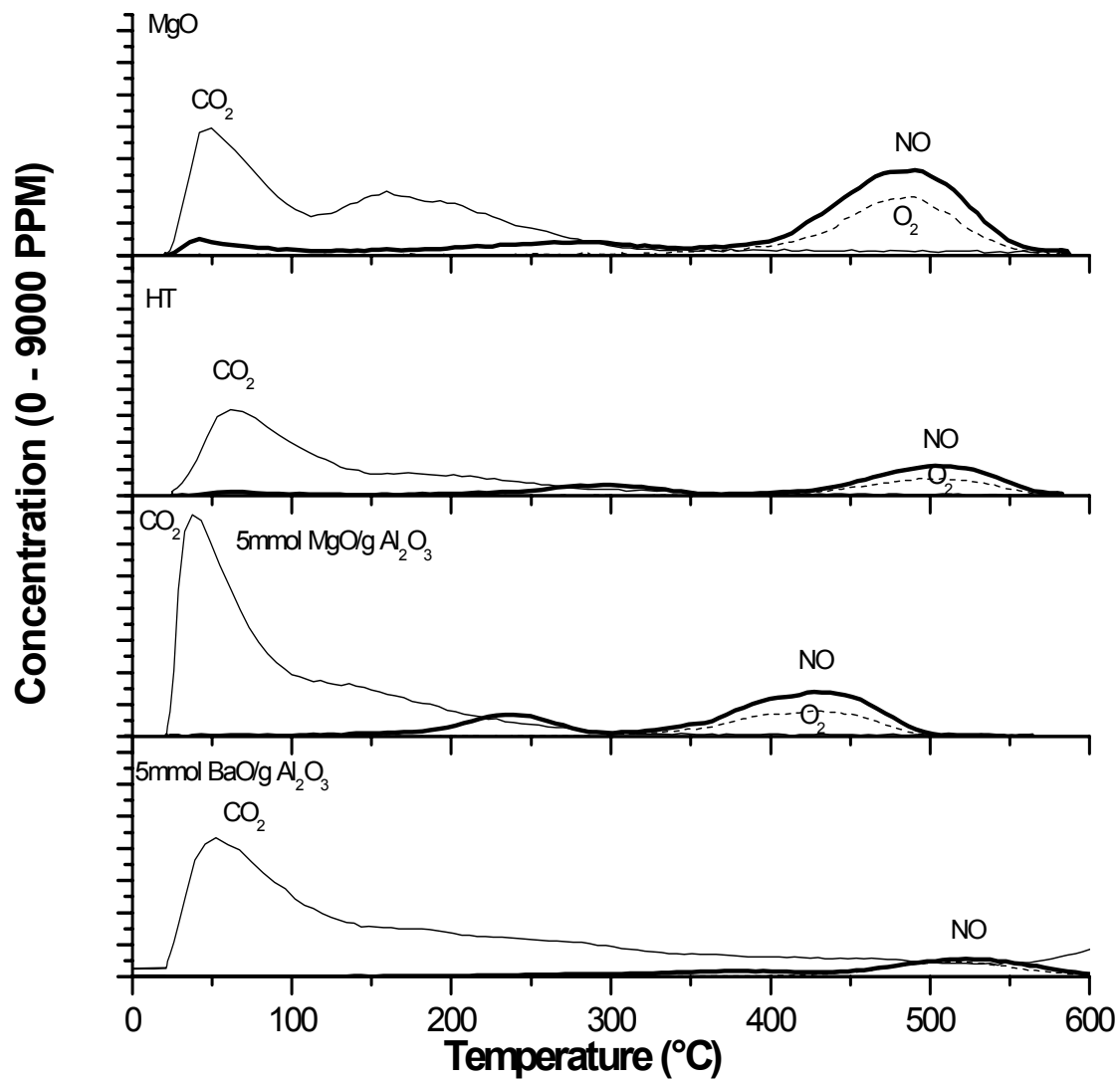


Figure 1.7: 290°C Adsorption of  $\text{NO}_2$  Mix Gas and  $\text{CO}_2$  on Alumina





**Figure 1.8: MgO, Commercial Hydrotalcite, and MgO/Al<sub>2</sub>O<sub>3</sub> CO<sub>2</sub> and NO<sub>2</sub> Adsorption at 30°C**

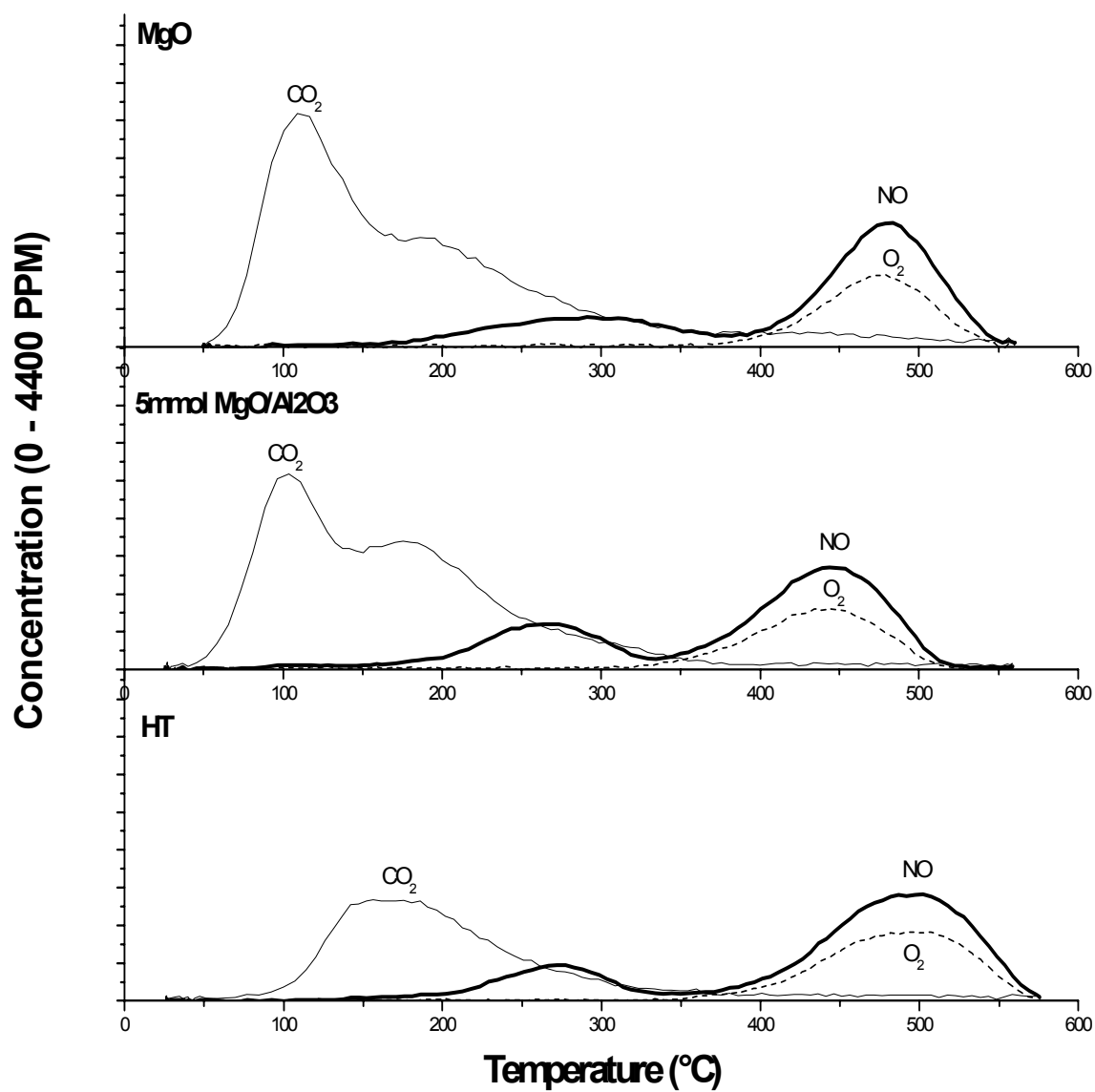


Figure 1.9: MgO, Commercial Hydrotalcite, and MgO/Al<sub>2</sub>O<sub>3</sub>  
CO<sub>2</sub> and NO<sub>2</sub> Adsorption at 100°C

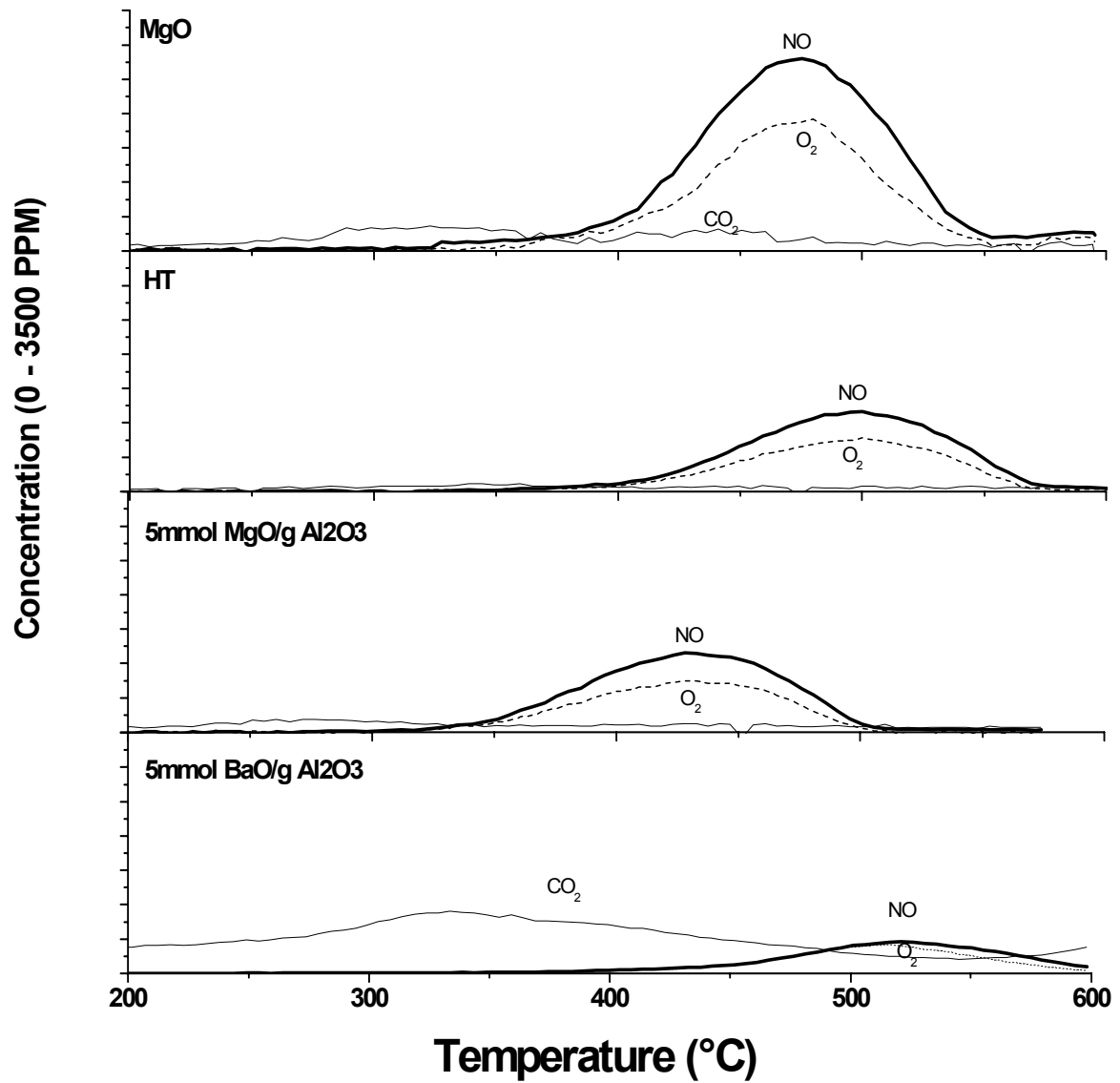
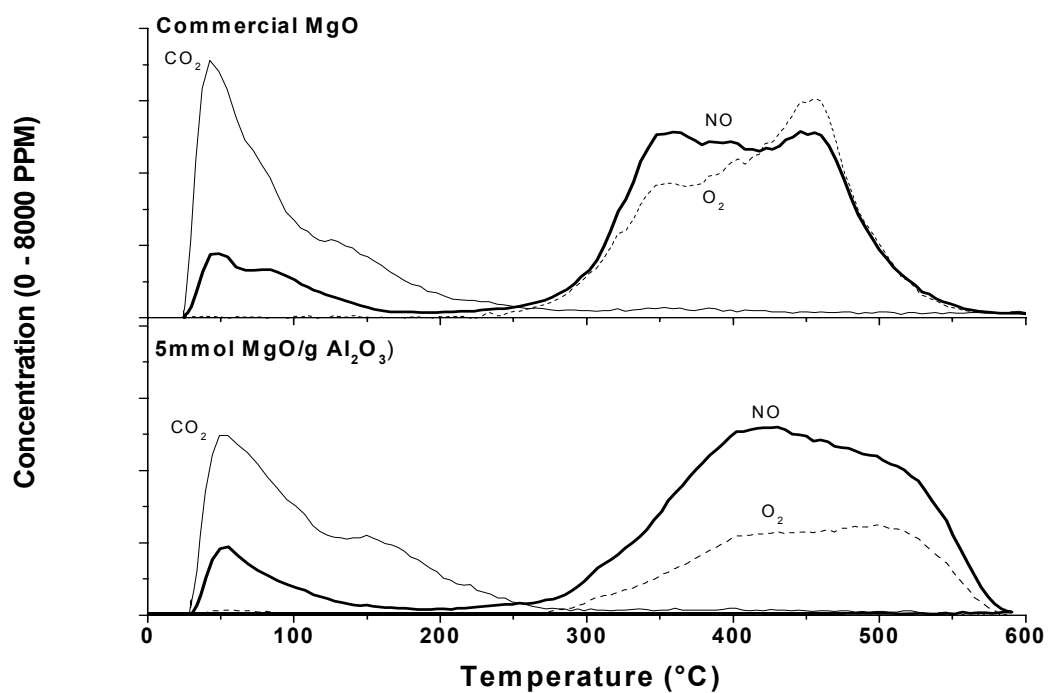


Figure 1.10: MgO, Commercial Hydrotalcite, and MgO/Al<sub>2</sub>O<sub>3</sub>  
CO<sub>2</sub> and NO<sub>2</sub> Adsorption at 290°C



**Figure 1.11: MgO, Commercial Hydrotalcite, and MgO/Al<sub>2</sub>O<sub>3</sub> CO<sub>2</sub> and NO<sub>2</sub> Adsorption at 290°C and cooled in the NO<sub>2</sub> mixed gas**

## **Chapter II: Characterization of (Mg,Al) Oxides as NO<sub>x</sub> Storage Materials: Infrared Spectroscopy of Adsorbed Species**

Bryan A. Silletti,<sup>1</sup> Susan Sigmon James J. Spivey,<sup>2</sup> and H. Henry Lamb\*

Department of Chemical Engineering,  
North Carolina State University  
Raleigh, NC 27695 USA

\*Author to whom correspondence should be addressed.

Phone: (919)-515-6395  
Fax: (919)-515-3465  
e-mail: lamb@eos.ncsu.edu

<sup>1</sup>Present Address: Caterpillar Inc., Mossville, Illinois

<sup>2</sup>Present Address: Department of Chemical Engineering, Louisiana State University, Baton Rouge, LA

## ABSTRACT

In this study, we investigated a mixed gas adsorption of 20% CO<sub>2</sub>, 12% O<sub>2</sub>, 1000 ppm NO<sub>2</sub> in balance He on basic storage oxides suitable for NO<sub>x</sub>SR catalysts utilizing Diffuse Reflectance Infrared Fourier Transform Spectroscopy (DRIFTS). The oxides used were MgO, Hydrotalcite, MgO/Al<sub>2</sub>O<sub>3</sub> and BaO/Al<sub>2</sub>O<sub>3</sub>. On all oxides, a surface bicarbonate and physisorbed CO<sub>2</sub> were removed after heating to 100°C in He. The low temperature NO desorption peaks are indicative of nitro species on Al<sub>2</sub>O<sub>3</sub> and MgO, but were either not clearly defined or not present on the HT and BaO/Al<sub>2</sub>O<sub>3</sub>. These surface nitro species are both converted to nitrate species and desorbed as the catalyst surface is heated in He. It was shown that BaO/Al<sub>2</sub>O<sub>3</sub> had the largest interaction with the CO<sub>2</sub> in the mixed gas and formed the largest concentration of bicarbonates that were stable until 200°C. In addition, very thermally stable monodentate and bidentate carbonate were formed and not desorbed from the surface at 500°C. On all of the oxides, various nitrate surface species were formed, but primarily monodentate nitrate. Consistent with the TPD results, the thermal stability of the nitrate on the various oxides is given as BaO/Al<sub>2</sub>O<sub>3</sub> > HT > MgO > Al<sub>2</sub>O<sub>3</sub>.

## Introduction

The NO<sub>x</sub> storage-reduction (NO<sub>x</sub>SR) catalyst is a new catalytic technology designed to reduce noxious emissions for lean burn engines. Through the storage of NO<sub>x</sub> in lean exhaust conditions followed by a short rich pulse to reduce the stored NO<sub>x</sub> to N<sub>2</sub>, the NSR catalyst is able to reach 90% NO<sub>x</sub> conversion. These catalysts have been studied extensively to understand their applicability in automobile applications, particularly the Toyota developed catalytic system, Pt/Rh/BaO/Al<sub>2</sub>O<sub>3</sub>. Barium oxide is typically used as the storage component in NO<sub>x</sub>SR catalysts due to its basic nature and the large polarizability of Ba ions, but other alkali and alkaline earth metals have also been investigated. A variety of techniques have been used to evaluate the chemistry of these catalytic systems, particularly temperature programmed desorption (TPD) and infrared spectroscopy. TPD is a very useful technique to isolate the relative thermal stabilities and (desorption) activation energies of adsorbates on surfaces of mixed oxides, but yet it does not give an indication of the specific nature of the binding of the adsorbate to the catalyst surface. Using diffuse reflectance infrared Fourier transform (DRIFTS) spectroscopy, the NO<sub>x</sub>SR adsorption process can be characterized through measurement of the infrared-active vibrational modes of the adsorbates during the lean condition[41]. Utilizing DRIFTS, we have characterized the nature of the adsorbed species on various Mg, Al mixed oxides as well as BaO/Al<sub>2</sub>O<sub>3</sub> after exposure to a simulated exhaust gas containing 20% CO<sub>2</sub>, 12% O<sub>2</sub>, 1000 ppm NO<sub>2</sub> in He (balance). The goal of this research was to understand how the various adsorbates compete for surface sites during the storage process. In addition, we examined the thermal stability of adsorbed species in an inert atmosphere.

## Experimental Methods

### *Materials*

MgO (Magchem AD200, Martin Marietta) and a commercial hydrotalcite (HT), with a Mg:Al ratio of 7:3 were calcined separately in flowing O<sub>2</sub> at 150 mL/min with a 4°C/min ramp rate from 30°C to 600°C and soaked for 2 hours. A sol-gel Al<sub>2</sub>O<sub>3</sub> was synthesized using aluminum isopropoxide and 2-methyl-2,4-pentanediol; the resulting powder was calcined at 700°C for 2 h. Subsequently, the calcined Al<sub>2</sub>O<sub>3</sub> was doped with Ba using Ba(NO<sub>3</sub>)<sub>2</sub> as the precursor via incipient wetness.

### *Diffuse Reflectance Infrared Fourier Transform Spectroscopy (DRIFTS)*

An Analect RFX-65 FTIR spectrometer equipped with a Harrick Scientific Praying Mantis DRIFTS cell and an MCT detector was employed in these experiments. Spectra were recorded at 8 cm<sup>-1</sup> resolution using 1024 interferometer scans for the background and 512 scans for the sample. Each spectrum was recorded using dehydrated KBr powder in He as the background. Ultrahigh purity He and a certified gas mixture containing 1000 ppm NO<sub>2</sub>, 20% CO<sub>2</sub>, 12% O<sub>2</sub> in balance He were metered using a calibrated rotometer. Approximately 50 mg of each sample was placed in the sample cup inside a high-temperature dome with KBr windows. The sample was then heated at 10°C/min to 500°C in flowing He (16 mL/min NTP) and soaked for 1 h. The sample was allowed to cool to 30°C in flowing He, and the DRIFTS spectrum was recorded. Subsequently, the sample was treated in flowing the NO<sub>2</sub> mixed gas (13 mL/min) at 30°C for 30 min and then purged in He (16 mL/min) for 30 min. Spectra were recorded at 1, 5, and 30 min of adsorption of the mixed gas as well as 1, 5, and 30 min after purging in He, but only the spectrum after 30-min purging was included in the analysis. After the adsorption and



purge, the sample was heated by soaking in He for 30 minutes at 100°C, 200°C, 300°C, 400°C, and 500°C.

## Results

Table 2.1 provides a summary of IR active bands in the gas phase as well as the expected adsorbed species on the metal oxide surfaces for CO<sub>2</sub>, NO<sub>2</sub>, and H<sub>2</sub>O. The structures of the various surface carbonates, nitrates, and nitrites can be seen in Figure 2.1. The normal modes of vibration for CO<sub>2</sub> that are given in Table 1 are the following: the symmetric stretch at 1340 cm<sup>-1</sup>, asymmetric stretch at 2350 cm<sup>-1</sup> and a bending mode at 667 cm<sup>-1</sup> [42]. The respective carbonate (CO<sub>3</sub><sup>2-</sup>) formed from interacting with the surface will exhibit strong IR absorptions in the asymmetric stretch in the region from 1530 – 1320 cm<sup>-1</sup>, but typically restricted to 1450 – 1400 cm<sup>-1</sup> along with medium strength bands in the out of plane bending mode at 890 – 800 cm<sup>-1</sup> [43]. In addition, surface bicarbonates can be formed by interaction of the CO<sub>2</sub> molecule with isolated OH groups. Bicarbonates have reduced symmetry and, as a result, have a larger number of IR active normal modes than carbonates, yielding strong IR bands at 1700 – 1600 cm<sup>-1</sup>, near 1400 cm<sup>-1</sup> (very strong), 1000 – 950 cm<sup>-1</sup> (medium, multiple bands) and 850 – 800 cm<sup>-1</sup> [43]. H<sub>2</sub>O has a symmetric stretch at 3657 cm<sup>-1</sup>, an asymmetric stretch at 3756 cm<sup>-1</sup> and a bending mode at 1595 cm<sup>-1</sup> [43]. The free nitrate ion will yield an absorption band in the region from 1500 – 1300 cm<sup>-1</sup> for the symmetric stretch and the bending vibrations gives peaks at 850 – 800 cm<sup>-1</sup> and 770 – 715 cm<sup>-1</sup> [43]. When an ionic metal nitrate is formed, this mode will split to form two strong bands between 1550 – 1250 and activate the symmetric stretch at 1070 – 1010 cm<sup>-1</sup> [43]. Nitrites exhibit two stretching vibrations in the region from 1365 – 1320 and 1270 – 1210, but these absorptions can often overlap on surfaces [43].

Figure 2.1A documents the diffuse-reflectance (DR) infrared spectrum of the sol-gel  $\text{Al}_2\text{O}_3$  in the high frequency ( $3800 - 2800 \text{ cm}^{-1}$ ) and low frequency regions ( $1800 - 800 \text{ cm}^{-1}$ ) measured at  $30^\circ\text{C}$  after heating to  $500^\circ\text{C}$  for 1 h. The OH stretching vibrations of isolated surface hydroxyl groups appear at  $3746$ ,  $3708$ , and  $3646 \text{ cm}^{-1}$  with an associated Al-O stretch at  $950 \text{ cm}^{-1}$ . In general, the highest frequency peaks are associated with the most basic isolated OH groups [44]. A broad band at  $3565 \text{ cm}^{-1}$  is indicative of H-bonded OH groups. In the low frequency region, there are possibly some bidentate nitrate and monodentate carbonate species ( $1420$ ,  $1370 \text{ cm}^{-1}$ ) still present on the oxide surface. Figure 2.2A shows the DR spectrum of the sol-gel  $\text{Al}_2\text{O}_3$  after adsorption of the  $\text{NO}_2$  mixed gas at  $30^\circ\text{C}$  and purging with He. The absorbance difference spectrum was obtained by subtracting the spectrum of the sample after heating from the sample after adsorption and purge. After adsorption, the OH peaks at  $3750$  and  $3715 \text{ cm}^{-1}$  were removed with an associated increase in  $3630$  to  $3000 \text{ cm}^{-1}$ , bands associated with  $\text{H}_2\text{O}$  adsorption. In addition, a new peak emerged at  $3688 \text{ cm}^{-1}$ , and a broad band at  $1616 \text{ cm}^{-1}$  emerges that has several shoulders at  $1632$ ,  $1593$ ,  $1563$ , and  $1540 \text{ cm}^{-1}$ . There is a great deal of overlap of the infrared bands of surface carbonates, nitrates, and adsorbed water in the low frequency region. Using Table 2.1, we assign the peaks at  $1540$ ,  $1247$ ,  $974 \text{ cm}^{-1}$  to monodentate nitrate species. In addition, charged nitro species, bound to the metal cation via the nitrogen, are formed with bands at  $1443$ ,  $1313 \text{ cm}^{-1}$ . but the bands at  $1420$ ,  $1370$ , and  $1050 \text{ cm}^{-1}$  may be assigned to monodentate carbonate species. It is well known that  $\text{CO}_2$  adsorbs on  $\text{Al}_2\text{O}_3$  at low temperature to form bicarbonate species bound to the type I and II hydroxyl groups yielding IR bands at  $1650$ ,  $1486$ , and  $1236$ ; however, there does not seem to be evidence for the desorption of a bicarbonate species (see below).

Figure 2.3 and Table 2.2 show the results as the sample was heated in He to desorb surface species. The broad adsorbed H<sub>2</sub>O band was reduced with the largest changes occurring at 3573 and 3446 cm<sup>-1</sup>. Concurrently, infrared bands associated with isolated OH groups began to re-emerge with peaks at 3750 and 3708 cm<sup>-1</sup>. Water desorption is also indicated by the loss of peaks at 1636 and 1663 cm<sup>-1</sup> as the temperature increases. These IR bands overlap with the bicarbonate and whatever bicarbonate is present on the surface is being desorbed with H<sub>2</sub>O. A monodentate carbonate species (1420, 1370, 1050 cm<sup>-1</sup>) seems to be stable until 400°C and then desorbs by 450°C, but this is inconsistent with the TPD results. At 100°C there is very little reduction in the adsorbed NO<sub>x</sub> species. At 200°C, the nitro (1443, 1313 cm<sup>-1</sup>) species begins to convert to monodentate nitrate (1540, 1247, and 971 cm<sup>-1</sup>), bidentate nitrate (1566, 1290, 1050 cm<sup>-1</sup>) and bridging nitrite (1205 cm<sup>-1</sup>) species. This process continues to a maximum at 400°C, where this species IR bands are lost at 450°C.

The DR infrared spectrum of the MgO sample after heating, Figure 2.1B, evidences isolated surface OH groups at 3747, 3727, 3669, and 959 cm<sup>-1</sup>. In addition there is a broad peak at 3492 cm<sup>-1</sup> indicating H-bonded OH species. Also, there still seems to be some monodentate carbonate (1432, 1305, 1040 cm<sup>-1</sup>) species as well as minor amounts of bidentate nitrate (1543 and 1286 cm<sup>-1</sup>) as indicated by Table 2.1. After adsorption, Figure 2.2B, there is a large negative peak at 3742 cm<sup>-1</sup> indicating that there are few if any (unperturbed) isolated OH groups and a broad band due to adsorbed water increases significantly, particularly at 3577 and 3442 cm<sup>-1</sup>. Although H<sub>2</sub>O is removed during heating, in Figure 2.4 and Table 2.3, given by the reduced absorbance in the region from 3650 – 2900 cm<sup>-1</sup>, the isolated OH group at 3738 cm<sup>-1</sup> decreases in total absorbance. In the low-frequency region, bridging nitrate (1586, 1232, 1017 cm<sup>-1</sup>), bidentate nitrate (1543, 1286 cm<sup>-1</sup>), and nitro (1405, 1320 cm<sup>-1</sup>) all appear. In addition,

bicarbonate species (1636, 1420, and 1213  $\text{cm}^{-1}$ ) and monodentate carbonate species (1447, 1347, and 1055  $\text{cm}^{-1}$ ) emerge. The surface bicarbonate and monodentate carbonate species desorb primarily at 100°C and 200°C, respectively. During heating in He, the bidentate nitrate increases at temperatures up to and including 350°C consistent with the conversion of surface nitro species, but then is removed at 400°C and 450°C. The bridging nitrate species is stable until 350°C, where the bands associated with this species actually increase at 400°C and 450°C as depicted by peaks (1580, 1232, 1017  $\text{cm}^{-1}$ ). This increase in absorbance could be associated with the conversion of bidentate nitrate to bridging nitrate species.

The DR infrared spectrum of the BaO/Al<sub>2</sub>O<sub>3</sub> sample after heating (Figure 2.1C) is indicative of isolated surface OH groups after heating at 3750, 3715, 3673, 3661, and 3638,  $\text{cm}^{-1}$ . In addition there is a broad peak at 3577  $\text{cm}^{-1}$  indicating H-bonded OH. There are carbonate species still present on the surface of the BaO/Al<sub>2</sub>O<sub>3</sub> as evidenced by the C=O stretch at 1747  $\text{cm}^{-1}$  and monodentate carbonate (1470, 1374, 1060) [39]. After adsorption, Figure 2.2C, there are two large negative peaks at 3750, 3715  $\text{cm}^{-1}$  indicating that there are few if any (unperturbed) isolated OH groups due to the adsorption of H<sub>2</sub>O. In addition, peaks at 3610, 1610 and 1224  $\text{cm}^{-1}$  emerge. This indicates that a significant amount of surface bicarbonate (HOCO<sub>2</sub><sup>-</sup>) is adsorbed on the surface to type I and II OH- groups present at 3750 and 3673  $\text{cm}^{-1}$ , respectively. The peak exposed after heating at 1743  $\text{cm}^{-1}$  was suppressed after adsorption. Bands associated with monodentate carbonate (1470, 1374  $\text{cm}^{-1}$ ) and bidentate carbonate (1570, 1251  $\text{cm}^{-1}$ ) species increased after adsorption. Monodentate nitrate (1520, 1270, 971  $\text{cm}^{-1}$ ) increased after adsorption, while bidentate nitrate (1532, 1290  $\text{cm}^{-1}$ ) emerged as a new species. Using the peak positions and their change with increasing temperature documented in Table 2.4 and Figure 2.5, it can be seen that a significant amount of the bicarbonate species desorbed at

100°C and continued through 200°C. The bands associated with monodentate carbonate species increased through 500°C. Bands due to bidentate carbonate increase at 200°C, but then decrease through 500°C, with some residual species still present at 500°C. Bands assigned to bidentate nitrate (1532, 1294  $\text{cm}^{-1}$ ) continue to grow in through 300°C, but then decreases through 500°C (again with some residual presence at 500°C). Monodentate nitrate seems to change very little during the temperature increase until 400°C, where the peaks at 1270 and 1520  $\text{cm}^{-1}$  increase. There do not seem to be nitrite and nitro species on the surface, but potentially the bidentate nitrate is converting to the monodentate nitrate as the temperature increases.

As seen in Figure 2.1D, the hydrotalcite sample had no isolated hydroxyl groups after heating and yields only broad peaks in the low frequency region after heating. In the high frequency region, the only discernible peak identification could be a bidentate carbonate after heating at (1586, 1317, 1040  $\text{cm}^{-1}$ ) as well as potentially Mg-OH bonds at 948  $\text{cm}^{-1}$ . After adsorption, Figure 2.2D, a significant water adsorption peak at 1659  $\text{cm}^{-1}$  appeared, as well as monodentate nitrate (1490, 1251, 978  $\text{cm}^{-1}$ ) and bidentate nitrate (1580, 1290  $\text{cm}^{-1}$ ). During the desorption, given by Figure 2.6 and Table 2.5, other than the obvious removal of water, the only other discernible feature was potentially the increase of monodentate nitrate (1490, 1251, 978  $\text{cm}^{-1}$ ), but the broadness of the peaks makes it difficult to isolate. Lastly, bands due to the bidentate nitrate increased through 400°C and the shoulder decreased significantly at 500°C. After desorbing at 500°C, there was some evidence of some isolated OH groups at 3708  $\text{cm}^{-1}$  and 3685  $\text{cm}^{-1}$  indicating either further dehydration of the sample or desorption of bound surface species previously bound to the OH groups.

## Discussion

With the exception of HT, each metal oxide after soaking at 500°C in He exposes isolated hydroxyl peaks that are associated with the stretching mode of the OH bound to the surface. CO<sub>2</sub> can bind at OH terminated surfaces whereby the isolated OH acts as a basic site active for CO<sub>2</sub> adsorption through the donation of electrons to the electropositive carbon. The bicarbonate IR bands were most significant on the BaO, the most basic oxide, but were also present on the MgO. The OH groups on BaO/Al<sub>2</sub>O<sub>3</sub> are the strongest basic sites as the oxygen anion has the largest negative charge and is able to donate its electrons more effectively. The bicarbonate, however, is mostly desorbed from the surface of the BaO after 100°C and was completely removed by 200°C. The isolated hydroxyl groups on sol-gel Al<sub>2</sub>O<sub>3</sub> reappear during the desorption stage of the experiment. On MgO these groups do not re-emerge at all, while on BaO/Al<sub>2</sub>O<sub>3</sub> the isolated OH bands do reappear at 100°C during desorption, but then are removed after further heating above 100°C. The hydroxyl band absorbance continues to decrease after heating, indicating that the surface is being dehydroxylated.

In general, the trends of the various nitrates and carbonates are consistent with the TPD results of the same materials (Chapter I). On Al<sub>2</sub>O<sub>3</sub>, the average nitrate thermal stability is approximately 400°C with no nitrates are still stable at 450°C. It is interesting to note is that the low temperature adsorbed nitro species are associated with the very symmetrical TPD feature that desorbs between 100°C and 290°C and has been seen on Pt/Al<sub>2</sub>O<sub>3</sub> by Uy et al [45]. Inconsistent with the TPD results, is the thermal stability of the monodentate carbonate that is stable through 400°C, whereas the TPD results indicate that there is no further CO<sub>2</sub> adsorption after 290°C. It is possible that, in the presence of H<sub>2</sub>O, the bicarbonate may be destabilized via H-OH groups minimizing the interaction of the CO<sub>2</sub> molecule with the basic OH groups.

However, the more thermally stable carbonate may still be created. On MgO, the bicarbonate decreased significantly by 100°C, consistent with the change in CO<sub>2</sub> capacity seen from the TPD results. The more thermally stable CO<sub>2</sub> from the TPD results in chapter I are associated with the monodentate carbonate bound to the more basic MgO sites on the surface. Similar to the Al<sub>2</sub>O<sub>3</sub>, the low temperature NO<sub>x</sub> desorption is associated with the nitro species, but they are not as clearly shown on the Al<sub>2</sub>O<sub>3</sub>. The nitro species, during heating convert to bidentate nitrate through 350°C, but are removed and converted to the more thermally stable bridging nitrate species on the MgO. This is consistent with the TPD results as the peak desorption temperature was approximately 475°C on the MgO.

BaO/Al<sub>2</sub>O<sub>3</sub> forms a large concentration of bicarbonates in the presence of NO<sub>2</sub> and H<sub>2</sub>O, that are not as readily formed for Al<sub>2</sub>O<sub>3</sub> and MgO. Due to the thermal stability of BaCO<sub>3</sub> and BaNO<sub>3</sub>, there is still some bulk carbonate and nitrate (primarily carbonate) present on the surface, and this provides an possible indication of the exchange that occurs between the carbonate and nitrate phases indicated by [39]. The carbonate phase that is clearly present after heating is covered after adsorption of the NO<sub>2</sub> mixed gas at room temperature, but reappears after the sample is treated to 500°C. This indicates that the carbonate is the most thermally stable phase after treatment at 500°C, but during the adsorption process where H<sub>2</sub>O, CO<sub>2</sub> and NO<sub>2</sub> are present, even at low concentrations, NO<sub>2</sub> is more preferentially adsorbed at the more basic oxygen sites that yield primarily surface nitrates. As the temperature is increased, the H<sub>2</sub>O, and bicarbonates are quickly removed, while both the monodentate nitrate and carbonate species actually increase through 500°C. The bidentate nitrate and carbonate however, begin desorption at 500°C.

Although Lopez et al established clear adsorption phases on hydrotalcite, this sample did not depict significant species on the surface of this catalyst [46]. The assumption is that either the sample was not adequately aligned during the experiment, a clear adsorption phase for this material is not IR active or that other problems occurred that are not known.

## Conclusions

On all of the metal oxides, but primarily on BaO/Al<sub>2</sub>O<sub>3</sub>, surface bicarbonate and physisorbed CO<sub>2</sub> were removed after heating to 100°C in He after adsorption of the NO<sub>2</sub> mixed gas at 30°C. The low temperature NO desorption peaks that were present in the TPD results are indicative of nitro species on Al<sub>2</sub>O<sub>3</sub> and MgO, but are not clearly defined on the HT and BaO/Al<sub>2</sub>O<sub>3</sub>. These surface nitro species are partially converted to different nitrate species on the surface, depending on the particular oxide. On all the mixed oxides, the nitrate is formed after adsorption at 30°C. Consistent with the TPD results and predictions by the electronegativity of the metal, the thermal stability of the nitrate on the various oxides is given as BaO/Al<sub>2</sub>O<sub>3</sub> > HT > MgO > Al<sub>2</sub>O<sub>3</sub>.



**Table 2.1: Frequencies of Stretching and Bending Vibrations for All Species**

Gas Phase Species	> 2000	2000 - 1700	1700 - 1400	1400 - 1100	< 1100
NO <sub>2(g)</sub>			1618		
NO(g)	2200, 2150	1874	1700, 1650	1300	
N <sub>2</sub> O(g)	2224			1284	
N <sub>2</sub> O <sub>4(g)</sub>		1742			
H <sub>2</sub> O(g)	3756	3657		1595	
CO <sub>2(g)</sub>	3740, 3700	3630, 3590	2350		667
<b>Surface CO<sub>3</sub><sup>2-</sup> Species</b>					
CO <sub>3</sub> <sup>2-</sup>			1450-1400		890-800
Bicarbonates		1700 – 1600	1490 - 1400	1250 - 1210	1010 – 950
Non-Coord. Carbonate			1470 - 1430		1090 - 1020
“Organic”		1870 - 1750		1250 -1150	1080 –1050
Monodentate Carbonate			1470 - 1430	1375 - 1300	1080 – 1050
Bidentate Carbonate		1670 – 1530		1350 – 1250	1090 - 1040
C=O Stretch		1740			
<b>Surface NO<sub>2</sub><sup>-</sup>/NO<sub>3</sub><sup>-</sup></b>					
Free NO <sub>3</sub> <sup>-</sup> Ion			1380	1050	
Monodentate Nitrate		1530-1480	1290 - 1250	1035 - 970	
Bidentate Nitrate		1565-1500	1300 - 1260	1040 -1010	
Bridging Nitrate		1650-1600	1225 - 1170	1030 - 1000	
Free NO <sub>2</sub> <sup>-</sup> Ion			1330	1260	
Bridging Nitrite				1220-1205	
Monodentate Nitrite			1470-1450	1260-1180	
Nitro			1440-1335	1350-1315	
<b>CO<sub>2</sub> on Al<sub>2</sub>O<sub>3</sub></b>					
Bicarbonate (HC1)	3609	1649	1482	1232	
Bicarbonate (HC2)	3620	1649	1458	1232	
Al <sub>2</sub> (CO <sub>3</sub> ) <sub>3</sub> (SC-Al <sup>3+</sup> )			1458		
Bidentate Al <sup>3+</sup> (B-Al)		1650		1230	
Monodentate (M-Al)		1528	1400		
<b>CO<sub>2</sub> on MgO</b>					
Monodentate Carbonate		1526		1419	1075
Bicarbonate		1658		1223	
<b>CO<sub>2</sub> on BaO</b>					
Bidentate Carbonate		1575		1295	
Mono. Carbonate			1440	1320	

**Table 2.2: DRIFTS Characterization of the Adsorption and Desorption  
of NO<sub>2</sub> Mixed Gas on Al<sub>2</sub>O<sub>3</sub>**

After Heating		3708	3646	3558			1609		1578		
After Ads	3746 \	3715 \	3665 \	3581 /	3448 /		1613	1593 /	1563 /	1540 /	1486 /
100C	3750 /	3708 /		3573 \	3446 \	1663	1636		1566	1540 /	1486 \
200C	3750 /	3708 /		3573 \	3446 \	1663 \	1636 \		1566 /	1540 /	1486 \
250C	3750 /	3708 /		3573 \	3446 \	1659 \	1636 \		1566 /	1540 /	1486 \
300C	3750 /	3708 /		3573 \	3446 \	1647 \	1636 \		1566 /	1540 /	1486 \
350C	3750 /	3708 /		3573 \	3446 \	1647 \	1636 \		1566 /	1540 /	1486 \
400C	3750 /	3708 /		3573 \	3446 \		1639 \		1566 /	1540 /	1486 \
450C	3750 /	3708 /		3573 \	3446 \		1636 \		1566 \	1540 \	1486 \
	OH-	OH -	OH -	CO <sub>2</sub>	H <sub>2</sub> O	H <sub>2</sub> O/Bic	H <sub>2</sub> O/Bic		Biden Nitrate	Mono Nitrate	Bicarb

After Heating		1420				1290					960
After Ads	1447 /	1413				1297 /	1259 /		1050 /	974 /	963 /
100C	1443 \	1420 -	1370	1355	1313	1290	1247 -	1205	1050 /	974 /	951 -
200C	1443 \	1420 -	1370 \	1355 \	1313 \	1290 /	1247 /	1205 -	1050 /	974 /	951 /
250C	1443 \	1420 -	1370 \	1355 \	1313 \	1290 /	1247 /	1205 -	1050 /	974 /	951 /
300C	1443 \	1420 -	1370 \	1355 \	1313 \	1290 /	1247 /	1205 -	1050 /	974 /	951 /
350C	1443 \	1420 /	1370 /	1355 /	1313 \	1290 /	1247 /	1205 /	1050 \	974 /	951 /
400C	1443 \	1420 /	1370 /	1355 /	1313 \	1290 /	1247 /	1205 /	1050 \	974 /	951 /
450C	1443 \	1420 \	1370 \	1355 \	1313 \	1290 \	1247 \	1205 \	1050 \	974 \	951 \
	Nitro	Mono Carb	Mono Carb		Nitro	Biden Nitrate	Mono Nitrate	Bridge Nitrite	Mono Carb	Mono Nitrate	Al-OH

**Table 2.3: DRIFTS Characterization of the Adsorption and Desorption  
of NO<sub>2</sub> Mixed Gas on MgO**

After Heating		3727	3669		3492						1563			1424
After Ads	3747 \	3727 \	3681 /	3558 /		3408 /			1624 /	1589 /	1540 /	1526 /	1459 /	
100C	3747 \						2351 /	2320 /	1636 \	1586 \	1543 /	1526 /	1443 -	1420 \
150C	3747 \						2351 \	2328 \	1636 \	1586 \	1543 /	1526 /	1447 /	1420 \
200C	3747 \						2351 \	2328 \	1636 \	1586 \	1543 /	1526 /	1447 /	1420 \
250C	3747 \						2351 \	2328 \	1636 \	1586 \	1543 /	1526 /	1447 /	1420 \
350C	3747 \						2351 \	2328 \	1636 \	1586 \	1543 /	1526 /	1447 \	1420 \
400C	3747 \						2351 \	2328 \	1636 \	1586 /	1543 \	1526 \	1447 \	1420 \
450C	3747 \						2351 \	2328 \	1636 \	1586 /	1543 \	1526 \	1447 \	1420 \
	OH-	OH-	OH -	H-OH	H-OH	H-OH	CO <sub>2</sub>	CO <sub>2</sub>	H <sub>2</sub> O/Bi carb	Bridge Nitrate	Biden Nitrate	Mono Nitrate	Mono Carb	Bicarb

After Heating					1305							1040		959 /
After Ads				1351 /		1294 /	1270 /		1213 /	1201 /		1017 /		
100C	1405 \			1347 -			1270 /	1224 /	1213 \	1201 /		1017 /	974 -	
150C	1405 \			1347 /			1263 /	1224 /	1213 \	1201 /		1017 /	974 -	
200C	1405 \			1347 /			1263 /	1224 /	1213 \	1201 /		1017 /	974 -	
250C	1405 \			1347 -		1286 /	1259 /	1224 /	1213 \	1201 /		1017 /	974 /	
350C	1405 \			1347 \		1286 /	1259 /	1232 /	1213 -	1201 /		1017 /	974 /	
400C	1405 \	1393 /	1374 /	1347 \	1320 \	1286 \	1259 \	1232 /	1213 -	1201 /	1051 /	1017 /	974 \	
450C	1405 \	1393 /	1374 /	1347 \	1324 \	1286 \	1259 \	1232 /	1213 -	1201 /	1051 \	1017 /	974 \	
	Nitro			Mono Carb	Nitro	Biden Nitrate	Mono Nitrate	Bridge Nitrate	Bicarb		Mono Carb	Bridge Nitrate	Mono Nitrate	Mg-OH

**Table 2.4: DRIFTS Characterization of the Adsorption and Desorption  
of NO<sub>2</sub> Mixed Gas on BaO/Al<sub>2</sub>O<sub>3</sub>**

After Heating		3715	3658			3546	2793	2439	2351	2324		1747			
After Ads	3746 \	3720 \	3661 /	3610 /	3608 /	3558 /	2793 \	2435 \				1747 \		1639	1609
100C	3750 /	3720 /	3658 \	3610 \	3596 \	3561 \	2793 /	2439 /	2335 /	2320 /	2070 /	1747 /	1736 /	1643 \	1610 \
200C	3750 \	3720 \	3658 \	3610 \	3596 \	3561 \	2793 /	2439 /	2335 \	2328 \	1610 \	1747 \	1736 /	1643 \	1610 \
300C	3750 \	3720 \	3658 \	3610 \	3596 \	3561 \	2793 /	2439 /	2335 \	2328 \		1747 \	1736 /	1643 \	1610 \
400C	3750 \	3720 \	3658 \	3610 \	3596 \	3561 \	2793 /	2439 /	2335 \	2328 \	2070 \	1747 \	1736 /	1643 \	1610 \
500C	3750 \	3720 \	3658 \	3610 \	3596 \	3561 \	2793 /	2439 /	2335 \	2328 \	2070 \	1747 \	1736 /	1643 \	
	OH-	OH-	OH -	Bicarb	CO <sub>2</sub>	H-OH	[HO-CO <sub>2</sub> ]-	CO <sub>2</sub>	CO <sub>2</sub>	CO <sub>2</sub>	C-O	C=O	Mono Carb	H <sub>2</sub> O	

After Heating		1543						1351						974	
After		1532 /				1386 /		1343 /				1224 /			958 /
100C	1570 -	1536 -	1520 -	1497 /	1470 /	1397 \	1374 -	1363 -	1290 /	1270 /	1251 /	1224 \		970 -	948 /
200C	1570 /	1536 /	1520 /	1497 \	1470 /	1401 /	1374 /	1363 /	1290 /	1270 /	1251 /	1224 \		974 /	948 /
300C	1570 \	1536 /	1520 /	1497 \	1470 /	1401 /	1374 /	1363 /	1290 /	1270 /	1251 /	1224 \		974 /	948 /
400C	1570 \	1536 \	1520 /	1497 \	1470 /	1401 /	1374 /	1363 /	1290 -	1270 /	1251 /	1224 \		974 /	948 /
500C	1570 \	1536 \	1520 /	1497 \	1470 -	1401 /	1374 /	1363 /	1290 \	1270 /	1251 /	1224 \	1090 /	974 \	948 /
	Biden Carb	Biden Nitrate	Mono Nitrate		Mono Carb		Mono Carb		Biden Nitrate	Mono Nitrate	Biden Carb	Bicarb	Mono Carb	Mono Nitrate	BaOH

**Table 2.5: DRIFTS Characterization of the Adsorption and Desorption  
of NO<sub>2</sub> Mixed Gas On Hydrotalcite**

After Heating						1586			1317 /	1290 /		1040	955 /
After Ads			2339 \		1659 /	1597 -	1580 /	1470 /		1290 /	1251 /	1032 /	955 -
100C	3688 /	2362 -	-	2193 -	1663 \	1597 /	1580 /	1490 /	1317 /	1290 /	1251 /	1040 /	978 /
200C	3688 /	2362 -	2324 /	2193 -	1663 \	1597 /	1580 /	1490 /	1317 /	1290 /	1251 /	1040 /	978 /
300C	3688 /	2362 -	2316 /	2193 -	1663 \	1597 /	1580 /	1490 /	1317 /	1290 /	1251 /	1040 /	978 /
400C	3688 /	2362 /	2316 /	2193 -	1663 \	1597 /	1580 /	1490 /	1317 \	1290 /	1251 /	1040 /	978 \
500C	3688 /	2362 /	2316 /	2193 /	1663 \	1597 /	1580 \	1490 /	1317 \	1290 /	1251 /	1040 /	978 \
	OH-	CO <sub>2</sub>	CO <sub>2</sub>	C-O	H <sub>2</sub> O	Biden Carb	Biden Nitrate	Mono Nitrate	Biden Carb	Biden Nitrate	Mono Nitrate	Biden Carb	Mono Nitrate

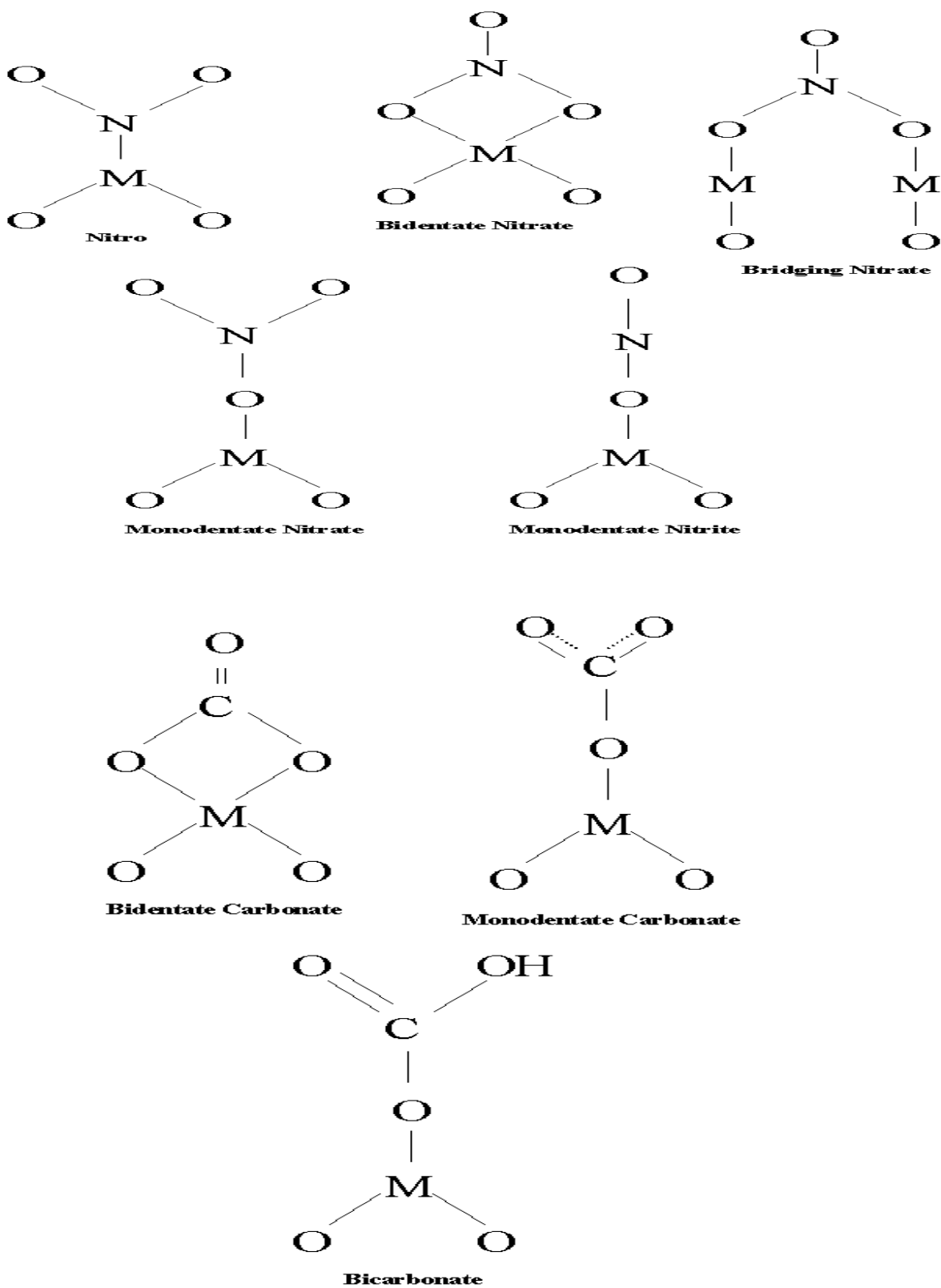
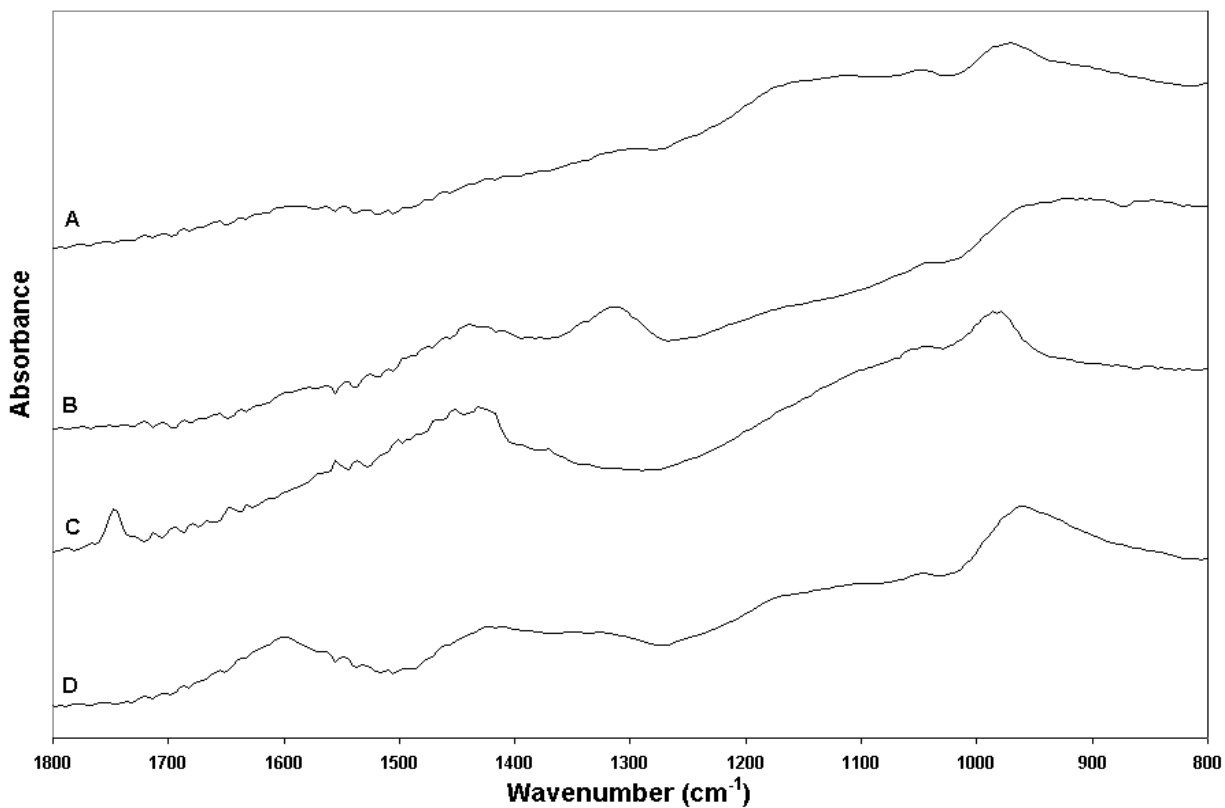
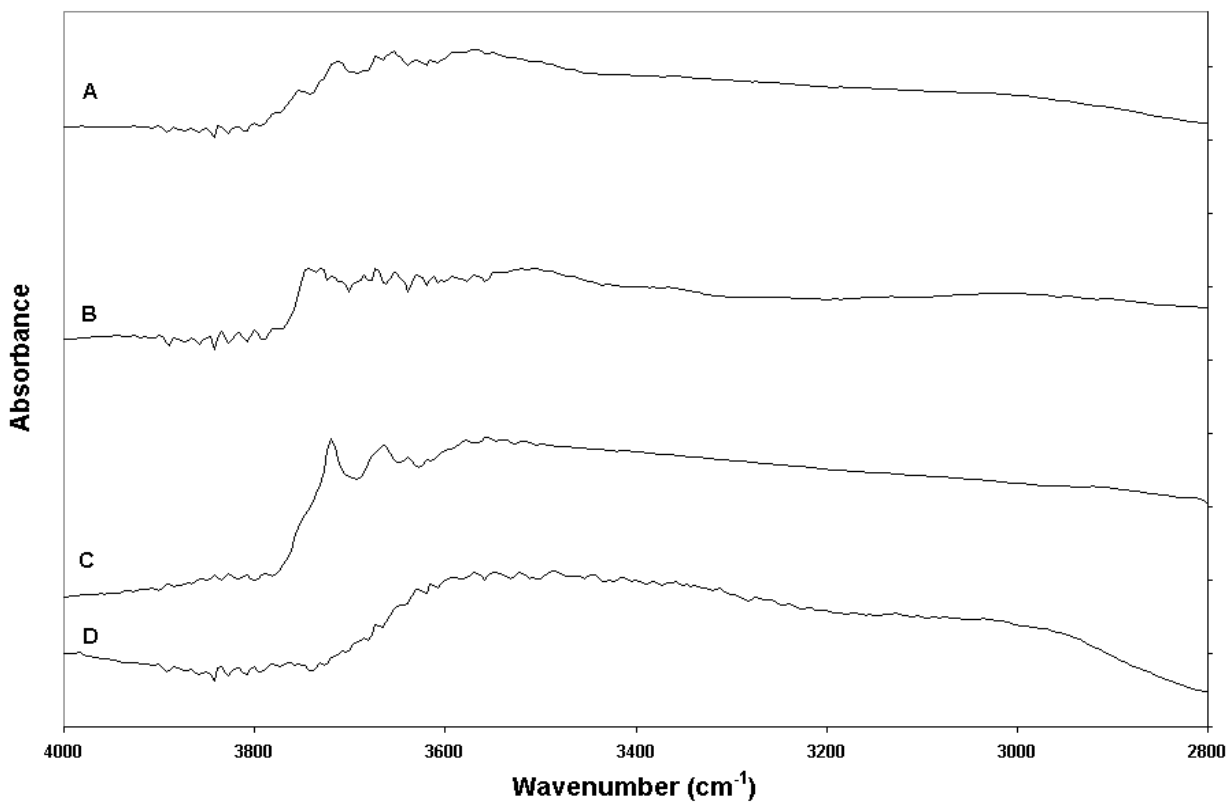
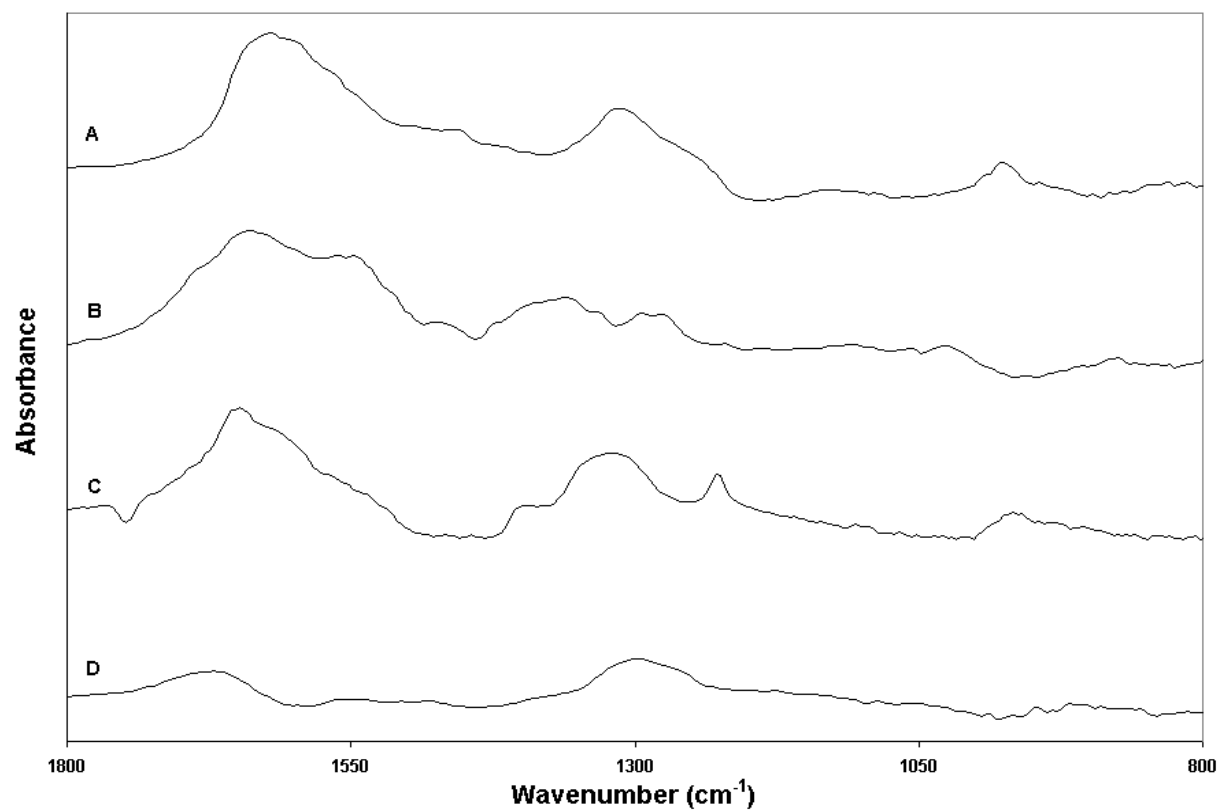
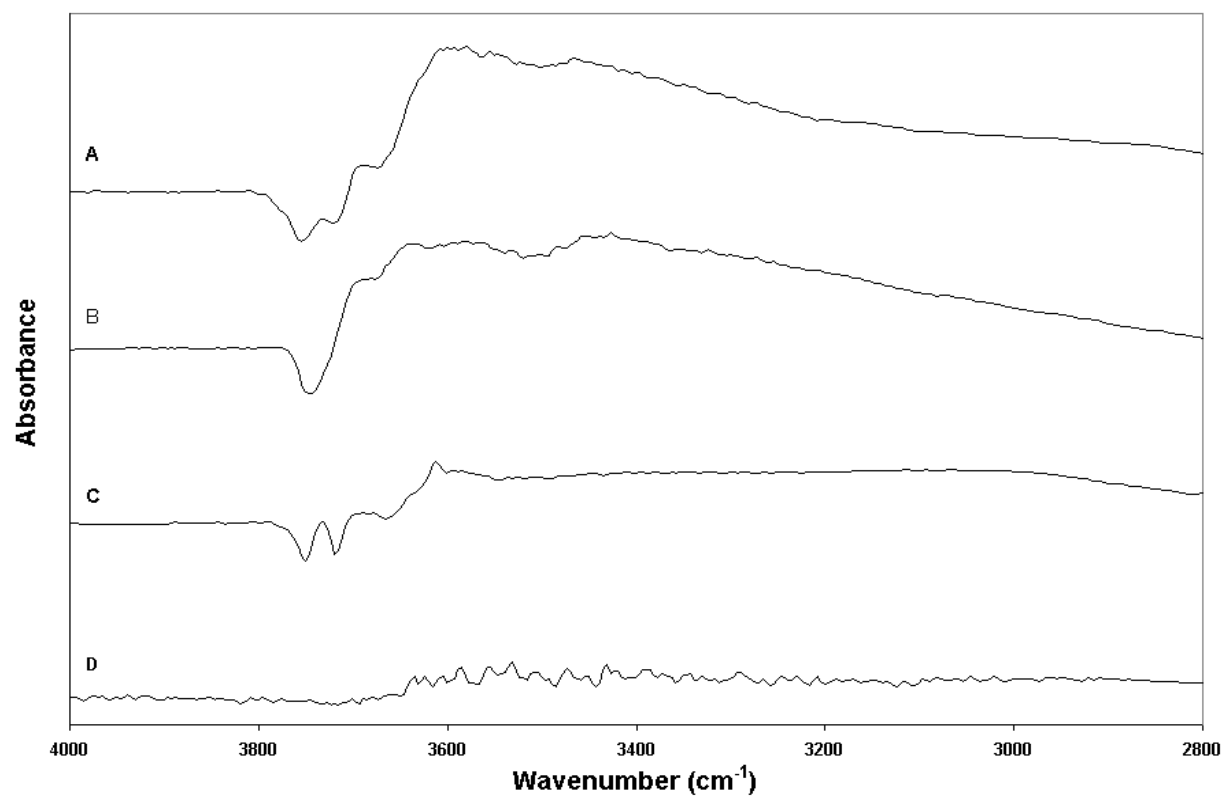


Figure 2.1: The structure of CO<sub>2</sub> and NO<sub>x</sub> Adsorbates on Oxide Surfaces



**Figure 2.2: Absorbance of (A)  $\text{Al}_2\text{O}_3$ , (B)  $\text{MgO}$ , (C)  $\text{BaO}/\text{Al}_2\text{O}_3$ , and (D) HT in He measured at 30°C after Soaking for 1 hour in He at 500°C with KBR as background.**



**Figure 2.3: Absorbance of (A)  $\text{Al}_2\text{O}_3$ , (B)  $\text{MgO}$ , (C)  $\text{BaO}/\text{Al}_2\text{O}_3$ , and (D) HT in He measured at 30°C after Adsorption and purge after**

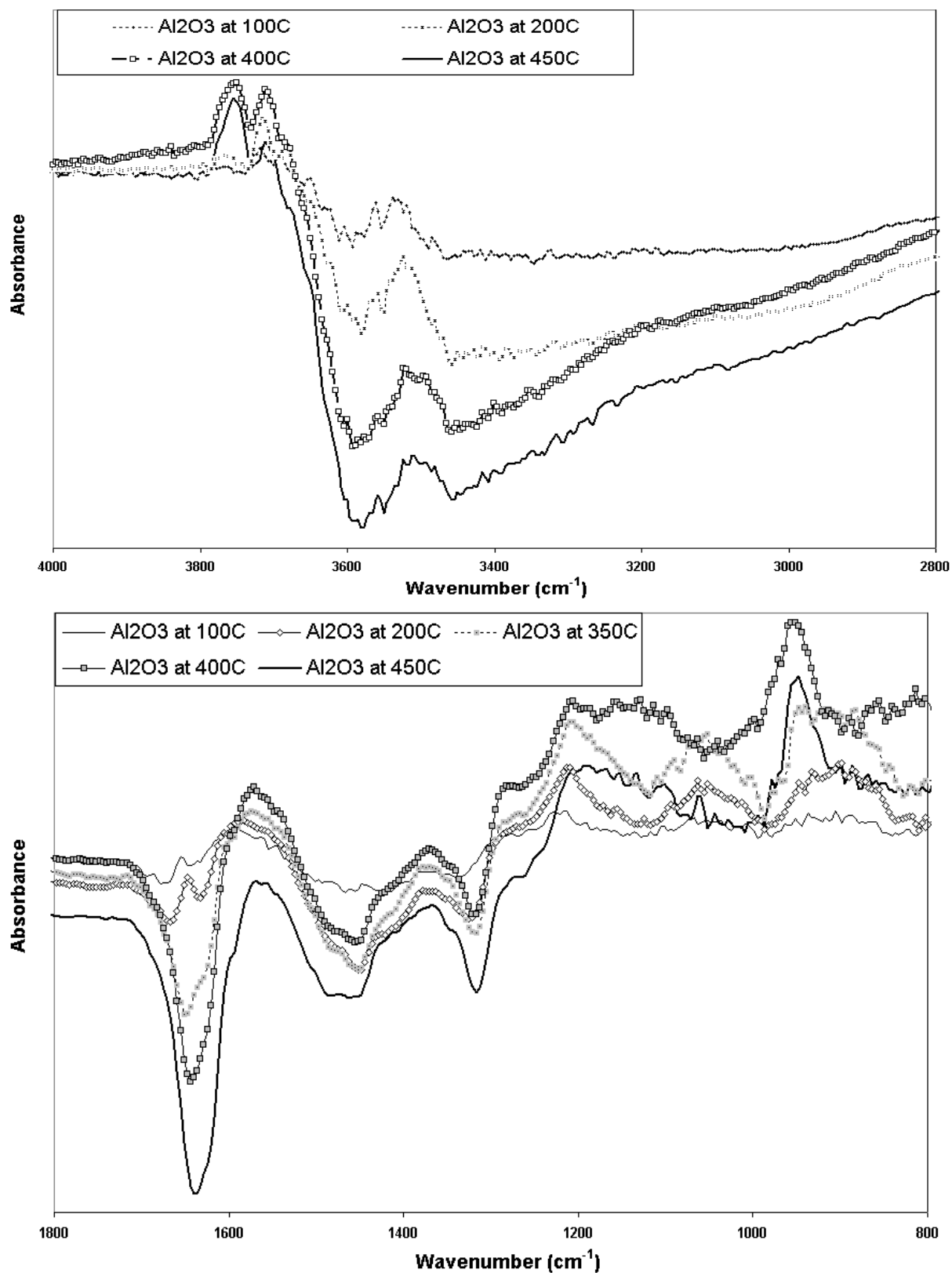
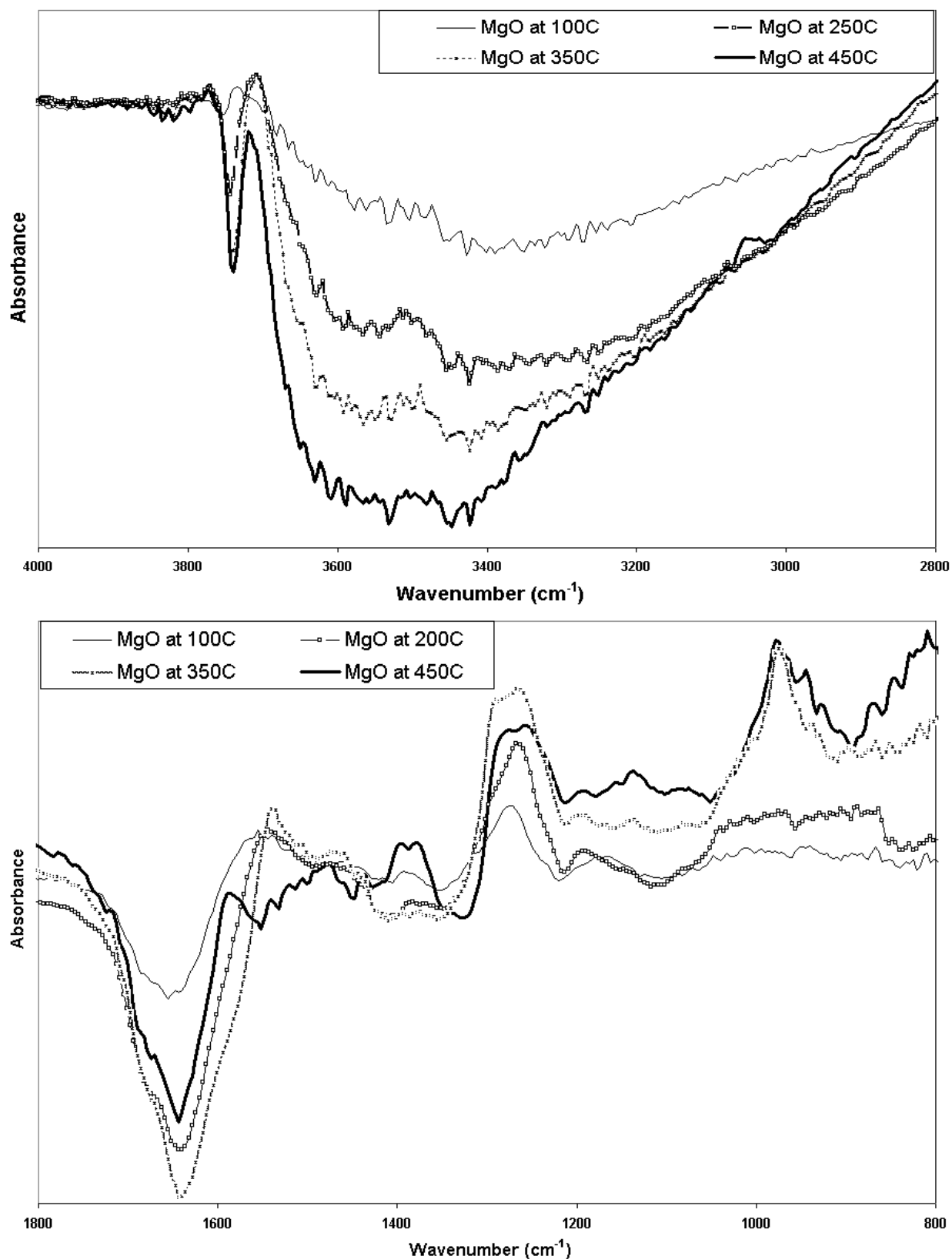


Figure 2.4: Absorbance of  $\text{Al}_2\text{O}_3$  during desorption at 100°C, 200°C, 250°C, 300°C, 350°C, 400°C, and 450°C with  $\text{Al}_2\text{O}_3$  after adsorption and purge subtracted from the spectrum.





**Figure 2.5: Absorbance of MgO during desorption at 100°C, 200°C, 250°C 350°C, 400°C, and 450°C with MgO after adsorption and purge subtracted from the spectrum.**

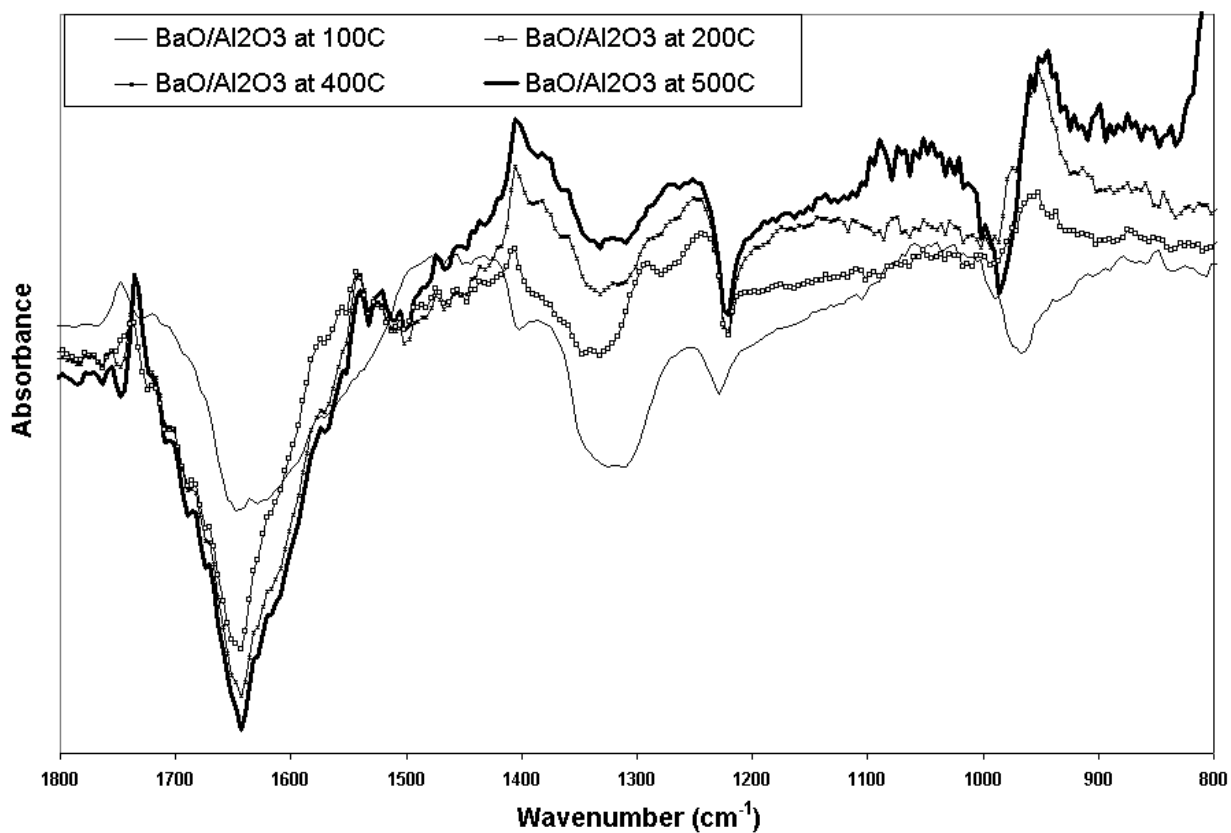
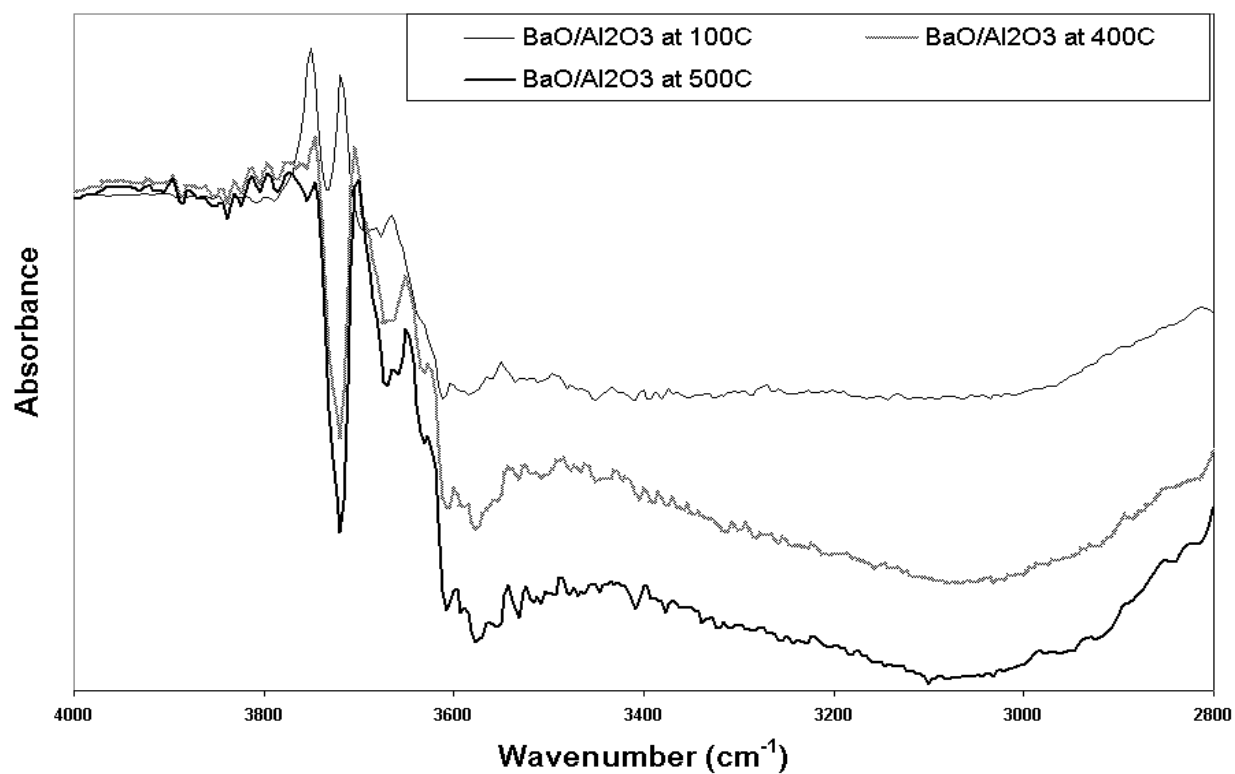
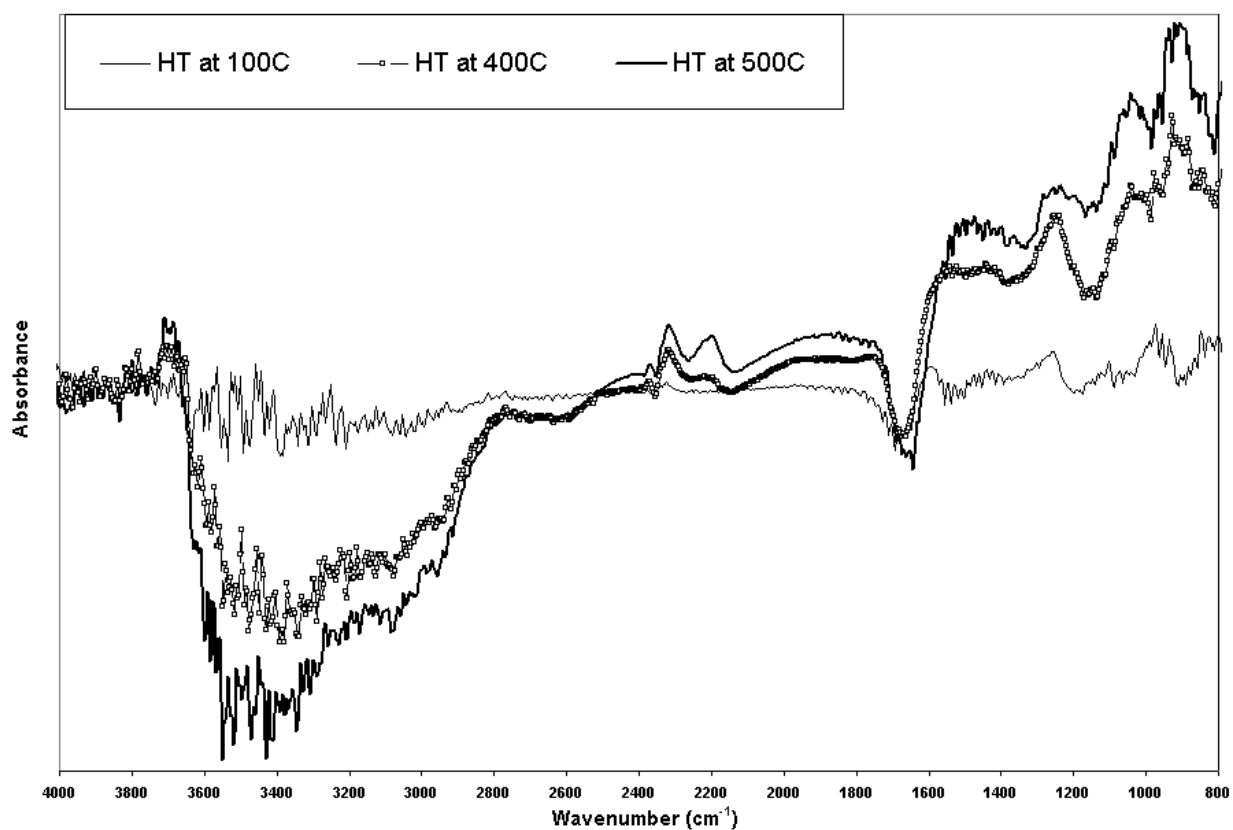


Figure 2.6: Absorbance of BaO/Al<sub>2</sub>O<sub>3</sub> during desorption at 100°C, 200°C, 300°C, 400°C, and 500°C with BaO/Al<sub>2</sub>O<sub>3</sub> after adsorption and purge subtracted from the spectrum.



**Figure 2.7: Absorbance of HT during desorption at 100°C, 200°C, 300°C 400°C, and 500°C with HT after adsorption and purge subtracted from the spectrum.**

**Chapter III:**  
**Characterization of NO<sub>x</sub> Storage Reduction by Pt/BaY and Pt/Nay Catalysts**

Bryan A. Silletti,<sup>1</sup> James J. Spivey,<sup>2</sup> and H. Henry Lamb\*

Department of Chemical Engineering,  
North Carolina State University  
Raleigh, NC 27695 USA

\*Author to whom correspondence should be addressed.

Phone: (919)-515-6395  
Fax: (919)-515-3465  
e-mail: lamb@eos.ncsu.edu

<sup>1</sup>Present Address: Caterpillar Inc., Mossville, Illinois

<sup>2</sup>Present Address: Department of Chemical Engineering, Louisiana State University, Baton Rouge, LA

## ABSTRACT

The NO<sub>x</sub> Storage-reduction catalyst is one of the leading technologies targeted to reduce NO<sub>x</sub> emissions from lean-burn internal combustion engines. In this work, NO<sub>x</sub> storage and reduction by Pt/NaY and Pt/BaY catalyst (each containing 0.4 wt% Pt) were investigated using temperature-programmed desorption (TPD) and temperature-programmed reduction (TPR). NO<sub>x</sub> storage was measured using a mixed gas containing 1000 ppm NO<sub>2</sub>, 20% CO<sub>2</sub>, and 12% O<sub>2</sub> in He. The results indicate that NO<sub>2</sub> adsorption on the zeolites at 25°C is characterized by two irreversibly bound states: a low-temperature TPD peak due primarily to NO and a high-temperature peak comprising NO + O<sub>2</sub> that is associated with decomposition of nitrate species. The NO<sub>2</sub> adsorption capacities of NaY and BaY at 25°C are similar, however NO<sub>2</sub> binds much more strongly to BaY than NaY. For NaY, 80% of the NO<sub>x</sub> desorbed below 100°C and the remainder desorbed as NO + O<sub>2</sub> below 200°C. The low-temperature TPD peak at 160°C accounted for approximately 60% of the NO<sub>2</sub> adsorption capacity of BaY, while ≈40% desorbed at 370°C as NO + O<sub>2</sub>. CO<sub>2</sub> was also more strongly adsorbed by BaY than NaY. The 1000 ppm NO<sub>2</sub> mixed gas and a NO + O<sub>2</sub> mixture containing nominally 0.75% NO and 15% O<sub>2</sub> in He were used to investigate NO<sub>x</sub> storage by Pt/BaY at 250°C. The results evidence that the thermal stability of the nitrate species is not affected by changes in gas composition and adsorption temperature. TPR in H<sub>2</sub> following NO<sub>x</sub> storage on Pt/BaY at 250°C indicated that NO<sub>x</sub> reduction (as evidenced by N<sub>2</sub> evolution) occurs at 225 – 250°C.

## INTRODUCTION:

The NO<sub>x</sub> adsorber is one of the leading technologies targeted to reduce NO<sub>x</sub> emissions from lean-burn internal combustion engines. Three-way exhaust catalysts are highly effective in reducing NO<sub>x</sub> emissions from spark ignition (SI) engines that operate under stoichiometric conditions; however, new regulations requiring a 95% decrease in NO<sub>x</sub> emissions from diesel engines and the automotive industry's shift toward lean-burn SI engines have created the need for new approaches to NO<sub>x</sub> emission reduction. The NO<sub>x</sub> adsorber stores nitrogen oxides as surface nitrite and nitrate species under lean conditions and periodically is regenerated via reduction releasing N<sub>2</sub> and H<sub>2</sub>O and/or CO<sub>2</sub> as byproducts. A prototypical NO<sub>x</sub> adsorber consists of noble metal nano-particles dispersed on an alkaline earth oxide-modified alumina support. The surface chemistry of the metal oxide adsorbent (support) and the noble metal (catalyst) are critical to the efficacy of the device. The narrow range of operating temperatures, thermal degradation, and deactivation by sulfur adsorption hinders the commercial viability of NO<sub>x</sub> adsorbers. Among a variety of other materials, Rh/Pt/BaO/Al<sub>2</sub>O<sub>3</sub> catalysts are very effective for NO<sub>x</sub> storage and reduction [47]. This material, however, readily deactivates in the presence of sulfur due to sulfate poisoning. Alkali and alkaline-earth metal exchanged faujasite (X and Y) zeolites have demonstrated a NO<sub>x</sub> storage mechanism that is not poisoned by SO<sub>2</sub> [47]. In this work, NO<sub>x</sub> storage-reduction was investigated over platinum-impregnated samples of Na- and Ba-Y zeolite by temperature-programmed desorption (TPD) and temperature-programmed reduction (TPR).

## EXPERIMENTAL METHODS

### *Catalyst Preparation*

Zeolyst International sodium-exchanged faujasite (20 g), sample CBV 100 with a  $\text{SiO}_2/\text{Al}_2\text{O}_3$  of 5:1 and a surface area of  $900 \text{ m}^2/\text{g}$ , was exchanged with 72 g of  $\text{Ba}(\text{NO}_3)_2$  dissolved in 800 ml of  $\text{H}_2\text{O}$  at  $90^\circ\text{C}$ . The barium was exchanged while stirring 400mL of the  $\text{Ba}(\text{NO}_3)_2$  solution with 20g of CBV 100 at  $90^\circ\text{C}$  for 2 h. The sample was then centrifuged and the solution was removed. The remaining solid was re-exchanged with 400mL of the  $\text{Ba}(\text{NO}_3)_2$  solution at  $90^\circ\text{C}$  for 2 h and then re-centrifuged. The sample was then washed with 250mL of DI water for 30 min in a stirred bath at  $90^\circ\text{C}$ , centrifuged, and the re-washed and centrifuged. Upon completion, the sample was heated in air with the following temperature program:

1. Ramp from  $30^\circ\text{C}$  to  $150^\circ\text{C}$  at  $2^\circ\text{C}/\text{min}$
2. Soak at  $150^\circ\text{C}$  for 1h
3. Ramp from  $150^\circ\text{C}$  –  $300^\circ\text{C}$  at  $2^\circ\text{C}/\text{min}$
4. Soak at  $300^\circ\text{C}$  for 1h
5. Ramp from  $300^\circ\text{C}$  –  $600^\circ\text{C}$  at  $5^\circ\text{C}/\text{min}$
6. Soak at  $600^\circ\text{C}$  for 2h
7. Cool from  $600^\circ\text{C}$  to  $25^\circ\text{C}$  at  $30^\circ\text{C}/\text{min}$

After calcination, the NaY and BaY samples were impregnated with 0.5% Pt by weight via incipient wetness using an aqueous solution of  $\text{H}_2\text{PtCl}_6$ .

The Zeolyst International commercial NaY faujasite was 13% percent by weight Na, while the BaY was exchanged using the method depicted in the experimental. Using ICP, it was determined that the BaY had 14.5% by weight Ba, 2% by weight Na, and .41% by weight Pt. It is assumed that the majority of the Na that remained in the material is located in the smaller sodalite cages. The elemental composition of a sample of Pt/BaY was determined by Galbraith Labs.

### *Temperature Programmed Desorption:*

TPD and TPR experiments were performed in a fixed bed microreactor consisting of a fritted quartz tube mounted in a vertical Lindberg furnace that is controlled by an Omega PID controller and a solid-state contactor. The catalyst bed temperature is measured using a Type K thermocouple interfaced to a PC via a Metrabyte device. The reactor effluent was sampled continuously using a quadrupole mass spectrometer (QMS) with a high-pressure gas inlet system. A certified gas mixture (National Welders) containing 1000 ppm NO<sub>2</sub>, 20% CO<sub>2</sub>, 12% O<sub>2</sub> in balance He was used in NO<sub>2</sub> TPD experiments. The gas composition and concentration for the NO + O<sub>2</sub> adsorption runs were 0.85% NO and 15% O<sub>2</sub> with a He balance. Ultrahigh purity He and CO<sub>2</sub> were supplied by National Welders. Gases were metered using calibrated flow controllers (rotameters).

For each test, a 200mg sample was placed in a quartz reactor and pretreated in H<sub>2</sub> at 30 cc/min to 400°C and soaked for 1 hour followed by a He purge. The adsorption run was completed by heating to the desired temperature and adsorbing the mixed NO<sub>2</sub> gas or mixed NO gas system at 45cc/min at the desired temperature (30°C and 250°C) for 1 hour. After adsorption the sample was purged in He at the same temperature for 40 minutes and allowed to cool to 30°C. For the TPD, the sample was then heated at a rate of 10°C/min to 550°C during desorption in a He flow rate of 35cc/min. For TPR, the sample was then heated at a rate of 10°C/min to 550°C during desorption in a H<sub>2</sub> flow rate of 30 cc/min.



## Results and Discussion

To investigate these materials, CO<sub>2</sub> was used to compare the basicity of the NaY with the BaY. The use of CO<sub>2</sub> as an acidic probe to search for basic sites on oxide materials is well documented. As a result, we compared the adsorption of CO<sub>2</sub> at 100°C and subsequent desorption to investigate the nature of the basicity of the basic exchanged faujasites. The results of the TPD, as depicted in Figure 3.1, indicate that there is little difference in the CO<sub>2</sub> desorption temperature and total capacity of CO<sub>2</sub> adsorption. Although the theoretical calculations, as given by Barthomeuf, indicate that the alkali metal exchanged faujasite, NaY, should be more basic than the alkaline earth exchange faujasite, BaY, the CO<sub>2</sub> study did not illustrate this character. Barthomeuf correlated the oxygen charge relative to the ionization potential of the exchanged cation indicating that Na has increased basicity relative to Ba due to the increased oxygen charge. Experimentally, it is difficult to characterize the basicity of zeolites using probe molecules. In zeolites, CO<sub>2</sub> adsorption measures more of the overall property of the materials including the structure effects and not just the basic exchanged cation effect as it is more involved with adsorption on the cation then the basic oxygen anion [47]. The metal oxygen bonds and their interaction as well as charge balance with the structure of zeolites define the nature of the basicity of the material. In general, replacing of an atom in the framework with an atom of lower vacancy creates a negative charge on the framework, which has to be neutralized by a metal cation [47]. Adsorbates must approach the lattice oxygen that favors the least physical and chemical constraints. During adsorption and catalysis, the reactant is able to choose which oxygen to interact with, depending on the oxygen atom charge, access, and neighboring configuration [47]. Since it is the basic oxygen anion charge that is most dependent on the exchanged cation and CO<sub>2</sub> cannot differentiate this specific effect from the nature of the

entire structure, it cannot be used to characterize the basicity difference between the two materials.

With these same materials, adsorption of the  $\text{NO}_2$  mixed gas at  $30^\circ\text{C}$  was investigated to understand the nature of all the sites involved in  $\text{NO}_2$  and  $\text{CO}_2$  adsorption. Figure 3.2 documents the distinctions between the TPD profiles of the  $30^\circ\text{C}$  adsorption on both NaY (Plot A) and BaY (Plot B). The overall  $\text{NO}_x$  capacity is equivalent in NaY and BaY. The cation exchange process did not affect the total number of sites, but it did affect the nature and strength of the sites for  $\text{NO}_x$  and  $\text{CO}_2$  adsorption. Although NaY is more basic than BaY, BaY has more high-temperature capacity for  $\text{NO}_x$  adsorption, indicating basicity alone is not the only driver for  $\text{NO}_x$  adsorption and storage. The adsorbed  $\text{NO}_x$  on BaY has a greater thermal stability and the peaks are broader due to the mixture of Na and Ba activated oxygen anions. In both the NaY and BaY, the lower temperature  $\text{NO}_x$  desorption is primarily associated with reversible  $\text{NO}_2$  desorption without the  $\text{O}_2$ , while the high temperature desorption yields  $\text{NO} + \text{O}_2$  in a ratio of 4:1 in NaY and 2.6:1 in BaY. The decomposition of bulk magnesium nitrate under the same TPD program is 1.45:1 as depicted in the Appendix II. The NaY has little to no  $\text{CO}_2$  adsorption in the presence of  $\text{NO}_2$ , while the BaY has a significant amount of  $\text{CO}_2$  that desorbs at approximately  $70^\circ\text{C}$ . Part of this is associated with the divalent versus monovalent ion that enables a well dispersed Ba ion to adsorb  $\text{CO}_2$ , while the Na is unable to adsorb the same species unless in the presence of a cluster of Na ions that can charge balance the  $\text{CO}_2$  in the cage. The  $\text{NO}_2$  molecule however only needs a +1 charged ion to form a nitrate or surface bound  $\text{NO}_2$  species and can more easily bind with the Na.

For the purposes of  $\text{NO}_x$  storage reduction, adsorption capacities at  $250^\circ\text{C}$  are more consistent for a diesel engine exhaust. In order to study independently, the storage mechanism

separate from the oxidation process, two separate gas mixtures were used to characterize the NO<sub>x</sub> oxidation and storage functions on BaY, Pt/BaY and NaY at 250°C. In figure 3.3, the storage of the NO<sub>2</sub> mixed gas was studied on BaY(plot A), Pt/BaY (Plot B) and NaY(Plot C). At this temperature, the reversible NO<sub>2</sub> adsorption is not present and only the nitrate decomposition products of NO + O<sub>2</sub> are desorbed. The stoichiometry of NO:O<sub>2</sub> is 3:1 on BaY, 3.5:1 on Pt/BaY, and 2.4:1 on NaY. BaY and Pt/BaY exhibit very similar capacities at 50 and 45 μmols/g, while NaY has very little capacity at 7 μmols/g. The strength of adsorption on the samples is as follows BaY > Pt/BaY > NaY.

In the second condition, the combined oxidation + storage mechanism was investigated using a mixture of NO and O<sub>2</sub> in the gas stream. The concentration of NO is 0.85% and O<sub>2</sub> is in excess at 15% with the balance in He. As can be seen in Figure 3.4, the character of the desorption profile is the same as in Figure 3. The stoichiometry of NO:O<sub>2</sub> is 2.6:1 on BaY and 3.6:1 on Pt/BaY. The total capacity of adsorption is higher with Pt/BaY because BaY does not have adsorption capacity for NO, only NO<sub>2</sub>. The thermodynamic equilibrium of NO:NO<sub>2</sub> at 250°C is 95% NO<sub>2</sub> as depicted in Figure 3.9. NO is stable with respect to NO<sub>2</sub> formation in the absence of O<sub>2</sub>, but in the presence of Pt, NO is converted to NO<sub>2</sub> more readily and will approach the equilibrium concentration. For this reason, the amount of adsorbed NO<sub>x</sub> on Pt/BaY is 190 μmols/g, while the BaY is only 120 μmols/g after 1 hour of adsorption.

Although NaY has little capacity for NO<sub>2</sub> adsorption at 250°C, it does have capacity for NO and NO + O<sub>2</sub> at 250°C. As documented by Martens et al, NaY, in the absence of H<sub>2</sub>O, can form N<sub>2</sub>O<sub>3</sub> which “undergoes heterolytic splitting into a nitrosonium cation and a nitrite and or a nitrate anion.”[48] The subsequent nitrite ion desorbs at NO. Figure 3.5 depicts the adsorption and desorption of NO after adsorption at 250°C on NaY (Plot A) and Pt/NaY (Plot B). In the

case of NaY, there is no oxygen desorbed, indicating the adsorbed species is primarily a nitrite. In Pt/NaY, however, the NO:O<sub>2</sub> ratio is 13:1, indicating there is a mixture of nitrate and nitrite formed. The same character of the desorption plots is present in Figure 3.6, when NO + O<sub>2</sub> is adsorbed at 250°C on the same materials. Similarly, there is no O<sub>2</sub> desorbed on NaY, but an equivalent amount of O<sub>2</sub> is desorbed on Pt/NaY. Thus, in the presence of Pt, the adsorbed N<sub>2</sub>O<sub>3</sub> is capable of forming the nitrate species, while in NaY, only the nitrite ion is formed. Table 3.1 summarizes the amount of NO<sub>x</sub> adsorbed by each sample under the various conditions.

The final mechanism of the NSR catalyst, is the reduction of NO<sub>x</sub> in the presence of H<sub>2</sub>, HC, or CO as a reductant. In the final study of these materials, the same adsorption experiments were completed, but were followed with a temperature programmed reduction at 10°C/min in the presence of N<sub>2</sub>. In figure 3.7, the TPR experiments were carried out on both BaY and Pt/BaY to understand the effect of the noble metal in the catalytic reduction of adsorbed NO<sub>x</sub> species. In plot A, in the absence of Pt, the adsorbed NO<sub>x</sub> is reduced to N<sub>2</sub> and N<sub>2</sub>O, but at a peak temperature of 325°C with a broader and irregular profile. In plot B, in the presence of Pt, the reduction is reduced to 260°C and there are no byproducts. Figure 3.8 documents the same experiment after adsorption of NO + O<sub>2</sub> on the identical samples. In this case, Pt again activates the reduction of the stored NO<sub>x</sub> at 225°C instead of 350°C. The reduction of the adsorbed NO<sub>x</sub> in the absence of Pt indicates the presence of two different reducible species.

## Conclusions

In this study, we demonstrated the capability of Pt impregnated NaY and BaY to function as a NO<sub>x</sub>SR catalyst. Both NaY and BaY exhibit NO<sub>x</sub> storage capacity for both nitrite and nitrate formation at 30°C. Pt/BaY was able to store NO<sub>x</sub> up to 400°C. Pt/BaY demonstrated

effective NO oxidation and NO<sub>2</sub> storage as a nitrate with sufficient thermal capacity required for a NO<sub>x</sub>SR catalyst. In addition, using H<sub>2</sub>, the stored NO<sub>x</sub> was completely reduced to N<sub>2</sub> without any byproducts. Pt/NaY, however, does not have adequate capacity for NO<sub>2</sub> storage reduction at 250°C, but it does have marginal capacity for NO storage at 250°C. The species formed is a mixed nitrate and nitrite on the Pt/NaY, while purely a nitrite on the NaY.

**Table 3.1: Thermal Stability and Storage Capacity Comparison of NO<sub>x</sub> Adsorption on NaY, BaY, Pt/NaY, Pt/BaY**

Catalyst	Desorption Temperature		Storage Capacity @ 250°C (μmols/g)			
	T <sub>des</sub> - NO <sub>2</sub> Ads	T <sub>des</sub> - NO Ads	NO <sub>2</sub> Ads	NO/O <sub>2</sub> Ads	NO Ads	CO <sub>2</sub> (100°C)
Pt/BaY	370°C	-	45	190	0	-
Pt/NaY	-	320°C	-	35	36	-
NaY	320°C	350°C	5	47	26	28
BaY	400°C	-	50	120	0	30

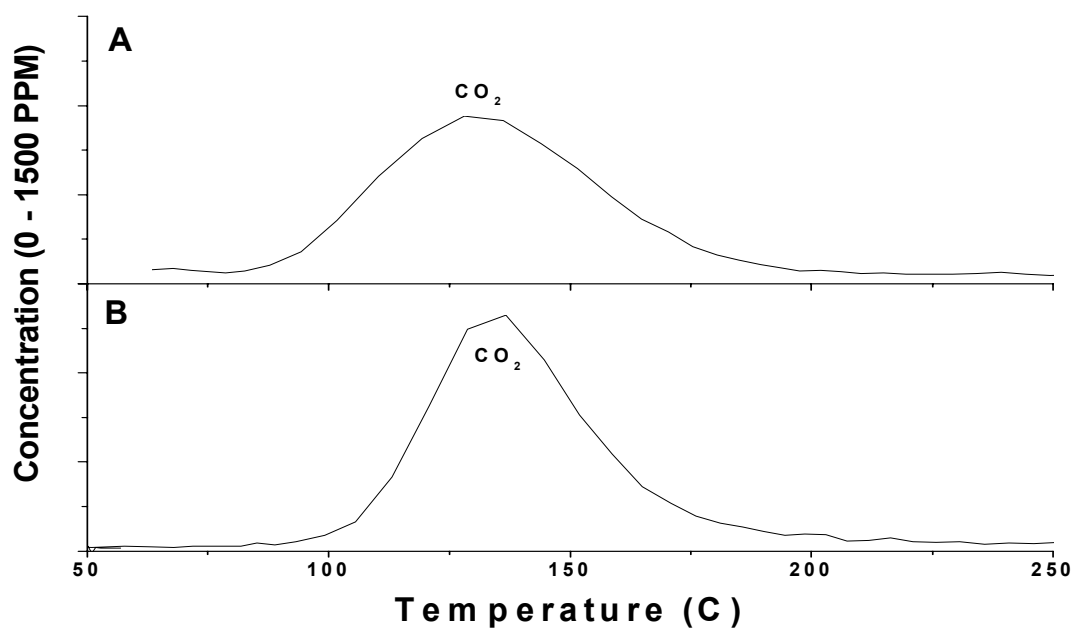


Figure 3.1: TPD: 100°C Adsorption of CO<sub>2</sub> on (A) NaY and (B) BaY

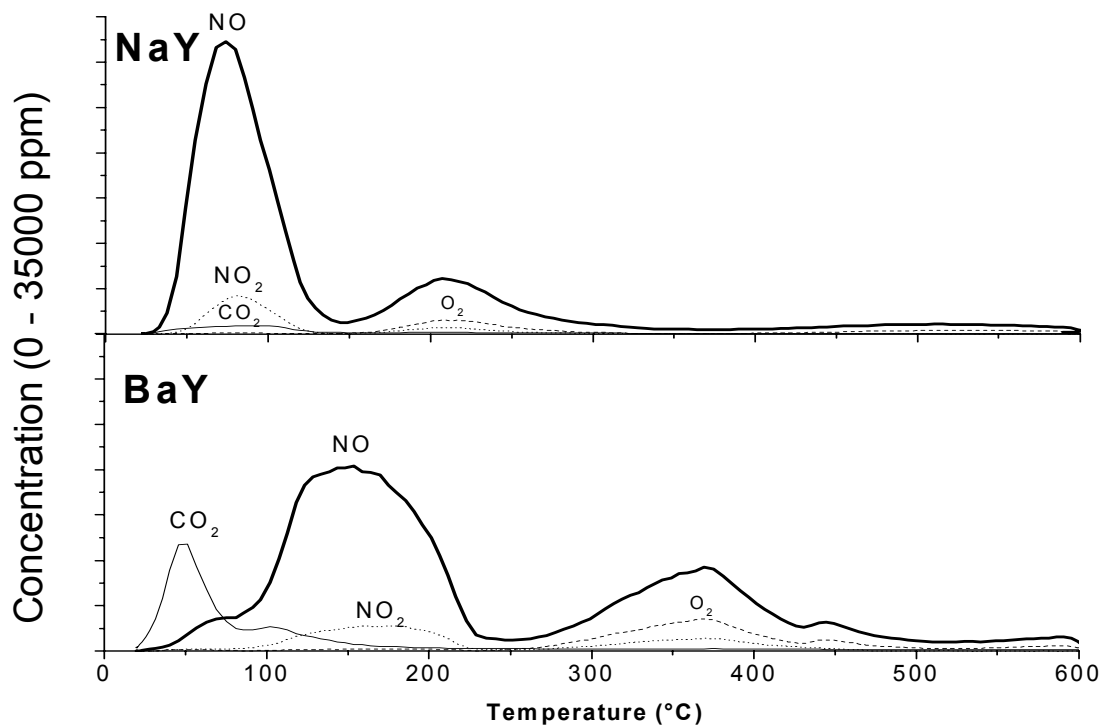


Figure 3.2: TPD: 4 hour 30°C Adsorption of NO<sub>2</sub> Mixed Gas on (A) NaY and (B) BaY

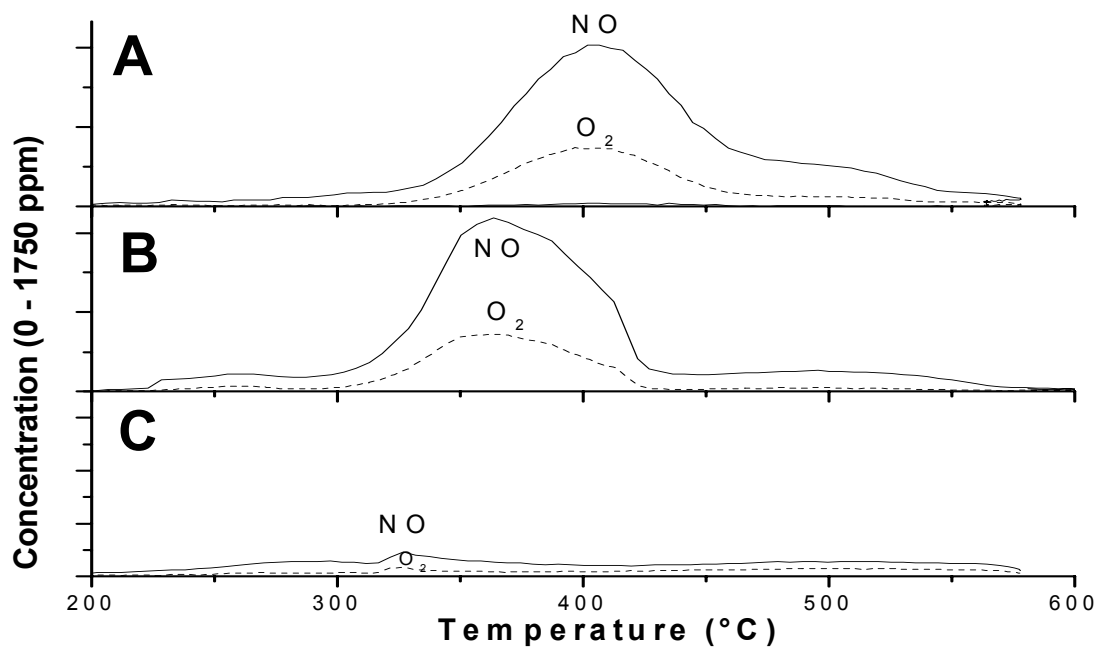


Figure 3.3: TPD: NO<sub>2</sub> Adsorption at 250°C on (A) BaY (B) Pt/BaY (C) NaY

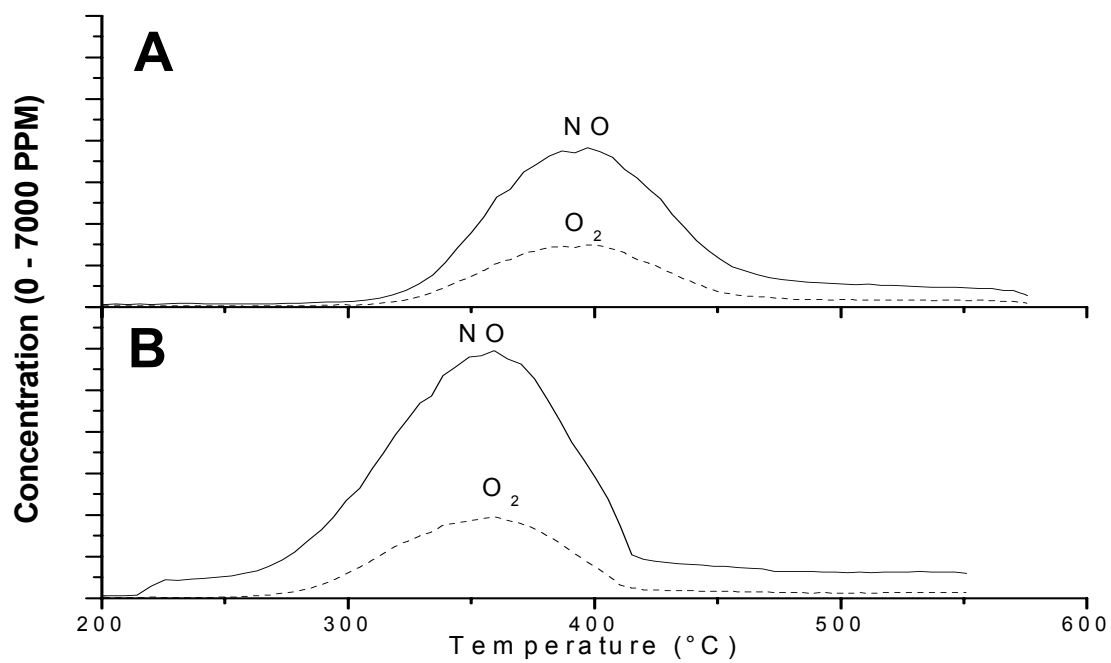
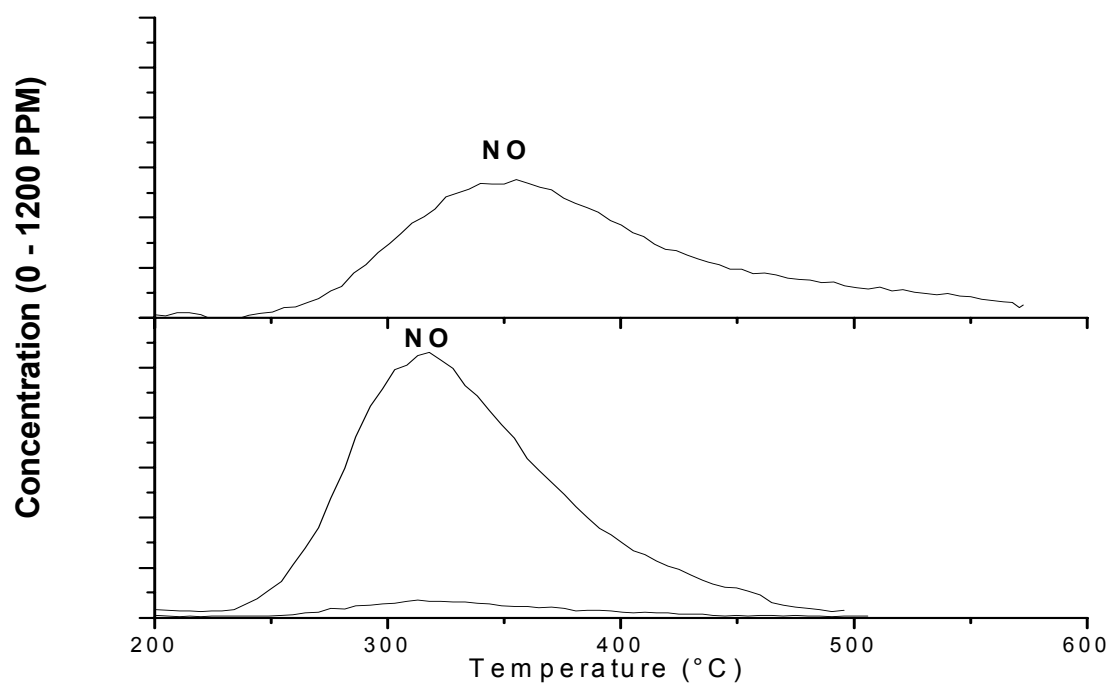
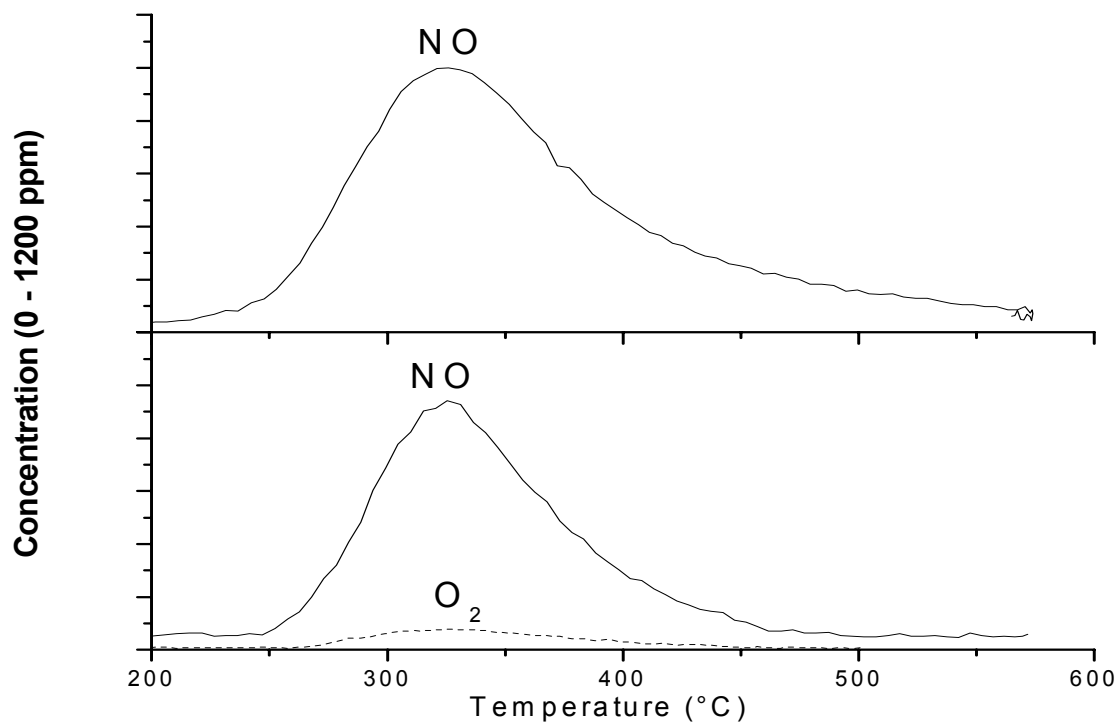


Figure 3.4: TPD: NO + O<sub>2</sub> Adsorption at 250°C on (A) BaY (B) Pt/BaY





**Figure 3.5: TPD: NO adsorption at 250°C (A) NaY and (B) Pt/NaY**



**Figure 3.6: TPD: NO + O<sub>2</sub> adsorption at 250°C (A) NaY and (B) Pt/NaY**

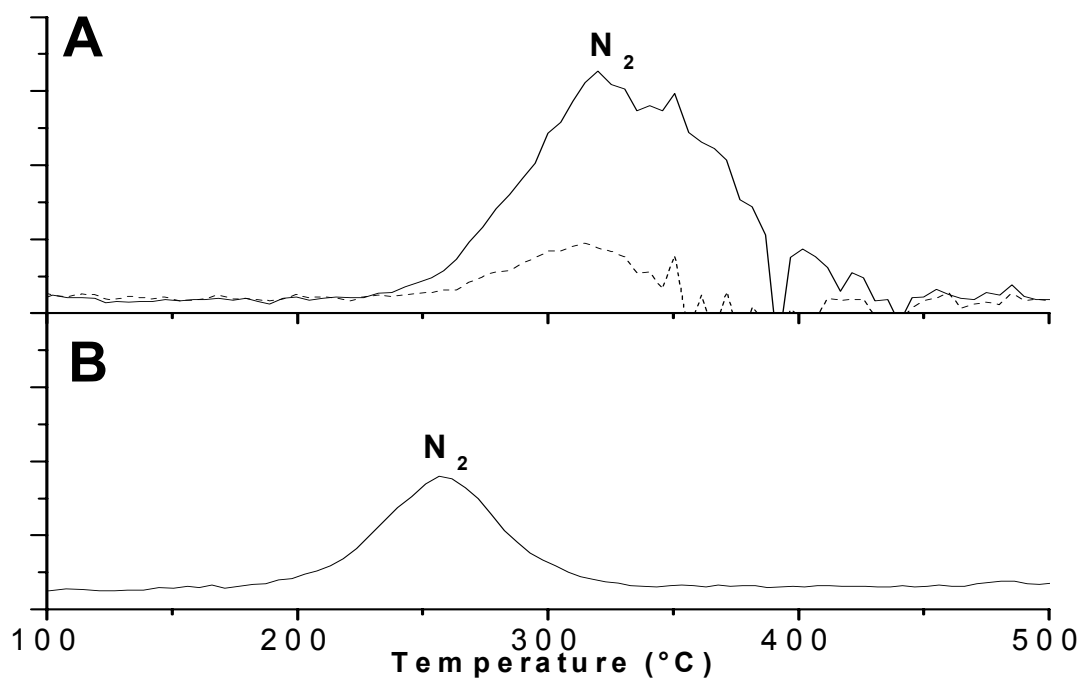


Figure 3.7: TPR( $H_2$ ):  $NO_2$  adsorption at 250C for 1 hour (A) BaY and (B) Pt/BaY

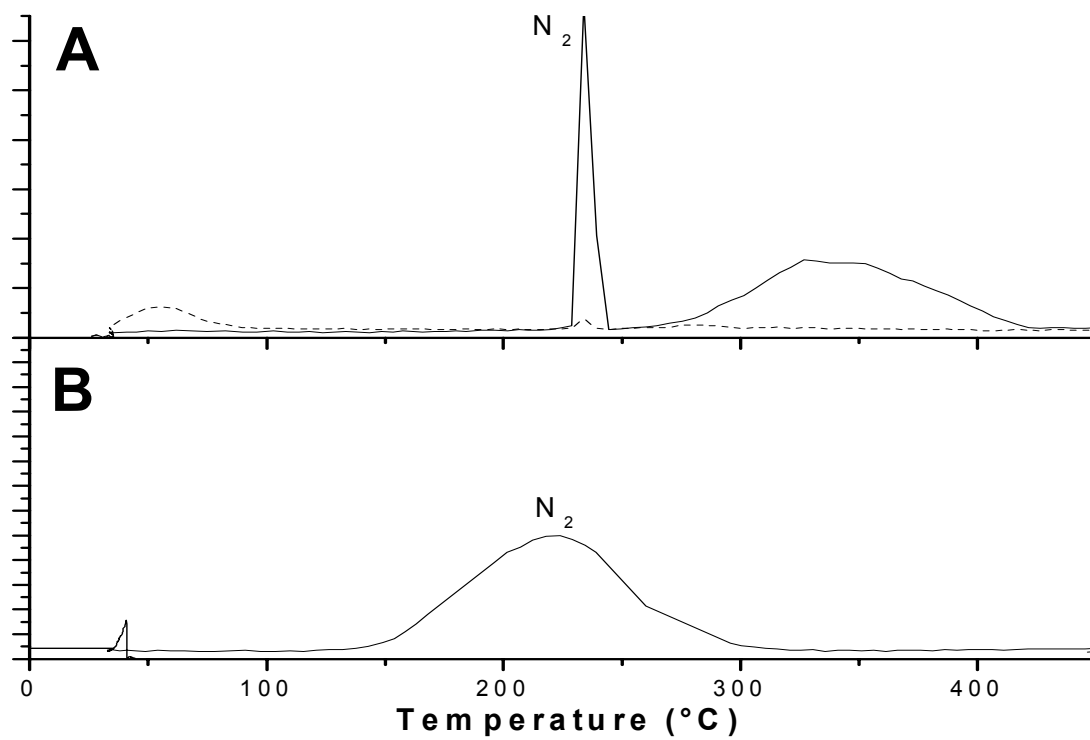
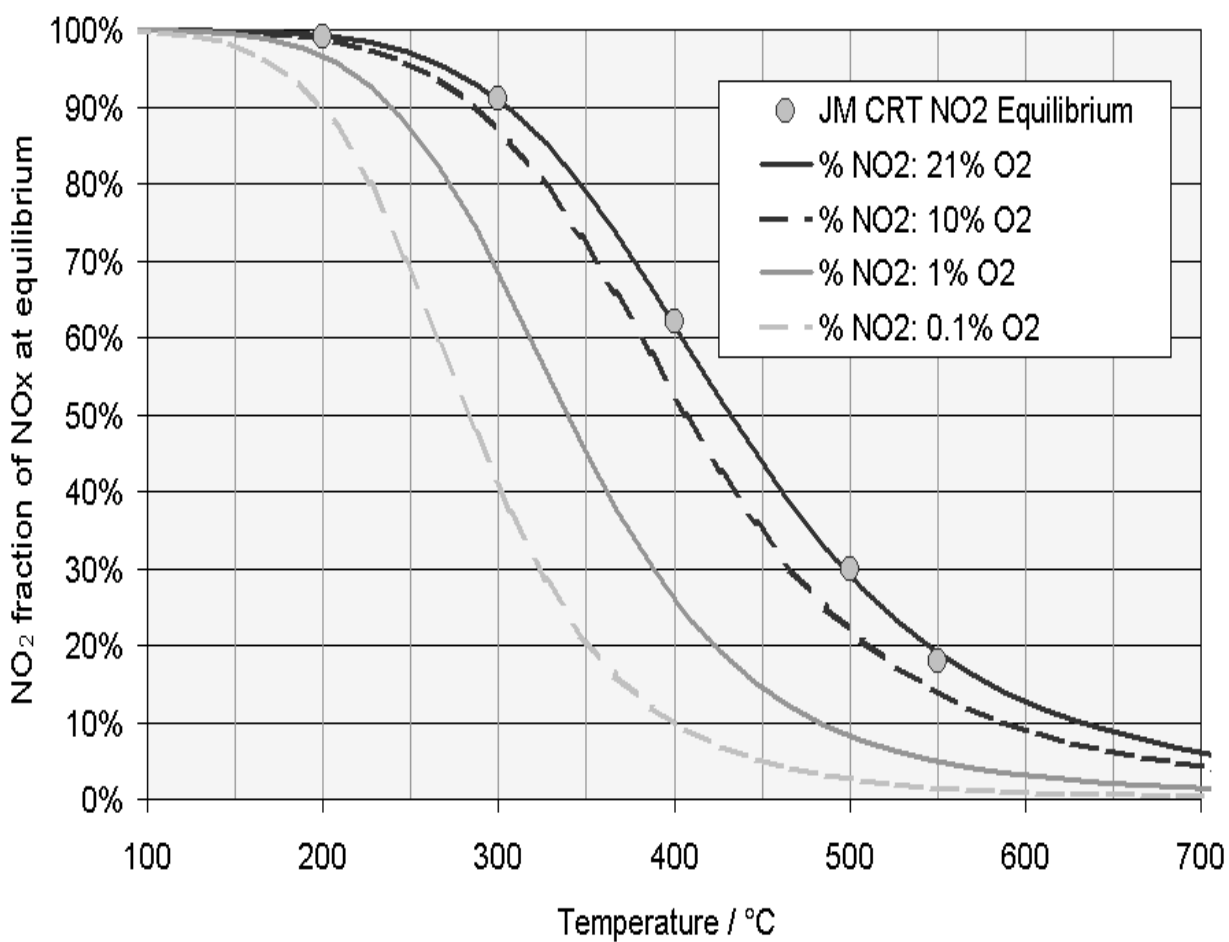
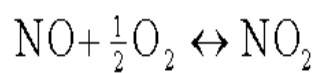


Figure 3.8: TPR( $H_2$ ):  $NO + O_2$  adsorption at 250C for 1 hour (A) BaY and (B) Pt/BaY



**Figure 3.9: NO<sub>2</sub>/NO equilibrium ratio as a function of temperature and O<sub>2</sub> concentration [49, 50, 51]**

## Conclusions and Outlook

The goals of this research were two-fold: (1) to elucidate the adsorption sites for NO<sub>2</sub> and CO<sub>2</sub> on basic metal oxides and (2) to investigate materials derived from Na- and Ba-exchanged Y zeolite (with and without added Pt) as NO<sub>x</sub>SR catalysts.

Competitive adsorption of CO<sub>2</sub> and NO<sub>2</sub> on basic metal oxides (MgO,  $\gamma$ -Al<sub>2</sub>O<sub>3</sub>, MgO/Al<sub>2</sub>O<sub>3</sub>, BaO/Al<sub>2</sub>O<sub>3</sub>, and a hydrotalcite-derived Mg-Al oxide) was investigated to better understand the nature of the NO<sub>2</sub> adsorption sites and to determine the effect on NO<sub>x</sub> storage capacity. CO<sub>2</sub> has a strong affinity for basic surface sites (both oxide ions and basic hydroxyl groups), whereas NO<sub>2</sub> adsorbs at oxygen vacancies and may interact with acid/base sites. CO<sub>2</sub> adsorption on basic metal oxides results in carbonate and bicarbonate surface species. NO<sub>2</sub> adsorption on basic metal oxides yields two surface species: a nitrite species that desorbs as NO between 100 - 300°C leaving oxygen on the surface and a nitrate species that desorbs as NO + O<sub>2</sub> (NO:O<sub>2</sub> ~ 1.33) between 375 - 500°C. A fraction of the nitrite species is converted to nitrate species during TPD suggesting that it may be a precursor of the latter. BaO/Al<sub>2</sub>O<sub>3</sub> has the highest basic site density and exhibits the strongest base strength as measured by CO<sub>2</sub> TPD. Based on the IR results, BaO/Al<sub>2</sub>O<sub>3</sub> formed the largest concentration of surface bicarbonate and physisorbed CO<sub>2</sub> after adsorption of the NO<sub>2</sub> mixed gas at 30°C. The strong basicity of BaO is consistent with simple electronegativity difference predictions since Ba is the more electropositive element (among Mg, Ba, and Al). The stronger basicity of BaO results in greater competition between NO<sub>2</sub> and CO<sub>2</sub> reducing the effective capacity for NO<sub>x</sub> adsorption. Adsorbed CO<sub>2</sub> species were formed on the other metal oxides albeit in much smaller concentrations. On MgO and Mg-doped Al<sub>2</sub>O<sub>3</sub>, although there is competition between CO<sub>2</sub> and NO<sub>2</sub> particularly at high temperature, there is always a significant amount of additional capacity for NO<sub>2</sub> storage relative to the loss in

CO<sub>2</sub> capacity. This indicates that there are additional sites for NO<sub>2</sub> adsorption that are not active for CO<sub>2</sub> adsorption.

The second phase of our experimental program was to investigate the use of alkali and alkaline-earth metal exchanged faujasite as NO<sub>x</sub>SR catalysts. The exchangeable cations in zeolites are not part of the aluminosilicate framework but are present as isolated charge-compensating cations within the nanoscale pores of the molecular sieve. The nanoscale pores and the unique local chemical environment of Na and Ba ions in faujasite can result in novel adsorption phenomena for gases such as NO<sub>2</sub>, CO<sub>2</sub>, and SO<sub>2</sub>. For example, NaY, in contrast to BaY, is not susceptible to CO<sub>2</sub> nor SO<sub>2</sub> adsorption in the presence of NO<sub>2</sub> [52]. Although NaY is more basic than BaY, the site-specific NO<sub>2</sub> adsorption strength on BaY is stronger than on NaY indicating that basicity in cation-exchanged faujasites does not correlate directly to NO<sub>x</sub> storage capacity. Our results evidence a higher NO<sub>2</sub> adsorption capacity and adsorption strength (nitrate thermal stability) for BaY. The adsorbed species formed in NaY are a mix of nitrite and nitrate species with a distinct NO:O<sub>2</sub> stoichiometry relative to the oxide materials. While NaY does not have significant NO<sub>x</sub> capacity above 250°C, it can behave as a low temperature NO<sub>x</sub>SR catalyst where the peak exhaust temperatures are below 250°C.

Our results demonstrate that Pt/BaY is able to catalyze the oxidation of NO to NO<sub>2</sub>, store NO<sub>2</sub> as a nitrate species, and catalyze nitrate reduction in the presence of H<sub>2</sub>. The Pt was introduced by incipient wetness impregnation using chloroplatinic acid resulting in relatively large Pt nanoparticles on the external surfaces of the faujasite crystals; therefore, the Pt was not in direct (intimate) contact with the intrazeolitic nitrate species. The catalytic effect of Pt was evidenced by a ~75°C decrease in the required NO<sub>x</sub> reduction temperature (relative to BaY in the absence of Pt). Even with Pt, the stored NO<sub>x</sub> was not reduced until 225°C indicating that the

reduction with  $H_2$  is either kinetically slow or diffusion limited. Without Pt, stored  $NO_x$  on the  $BaO/Al_2O_3$  was not reduced until approximately  $350^\circ C$ , while in the presence of Pt stored  $NO_x$  was reduced at room temperature.

The capacity and susceptibility of Ba to carbonate formation will vary due to its electronic environment. As a supported oxide, BaO is most susceptible to competitive adsorption of  $CO_2$  and  $SO_2$ , yet it has the largest  $NO_2$  capacity. When Ba is present with Al in a spinel structure, the material is much less prone to carbonate formation [53]. Lastly, in Y zeolite, the Ba is only susceptible to  $CO_2$  at low temperatures and is not active for  $CO_2$  adsorption at  $250^\circ C$ , while  $SO_2$  readily deactivates Ba in the zeolite cage. This gives credence to the fact that the basic ion is more susceptible to the more acidic  $SO_3$  molecule and basicity of the ion drives the interaction in the specific zeolite material.

Although  $NO_2$  can react with Lewis basic sites, it also can react with Lewis acid and vacancy sites as it is a free radical and can donate the lone electron for bonding. On  $CO_2$  and  $SO_3$ , the central atom becomes electropositive because the more electronegative oxygen atoms draw the electrons away. With this partial positive charge, both  $CO_2$  and  $SO_3$  (although more strongly) are very active for basic surface sites. Neither molecule has extra electrons to donate to the surface of the oxide, while  $NO_2$  is able to exchange with either an acidic or a basic surface. More particularly, by exploiting the electron donating properties,  $NO_2$  can adsorb on an acidic electron accepting surface that would only be active for  $NO_2$  adsorption. By understanding the nature of the  $NO_2$  molecule and the susceptibility of the surface for  $NO_x$  adsorption, it is possible to tailor ion conductivity in surfaces that would promote  $NO_2$  adsorption and prevent the susceptibility to  $CO_2$  and  $SO_3$  adsorption.

Progressing from this concept, it implies that under lean-burn conditions NO<sub>x</sub> can be stored on the surface not at a basic site but a vacancy site on mixed electronic-ionic conductors materials, such as a mixed La-Co or La-Fe oxide with a perovskite structure, In this way, the highly acidic SO<sub>3</sub> molecule is not active for adsorption and the process is not deactivated. Additionally, NO<sub>2</sub> acts as the agent by which the surface is oxidized, but subsequently allows the reduction of the stored NO<sub>x</sub> to N<sub>2</sub>.

In summary, by understanding these fundamental mechanisms of NO<sub>2</sub> adsorption in the presence and absence of CO<sub>2</sub>, testing of spinel, perovskite, and/or mixed electronic-ionic conductor materials that are acidic and electron withdrawing offer an opportunity to minimize the impact of sulfate and carbonate formation from deactivating NO<sub>x</sub>SR catalysts. In addition, Pt/NaY can act as a low temperature (< 325°C) NO<sub>x</sub>SR catalyst that is sulfur tolerant due to the unique interaction of the alkali metal in the zeolite structure with the nitrate and nitrite ion.

## **Appendix I:**

### **Palladium-Hydrotalcite NO<sub>x</sub> Storage-Reduction Catalysts**

Ryan Adams, North Carolina State University, Dept. of Chemical Engineering, Under the Advisement of Dr. Henry Lamb

#### **Introduction**

NO<sub>x</sub> emissions from internal combustion engines are a serious environmental concern, as they are a major culprit in the creation of acid rain and smog. Consequently, NO<sub>x</sub> emissions are regulated by the U.S. Environmental Protection Agency. Three-way exhaust catalysts have been effective in reducing NO<sub>x</sub> emissions from spark ignition (SI) engines that operate under stoichiometric conditions (Mahzoul, 2001). Conforming to increasingly stringent standards on NO<sub>x</sub> exhaust emissions has proven more difficult for diesel engines which operate under fuel lean (oxygen rich) conditions. Legislation requiring a 95% decrease in NO<sub>x</sub> emissions from diesel engines and the automotive industry's shift toward lean-burn SI engines have created the need for new approaches to NO<sub>x</sub> emission reduction. (Elsom, 1992) One such alternative is the NO<sub>x</sub> storage reduction (NO<sub>x</sub>SR) catalyst or NO<sub>x</sub> trap.

The NO<sub>x</sub>SR catalyst can operate under oxygen-rich conditions and can be applied to both diesel and SI engines. These materials store nitrogen oxides as nitrite or nitrate species under lean conditions, and then are regenerated via reduction releasing N<sub>2</sub> and H<sub>2</sub>O and/or CO<sub>2</sub> as byproducts. A typical NO<sub>x</sub>SR catalyst consists of platinum and barium oxide on an alumina support. The Pt/BaO/Al<sub>2</sub>O<sub>3</sub> NO<sub>x</sub> trap adsorbs NO, O<sub>2</sub>, and NO<sub>2</sub> onto the platinum sites. The adsorption is followed by a reaction between BaO and NO<sub>2</sub> to form nitrates on the surface of the catalyst. (Fridell, 2000) The commercial viability of NO<sub>x</sub> traps is hindered by the narrow range of operating temperatures, thermal degradation, and deactivation by sulfur adsorption. The surface chemistry of the metal oxide adsorbent (support) and the noble metal catalyst also play important roles in the catalyst's activity. (Mahzoul, 2001)

Hydrotalcites are naturally occurring anionic clays which can be expressed with the general formula,  $[M_x^{2+}M^{3+}(\text{OH})_{2x+2}]^+[A_{1/n}^{n-}\cdot\text{H}_2\text{O}]^-$  where x is the M<sup>2+</sup>/M<sup>3+</sup> ratio. Also known as layered double hydroxides, hydrotalcites consist of positively charged brucite-like layers between negatively charged layers of anions and water. Although rare in nature, these



compounds are easily produced and are highly customizable. Most commercial hydrotalcites resemble the naturally occurring compound,  $\text{Mg}_6\text{Al}_2(\text{OH})_{16}\text{CO}_3 \cdot 4\text{H}_2\text{O}$ . (Rousselot, 2002)

This investigation explored the preparation and activity of a 0.5 wt% palladium/commercial hydrotalcite (Pd/HT)  $\text{NO}_x$ SR catalyst. Both the catalyst and HT support were subjected to temperature-programmed desorption (TPD) tests after adsorption of  $\text{NO}_2$  and  $\text{NO} + \text{O}_2$  at  $290^\circ\text{C}$ . The Pd/HT and the HT support also were subjected to temperature-programmed reduction (TPR) in  $\text{H}_2$  following adsorption of  $\text{NO}_2$  at  $290^\circ\text{C}$ .

## **Experimental**

### *Catalyst Support*

A commercial hydrotalcite was obtained and a 10 g sample was calcined in  $\text{O}_2$  at  $600^\circ\text{C}$ . The calcined sample was carefully moved into a glove box to avoid adsorption of water. The sample was white in color.

### *Preparation of Pd/HT Catalyst*

Materials: calcined HT, reagent grade toluene (Fisher Scientific),  $\text{Pd}(\text{acac})_2$  (Strem Chemicals), airless glassware, balance, and magnetic stirrer and stirbar. 100 mL of toluene and a stirbar were added to a Schlenk flask. The flask was purged by evacuating and filling with  $\text{N}_2$  on the Schlenk line. This step was repeated 3 times. The flask was then sealed off and transferred to the glove box. 0.057 g of  $\text{Pd}(\text{acac})_2$  were weighed in the glove box and added to the 100 mL of toluene. The mixture was stirred for 30 min. resulting in a clear, yellow solution. 4.0 g of the calcined HT was added to the flask, and the mixture was stirred overnight. The resulting mixture consisted of a yellow solid in a clear solution. A fritted filter was attached to the flask, and an identical flask was attached to the other end of the filter. The system was sealed off from the environment. Next, the system was transferred out of the glove box to the Schlenk line. Gravity filtration was performed and followed by vacuum filtration and drying of the solid under vacuum overnight. The dried sample was transferred to a vial and stored in a dessicator.

### *Catalyst Testing*

TPD and TPR experiments were performed in a fixed bed quartz microreactor with continuous on-line sampling by quadrupole mass spectrometry (QMS). 0.2 g samples and a

linear temperature ramp of 10°C/min. from 100°C to 550°C were employed. In TPD, He (46 cc/min.) was used as the carrier gas. TPR experiments used H<sub>2</sub> (35 cc/min.). With all these runs, He was used as a purge gas. The necessary purge time ranged from 40 min for nitrogen oxides to 1 h or more for H<sub>2</sub>. A series of TPD experiments were performed on the Pd/HT and the blank HT:

1. NO + O<sub>2</sub> adsorption followed by TPD.
2. NO<sub>2</sub> adsorption followed by TPD.

The gas composition and concentration for the NO + O<sub>2</sub> adsorption runs were 0.85% NO and 15% O<sub>2</sub> with a He balance. The NO<sub>2</sub> runs had a composition and concentration of 1000 ppm NO<sub>2</sub>, 20% CO<sub>2</sub>, and 12% O<sub>2</sub> with a He balance. All adsorption runs were performed at 290°C for 30 min. A temperature ramp was always necessary before adsorption in order to reach 290°C. During these ramps, pure He (46 cc/min.) flowed over the samples. The Pd/HT and the HT support were also subjected to a TPR test:

1. NO<sub>2</sub> adsorption at 290°C followed by TPR.

#### *BET Surface Area*

N<sub>2</sub> adsorption using the single-point BET method was used to determine the surface area of the calcined HT and the Pd/HT catalyst. This was accomplished using a Micromeritics Flow Sorb II 2300.

### **Results**

Surface area tests performed using the single-point BET method show that the preparation of the NO<sub>x</sub>SR catalyst did not change the surface area of the calcined HT significantly. A 0.09 g sample of the calcined HT gave a surface area of 190 m<sup>2</sup>/g, and a 0.09 g sample of the Pd/HT gave a surface area of 180 m<sup>2</sup>/g.

TPD was used to measure the NO<sub>x</sub> storage capacity of the catalyst. NO + O<sub>2</sub> and NO<sub>2</sub> were adsorbed at 290°C. Below is a typical QMS trace recorded during NO<sub>2</sub> adsorption on Pd/HT.

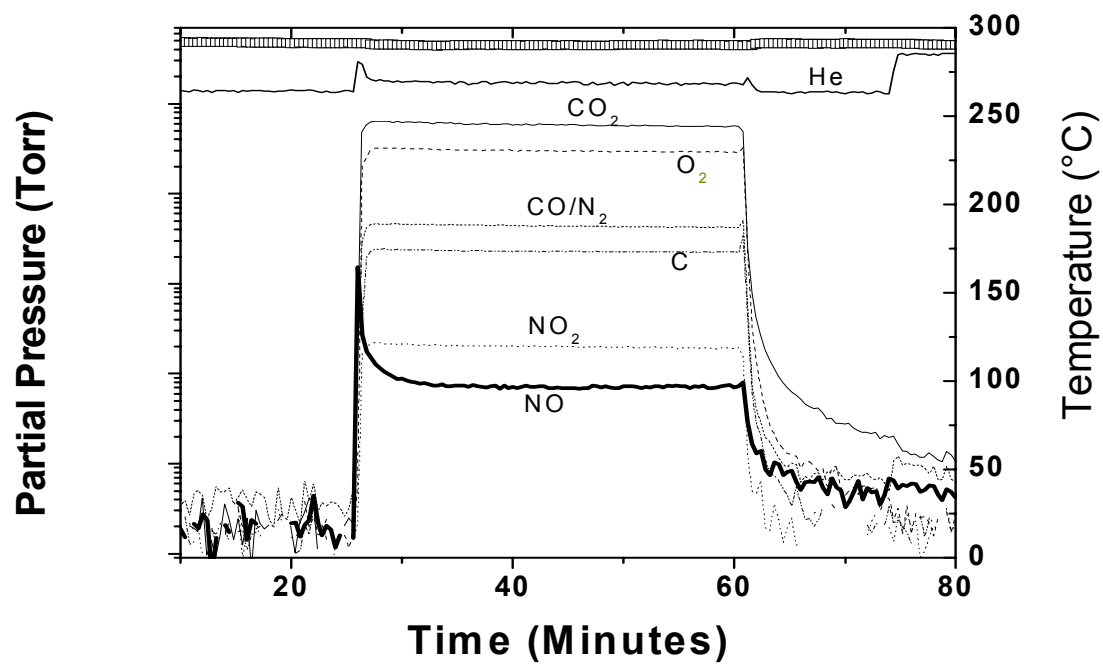


Figure 1: NO<sub>2</sub> adsorption at 290°C for 30 min on Pd/HT3.

Following adsorption, each sample was subjected to the same desorption conditions. The graph below summarizes this data.

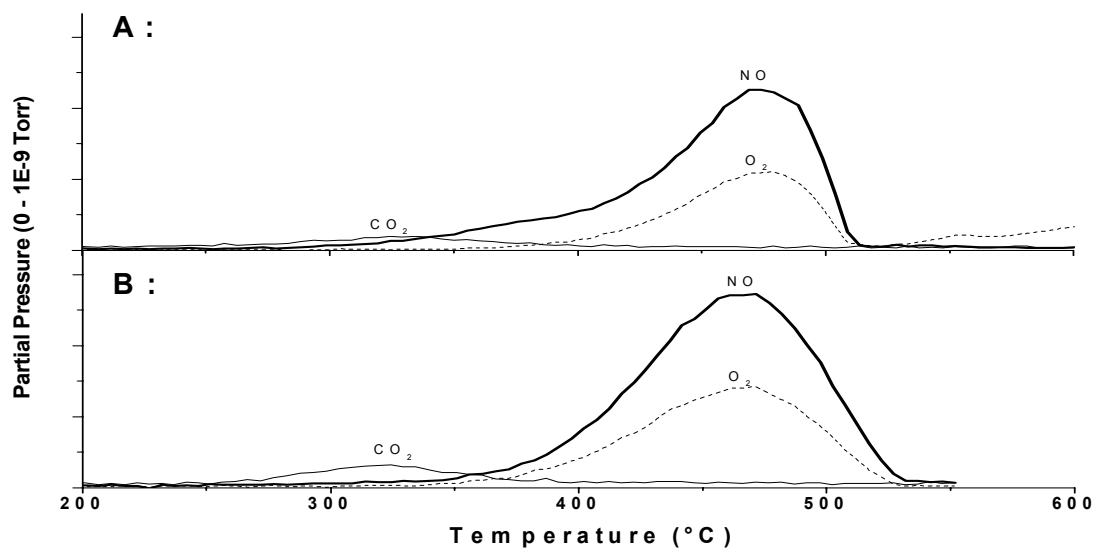


Figure 2: TPD following NO<sub>2</sub> adsorption at 290°C on (A) Pd/HT3 (B) HT3

Similarly,  $\text{NO} + \text{O}_2$  was adsorbed on the catalyst and the blank support.

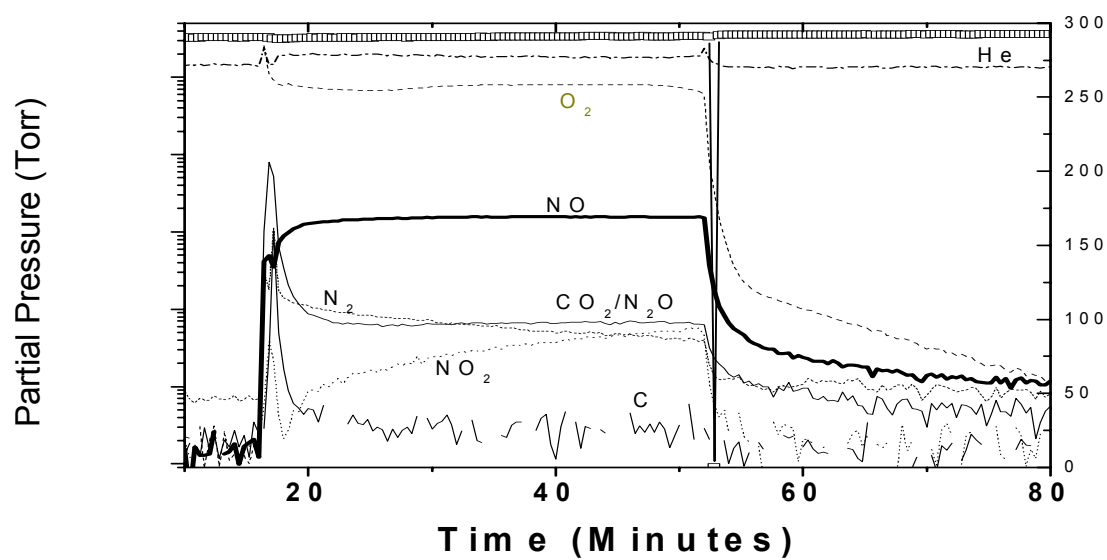


Figure 3:  $\text{NO} + \text{O}_2$  adsorption at  $290^\circ\text{C}$  for 30 min on Pd/HT3.

Below are the TPD data for the adsorption of  $\text{NO} + \text{O}_2$ .

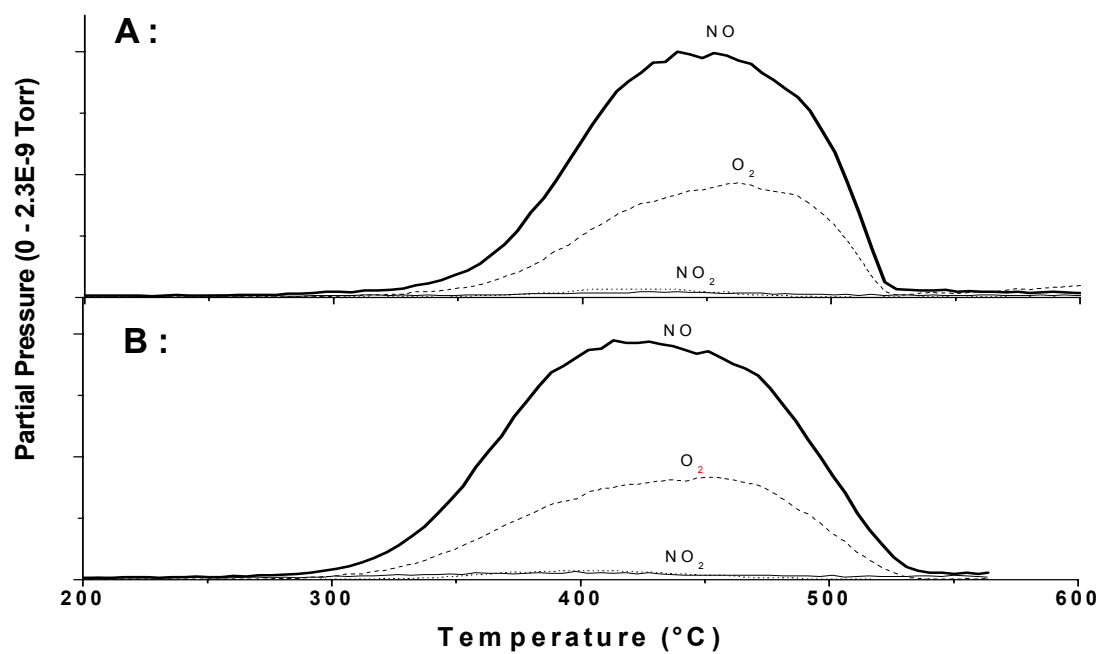
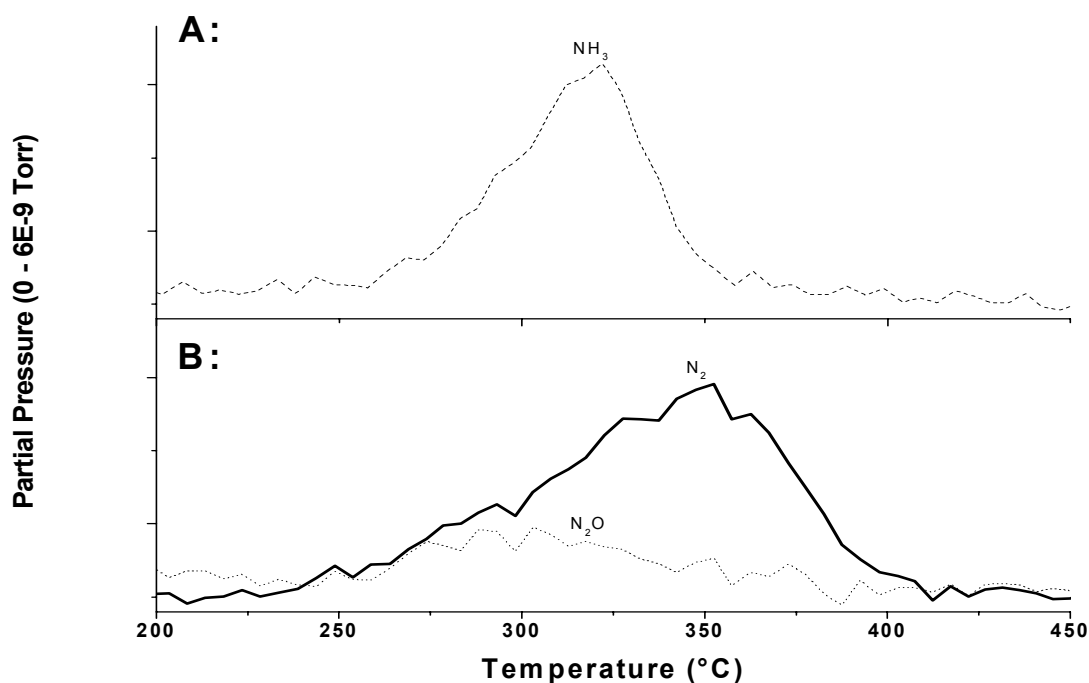


Figure 4: TPD after  $\text{NO} + \text{O}_2$  adsorption at  $290^\circ\text{C}$  on (A) Pd/HT3 and (B) HT3.

Similar TPD results were obtained with the Pd/HT and HT samples. In each case,  $\text{NO}_2$  was adsorbed as a surface nitrate ( $\text{NO}_3$ ) species that decomposes with evolution of  $\text{NO}$  and  $\text{O}_2$  at  $\sim 450^\circ\text{C}$ . Oxidation of  $\text{NO}$  to  $\text{NO}_2$  during  $\text{NO} + \text{O}_2$  adsorption is evidenced in Fig. 3, and this reaction occurs with and without Pd. The blank HT showed marginally greater storage capacity. The Pd/HT sample had been subjected to several redox cycles in  $\text{NO}$  and  $\text{H}_2$  before testing, and, consequently, its storage capacity may have been somewhat diminished.

The results from the TPR experiments show a clear effect of Pd catalysis. The goal of such an experiment is regenerate the  $\text{NO}_x\text{SR}$  catalysts without producing undesirable gaseous byproducts, such as  $\text{N}_2\text{O}$ . TPR tests were carried out on the Pd/HT and the blank HT support.



**Figure 5: TPR following  $\text{NO}_2$  adsorption at  $290^\circ\text{C}$  on (A) Pd/HT3 (B) HT3.**

Obvious differences can be noted between the two TPR traces in Fig. 5. First of all, the TPR for the Pd/HT produced  $\text{NH}_3$  (as evidenced by the  $\text{NH}_2$  peak at  $322^\circ\text{C}$ ). The blank HT produces  $\text{N}_2\text{O}$  and  $\text{N}_2$ , and the  $\text{N}_2$  peak appears at  $353^\circ\text{C}$ . Although there are currently no restrictions on ammonia emissions from diesel engines,  $\text{N}_2$  is obviously a more desirable regeneration

byproduct. For Pd/HT, the H<sub>2</sub> reduction process goes a step too far and produces NH<sub>3</sub> from the stored NO<sub>x</sub>. Since CO or hydrocarbons are more likely choices for the reductant in engine applications, TPR using CO or propane might give more promising results.

### **Conclusions**

The results show that Pd/HT may be promising as a NO<sub>x</sub>SR catalyst for diesel engines. NO<sub>x</sub> storage via NO<sub>2</sub> adsorption as NO<sub>3</sub> species on the HT support occurs with and without Pd. The TPR results suggest that Pd/HT catalyzes NH<sub>3</sub> synthesis from stored NO<sub>x</sub> at ~320°C. In future experiments, it would be interesting to examine regeneration of the Pd/HT using a different reductant, such as CO.

### **References**

- Elsom, Derek M. *Atmospheric Pollution, A Global Problem*, 2nd. Ed., Blackwell Publishers, Oxford, England (1992).
- Fridell, Erik et al. *Catalysis Letters*. Vol. 66, 71-74, 2000.
- Mahzoul, H. et al. *Topics in Catalysis*. Vol. 16/17, Nos. 1-4, 2001.
- Rousselot, I. *Journal of Solid State Chemistry*. Vol. 167, 137-144, 2002.

## Appendix II: Bulk Magnesium Carbonate and Nitrate Decomposition

### Experimental

To obtain a standard for the desorption of NO<sub>x</sub> and CO<sub>2</sub>, 0.05g of Mg(NO<sub>3</sub>)<sub>2</sub>•6H<sub>2</sub>O was physically mixed with 0.20g of SiO<sub>2</sub> and crushed in a mortar and pestle until a uniform mixture was obtained. From this sample, 0.20g was weighed and transferred to a quartz reactor where it was heated in He at a flow rate of 30mL/min. The reactor effluent was measured via a quadrupole mass spectrometer. Similarly, a sample of MgCO<sub>3</sub> was weighed and mixed with SiO<sub>2</sub> and desorbed in a quartz reactor to calibrate the signal for CO<sub>2</sub> at high concentrations.

**Table 1: Magnesium Nitrate and Carbonate Decomposition<sup>(6,7)</sup>**

Species	Reference	Formula Weight	T <sub>m</sub> (°C)	T <sub>d</sub> (°C)
MgCO <sub>3</sub>	1, p. 1150, v. 2			320
MgCO <sub>3</sub>	2, p. 731	84.3	350	350
Na <sub>2</sub> CO <sub>3</sub>	1, p. 1352, v. 2			
Na <sub>2</sub> CO <sub>3</sub>	2, p. 741	106.0	851	T <sub>b</sub> =d
BaCO <sub>3</sub>	1, p. 191, v. 1			
BaCO <sub>3</sub>	2, p. 718	197.4	811	T <sub>b</sub> =1450
Mg(NO <sub>3</sub> ) <sub>2</sub> •6H <sub>2</sub> O	1, p. 1145, v. 2			304
Mg(NO <sub>3</sub> ) <sub>2</sub> •6H <sub>2</sub> O	2, p. 731	256.4	90	330
NaNO <sub>3</sub>	1, p. 1347, v. 2			380
NaNO <sub>3</sub>	2, p. 741	85.0		T <sub>b</sub> =380
Ba(NO <sub>3</sub> ) <sub>2</sub>	1, p. 186, v. 1		592	
Ba(NO <sub>3</sub> ) <sub>2</sub>	2, p. 741	261.4	592	T <sub>b</sub> =d

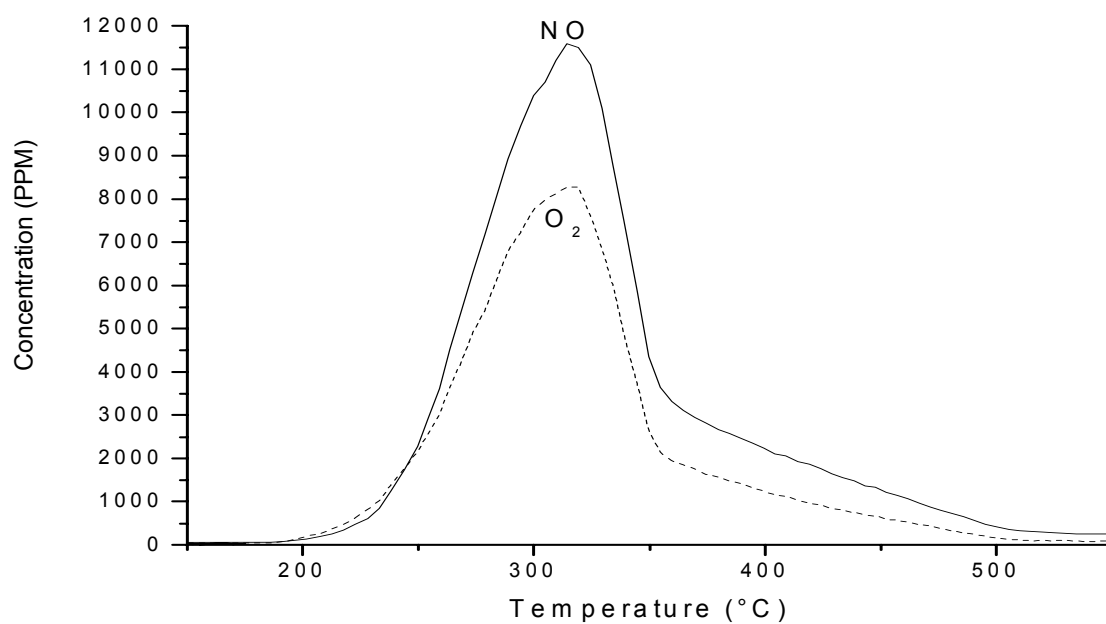


**Figure 1: Mg(NO<sub>3</sub>)<sub>2</sub> Thermal Decomposition in He**

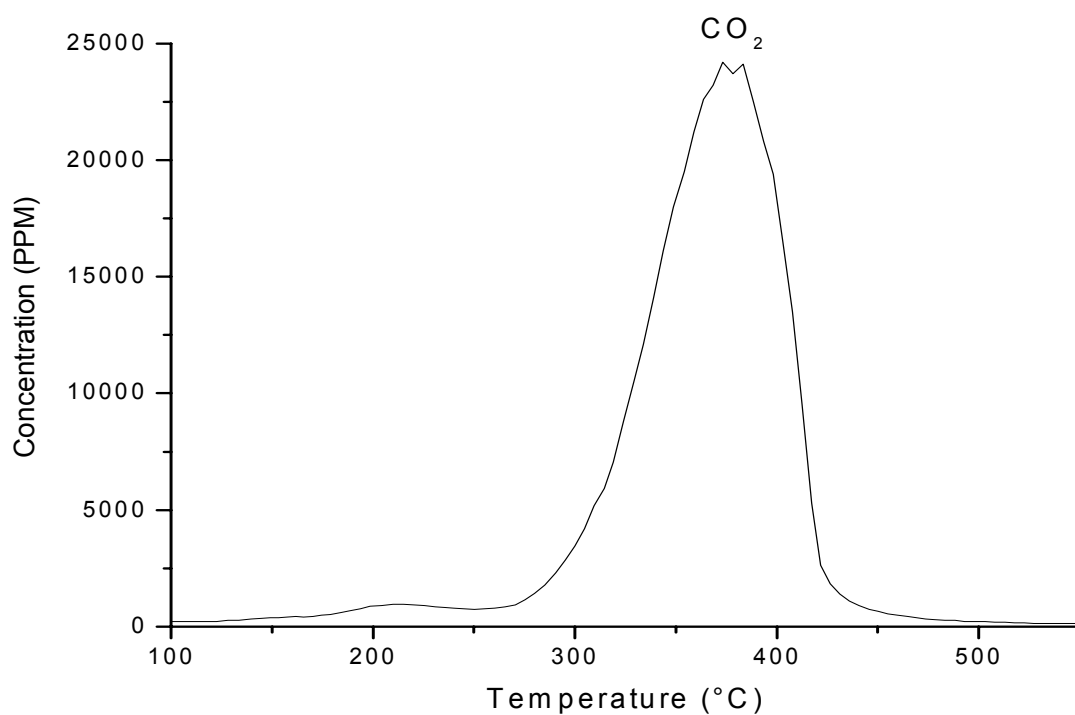


**Figure 2: MgCO<sub>3</sub> Thermal Decomposition in He**



### **Appendix III: SuperCriticalCO<sub>2</sub> (SCCO<sub>2</sub>) Solvent Extraction Apparatus Design and Assembly**

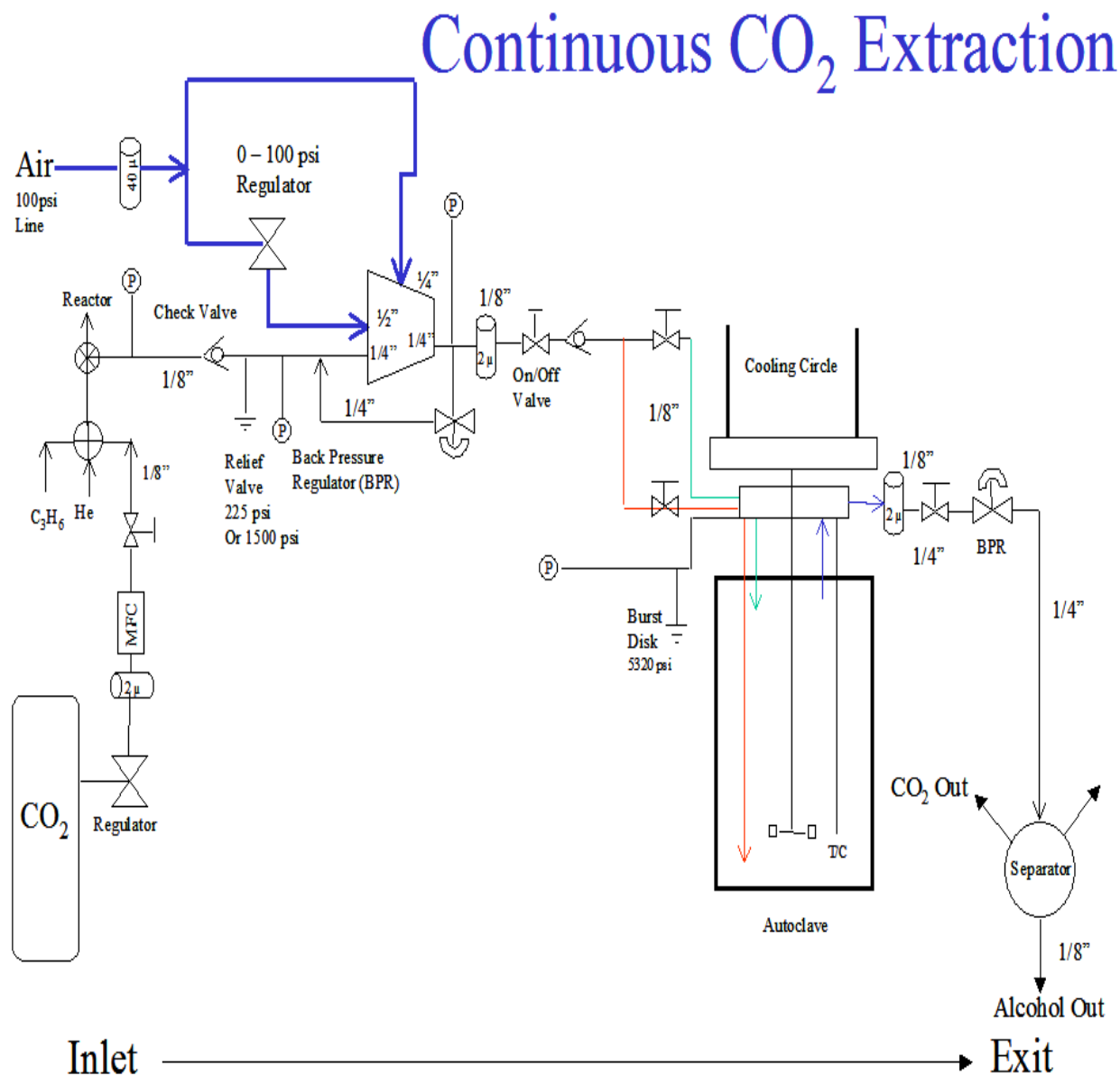
#### **Introduction:**

Traditional calcination processes can be very destructive of active pore and surfaces of catalyst materials. The process adds variability to the pore structures, causes phase changes and reduces the available pore volume for catalysis. SCCO<sub>2</sub> extraction processes were developed to remove the solvents used during solution sol-gel synthesis and afforded the opportunity of removing solvents at low temperatures. This has led to a new class of materials called aerogels. Essentially, these materials use the same sol-gel techniques, yet they incorporate SCCO<sub>2</sub> for the extraction of the solvent as opposed to high temperature drying. As a result of this novel drying method, aerogels have very high surface areas and tunable pore structures. The value that aerogels provide for NO<sub>x</sub> adsorber applications are that with these materials you can control particle nucleation, the physical/chemical properties by tuning the CO<sub>2</sub> conditions to yield very high surface area materials. By integrating a combined solution gel process, the noble metals, basic oxides and supports can be synthesized in one gel that can be dried via SCCO<sub>2</sub> to yield highly dispersed and active phases integrated with the oxide support. This technique is ideal for temperature sensitive solids and for assurance of contaminant free synthesis via extraction of solvent residues with molecular scale mixing and structure control. Lastly, very unique and tunable morphological and chemical properties can be obtained using these very versatile methods.

NO<sub>x</sub> adsorbers need to have a very close intimacy between the noble metal and basic oxides and this can be achieved through this method. In addition, a high surface area to bulk ratio can be achieved to enhance the NO<sub>x</sub> adsorption efficiency during lean exhaust conditions. The

goal of this area of research was to build and test the SCCO<sub>2</sub> apparatus for use in NO<sub>x</sub> adsorber applications. Unfortunately, we were only able to design and build the equipment and the diagram + picture are given below.

**Figure 1: SCCO<sub>2</sub> Apparatus Design**



## REFERENCES

- 1 Elsom, Derek M., *Atmospheric Pollution, A Global Problem*, 2nd. Ed., Blackwell Publishers, Oxford, England (1992).
- 2 John P.A. Neeft et al. Fuel Processing Technology. 17 (1996) 1-69
- 3 Heywood, John B. Internal Combustion Engine Fundamentals. 1988.
- 4 Gregory, D. Marshall, R.A. Eves, B. Dearth, M. Hepburn, J. Swallow, D. Brogan, M. SAE 1999-01-3498
- 5 Cant, Noel, W. Patterson, Michael J. Department of Chemistry, Macquarie University NSW 2109, Australia.
- 6 Amberntsson, Annika. Persson, Hans. Engstrom, Per. Kasemo, Bengt. App. Cat. B: Env. 31 (2001) 27-38.
- 7 Miyoshi, N. Mastumoto, S. Katoh, K., Tanaka, T. Harada, J. Takahashi, N. Yokota, K. Sigiura, M. Kasahara, K. SAE Technical Paper 950809, 1995.
- 8 Presentation by Johnson Matthey in 2001.
- 9 Kobayashi, Takeshi.; Yamada, Teiji.; Kayano, Kunihide. (N.E. Chemcat Corp) SAE 970745 February 1997
- 10 <http://en2.wikipedia.org/wiki/Electronegativity>
- 11 C. H. Bartholomew. Chem. Eng. 1984, 96
- 12 Paul T. Fanson, Margaret R. Horton, W. Nicholas Delgass, Jochen Lauterbach. Applied Catalysis B: Environmental, Volume 46, Issue 2, 10 November 2003, Pages 393-413
- 13 S. Matsumoto, Y. Ikeda, H. Suzuki, M. Ogai, N. Miyoshi. App. Cat. B: Environmental 25 (2000) 115-124.
- 14 Engstrom, P.; Amberntsson, A.; Skoglundh, M.; Fridell, E.; Smedler, G.; Appl Cat. B: Env. 22 (1999) L241-L248
- 15 K. Taylor Cat. Rev. Sci. Eng. (1993) 457.
- 16 K. Wilson, C. Hardacre, C.J. Baddeley, J. Ludecke, D.P Woodruff, R.M. Lambert, Surf. Sci. 372 (1997) 279
- 17 Amberntsson, A. Persson, H. Engstrom, P. Kasemo, B. Applied Catalysis B: Environmental 31 (2001) 27-38.
- 18 Institute of Applied Catalysis. Kings Buildings, Smith Square, London SW1P 3JJ
- 19 M. Bmisse, J.L Portefaix and M. Vrinat, Catal. Today, 10 (1991) 489-505.
- 20 A. Nishijima, H. Shimada, T. Sato. Y. Yoshimura and J. Hiraishi, Polyhedron, 5 ( 1986) 243-247.
- 21 W. Zaobin, X. Qin, G. Xiexian, E.L. Sham, P. Grange and B. Delmon, Appl. Catal., 63 (1990) 305-317.
- 22 Chen, J. P.; Yang, R. T. J. Catal. 1993, 139, 277
- 23 K. Tanaka, A. Ozaki, J. Catalysis 8 (1967)
- 24 Yamazaki, Kiyoshi; Suzuki, Tadashi; Takahashi, Naoki; Yokota, Kouji; Sugiura, Masahiro; App. Cat. B: Env. 30 (2001) 459-468
- 25 M. S.Brogan, A. D. Clark, R. J. Brisley SAE 980933
- 26 Wang, J. A.; Novaro, O.; Bokhimi, X.; Lopez, T.; Gomez, R.; Navarrete, J.; Llanos, M. E.; Lopez-Salinas, E.; J Phys. Chem. B 1997, 101 7448-7451
- 27 Wachs, Israel E. Catalysis Today 27 (1996) 437-455
- 28 Hodjati S, Vaezzadeh K, Petit C. Framework of SNR Brite-Euram European Project; Partners – DC, AG and Johnson Matthey and University of Leuven (COK) and Gothenburg (Chalmers) Catalysis Today 59 (2000) 323 – 334
- 29 G.C. Koltsakis, A.M. Stamatelos, Prog. Energy Combust. Sci. 23 (1997) 1-39.
- 30 Institute of Applied Catalysis. Kings Buildings, Smith Square, London SW1P 3JJ
- 31 Chemistry of the Elements. 2<sup>nd</sup> Edition. Greenwood, NN and Earnshaw, A. Butterworth Heinemann. University of Leeds, UK.
- 32 G. Centi, G. Fornasari b, C. Gobbi, M. Livib, F. Trifirò, A. Vaccari. Catalysis Today 73 (2002) 287–296
- 33 G. Fornasari, F. Trifirò, A. Vaccari, F. Prinetto, G. Ghiotti, G. Centi. Catalysis Today 75 (2002) 421–429
- 34 A.E. Palomares, J.M. Lopez-Nieto, F.J. La-zaro, A. Lopez, A. Corma Applied Catalysis B: Environmental 20 (1999) 257-266.
- 35 E. Manasse, Atti.Soc.Toscana.Sc.Nat.Proc. Verb. 24 (1915) 92.
- 36 Roelofs, J.C.A.A. Catalysis Today 60 (2000) 297–303
- 37 Park, PW. Caterpillar Inc. TIC report 07/30/1999
- 38 Huang HY, Long RQ, Yang RT ENERG FUEL 15 (1): 205-213 Jan-Feb. 2001
- 39 Prinetto, F. Ghiotti, G. Nova, I. Lietti, L. Tronconi, E. Forzatti, P. J. Phys. Chem. B 2001, 105 12732-12745.
- 40 Rodriguez JA, Jirsak T, Liu G, Hrbek J, Dvorak J, Maiti A J of the Am. Chem. Soc. 123 (39): 9597-9605 Oct 3 2001

- 
- 41 Hudson, John. Surface Science: An Introduction. Rensselaer Polytechnic Institute, Troy, NY. John Wiley and Sons, Inc.
- 42 Nakamoto, Kazuo. Infrared and Raman Spectra of Inorganic Compounds Part A. 5<sup>th</sup> edition.
- 43 Gadsden, J. A. Infrared Spectra of Minerals and Related Inorganic Compounds. The Butterworth Group, Reading, Mass. 1975
- 44 Jianke Liu, Pinliang Ying, Qin Xin, and Can Li. Applied Spectroscopy Volume 53, Number 1, 1999 40-43.
- 45 Dairene Uy,\* Kelly A. Wiegand, Ann E. O'Neill, Mark A. Dearth, and Willes H. Weber. J. Phys. Chem. B 2002, 106, 387-394
- 46 T. López, P. Bosch, M. Asomoza, R. Gómez and E. Ramos. Materials Letters 31 (1997) 311-316
- 47 Sultana, A; Loenders, R; Monticelli, O; Kirschhock, C; Jacobs, P; Martens, J. *Angew Chem International Ed.* 39 (2000) No. 16
- 48 Martens et al. *Angew. Chem. Int. Ed.* 2000, 39, No. 16
- 49 Hesselmann, K.; Kubaschewki, O.; Knacke, O. *Thermochemical Properties of Inorganic Substances, Vol. 1 & 2.* 2<sup>nd</sup> Ed, 1991. Springer-Verlag Berlin, Heidelberg, 1991.
- 50 Moses, Alfred J. *The Practicing Scientist's Handbook.* Van Nostrand Reinhold Company, 135 West 50<sup>th</sup> St., New York, NY 10020.
- 51 Driscoll, Josh J. Caterpillar Engine Research, May 2003.
- 52 J.A. Martens, A. Cauvel, F. Jayat, S. Vergne, E. Jobson. *Applied Catalysis B: Environmental* 29 (2001) 299-306
- 53 S. Hodjati, K. Vaezzadeh, C. Petit, V. Pitchon, A. Kiennemann. *Catalysis Today* 59 (2000) 323-334